Exploring light-matter interactions with graphene

Submitted by Christopher Lewis Beckerleg to the University of Exeter as a thesis for the degree of Doctor of Philosophy in Physics, September 2017

I certify that all material in this thesis which is not my own work has been identified and that no material has previously been submitted and approved for the award of a degree by this or any other University.

Christopher Lewis Beckerleg
March 28, 2018

Declaration of Authorship

The silicon deposition and ellipsometry measurements for the sample discussed in Chapter 2 and Chapter 4 were kindly performed at the University of Southampton by Dr Ioannis Zeimpekis. The synthesis of the pyrene-rhodamine molecule used in Chapter 5 was performed by Dr Alexis Perry at the University of Exeter.

Publications

Chris Beckerleg and Euan Hendry. "Localized plasmons induced by spatial conductivity modulation in graphene." JOSA B 33.10, 2051-2056, (2016)

C. Beckerleg, T. J. Constant, I. Zeimpekis, S. M. Hornett, C. Craig, D. W. Hewak and E. Hendry “Cavity enhanced third harmonic generation in graphene”, Applied Physics Letters, 112, 1, (2018)

Abstract

Graphene has drawn extraordinary interest from both scientists and the wider public; the idea of an atomically thin material that is staggeringly conductive while also being both strong and flexible, seems impossible. From a scientific perspective, the two dimensional nature of graphene provides an exciting playground to explore new phenomena with the potential for technical applications. The question of how light interacts with graphene underpins these devices and is often set in the context of graphene as a highly transparent material. In this thesis, results from the interaction between light and graphene will be explored across a broad frequency range and methods for manipulating the interaction between light and a graphene layer will be presented.

At infrared frequencies, nanostructured graphene displays plasmonic behaviour. A layer of graphene with a periodically modulated, array-like, conductivity analogous to graphene nano-ribbons is investigated numerically. The total response of this structure was found to arise from the hybridisation between multipolar resonances supported by different areas of the array. By designing the appropriate geometric parameters the resonant absorption of the array is shown to increase by a factor of ~50%.

In addition to displaying interesting linear properties, graphene is a strongly nonlinear material. To enhance a specific nonlinear optical mixing process, third harmonic generation, graphene is combined with a resonant cavity. The measurements of the third harmonic generation from this cavity structure show that integrating a graphene layer with a cavity increases the generated third harmonic power by a factor of 117. Numerical modelling of the cavity structure shows the enhancement mechanism arises from the cavity structure supporting a resonance in the electric field at the wavelengths of both the incident and third harmonic. A value for the bulk third order susceptibility of graphene of, $\chi^{(3)} = 4 \times 10^{-17}\,(\mathrm{m/V})^2$ was determined from these numerical models.

Finally, the influence of strain in a graphene layer on the fluorescence collected from a molecule deposited on top of the graphene layer is investigated. Using Raman spectroscopy, the level of local strain was mapped across a graphene sample and confocal microscopy was used to measure the emitted luminescence. The observed correlation between the level of strain and luminescence intensity is supported by a simple model of a dipole near a graphene sheet.

Acknowledgements

Firstly I would like to thank Euan Hendry for his boundless enthusiasm for science and for introducing me to the world of scientific research. I would also like to acknowledge the support of the European Commission (FP7-ICT-2013-613024-GRASP). I am also grateful for the technical and scientific support of many people. To Sam and Tom, thank you for your patience and the clear explanations you could always provide. I would also like to thank the small army of cleanroom-wizards who taught me finer points of the dark art of device fabrication. I was lucky to spend time with a great number of excellent people and I would like to thank all of those who contributed to SPIE (with Martin helping to proof this thesis) and made my time with SPIE as fun as it was. A special mention goes to Wednesday football which proved a unexpected highlight of my week. Thank you all.

I would also like to thank my long suffering house mates for all the support they provided. Tim, for all the no-strings fun and all the various walks (via various pubs) and Lucy, wubalubadubdub! To the repeat offender Ryan, while Exeter, our home, is now behind us, the world is ahead. Look to my coming and I will see you on the other side of the world. To Jess, I could not have asked for a better partner for my PhD journey. Thus, unquestionably, your greatest contribution was introducing me to Neil and Sproggie. Their support has proved invaluable. Finally, I would like to thank my family for the decades of work making me into the person willing to tackle the challenge of a PhD and for their support along the way.

Contents

List of Figures

List of Abbreviations

AFM	Atomic force microscope
AOBS	Acousto-Optical beam splitter
APD	Avalanche photodiode
APS	Ammonium persulfate
AOTF	Acousto-optical tunable filter
BBO	Barium borate
CCD	Charge-coupled device
CVD	Chemical vapour deposition
DFG	Difference frequency generation
DFT	Density functional theory
e-h	Electron-hole pair
FDTD	Finite difference time domain
FET	Field effect transistor
FTIR	Fourier transform infrared spectroscopy
FWHM	Full width half maximum
GaAs	Gallium arsenide
HCP	Hexagonal close packed
LBO	Lithium triborate
OPA	Optical parametric amplification
PDMS	Polydimethylsiloxane
PML	Perfectly matched layer
PMMA	Poly(methyl methacrylate)
PMT	Photon multiplier tube
RP	Rhodamine-pyrene molecule
SERS	Surface enhanced Raman spectroscopy
SiC	Silicon carbide
THG	Third harmonic generation

List of Symbols

Quantity	Symbol	Units
Angular frequency	ω	rads^{-1}
Carbon-Carbon bond length	a_0	$1.42 \times 10^{-10}\,\mathrm{m}$
Charge on electron	e	$1.602 \times 10^{-19}\,\mathrm{C}$
Fermi energy	E_f	eV
Fermi velocity	v_f	ms^{-1}
Mass of an electron	m_e	$9.11 \times 10^{-31}\,\mathrm{kg}$
Mobility	μ	$\mathrm{cm}^2/(\mathrm{Vs})$
Power	P	$\mathrm{W}\,(\mathrm{J\,s}^{-1})$
Reduced Planks constant	$\hbar$	$1.054 \times 10^{-34}\,\mathrm{Js}$
Susceptibility, second order	$\chi^{(2)}$	~$1 \times 10^{-12}\,(\mathrm{mV}^{-1})$
Susceptibility, third order	$\chi^{(3)}$	~$1 \times 10^{-20}\,(\mathrm{mV}^{-1})^2$
Speed of light in free space	c	$3 \times 10^8\,\mathrm{m\,s}^{-1}$
Vacuum permeability	μ_0	$4\pi \times 10^{-7}\mathrm{Am}^{-2}$
Vacuum permittivity	ϵ_0	$8.85 \times 10^{-12}\,\mathrm{Fm}^{-1}$

Chapter 1

Introduction

Understanding how light interacts with matter has been of key interest to an enormous number of scientists spanning the natural sciences for many decades. From a historical perspective, the development of microscopes, ranging from optical to highly sophisticated fluorescence microscopy [1], has allowed physical phenomena to be investigated with increasing magnification. This shrinking scale has allowed images to be taken far beyond the resolution of the human eye and recently allowed imaging with a resolution greater than the diffraction limit [1]. Physicists have used knowledge of how materials interact with light as a characterisation tool for hundreds of years, aiding the discovery of new elements [2]. Using light to probe the properties of materials also offers another extension beyond the limits of the human eye by being able to probe outside the visible frequency range. For example, the nature of vibrational bonds between molecules allows for unique characterisation of materials through the use of infrared spectroscopy [3]. The use of ultraviolet light has also enabled extremely high resolution lithography: a technology which underpins large scale manufacturing of integrated circuit technology [4].

Rather than these passive light-matter interactions, the interaction between light and a material can be actively controlled. A well understood technique for controlling light is with a photonic crystal. Photonic crystals are materials with a periodic refractive index, creating an analogue of electrons in a periodic potential for light. The periodic refractive index creates bandgaps for photons that interact with the crystal, only allowing photons with specific wavelengths to propagate through the material and blocking all other wavelengths [5]. The speed and bandwidth of photon-based circuits together with their ease of integration with silicon technology (which operates at a wavelength of $1.5\ \mu\mathrm{m}$) make photonic crystals of great technological interest [6].

To preserve a suitable bandgap, photonic crystals have to be made from high-quality materials, such as silicon spheres, as defects can quickly destroy the band gap behaviour [7]. While unintentional defects in photonic crystals result in unwanted losses, deliberate defects can offer benefits. Through patterning defects at controllable locations, a large degree of

control can be achieved over the propagation of light through a photonic crystal, to create mirrors [8][9], cavities [10] and waveguides [11] as the light is only allowed to propagate along specific channels, not through the rest of the photonic crystal. Photonic waveguides are of particular interest as they allow guided photons to propagate over long distances and around very tight bends [12]. These properties allow photonic crystals to be combined into complex waveguiding geometries forming the basis for optoelectronic devices [13][14][15]. Additionally, photonic cavities also exhibit very large Q-factors, with the current record measured to be ~6×10^5 [16]. These large Q-factors exhibit strong light-matter interactions which are of great interest in biosensing and nonlinear optical applications [17][18].

Creating three dimensional photonic crystals which operate in the optical regime requires nanoscale precision and a high dielectric contrast, both of which present fabrication challenges. A solution to these fabrication challenges is self-assembling molecules [19]. Furthermore, new photonic crystals which possess topologically insulating properties give an experimentally accessible analogue for investigating fundamental properties of topological insulators and the potential for topological protection from defects in photonic crystals [20].

Similarly, the field of transformation optics is also concerned with designing the properties of a material to control how electromagnetic waves propagate through the material [21]. Named for the coordinate-transform mathematics, transformation optics allows judicious design of a continuous refractive index profile to create custom designed electromagnetic behaviour [22][23]. Typically cited designs are refractive index profiles capable of lensing behaviour by guiding surface waves to a point [24], or capable of cloaking behaviour by guiding waves around regions of space [25].

The interface between a metal surface and a dielectric presents another interaction between light and matter. Electromagnetic radiation incident on such an interface can cause a collective oscillation in the electrons in the metal, known as surface plasmons [26]. These collective oscillations are known as surface plasmon and are highly confined to the surface of the metal. The large degree of confinement leads to a huge enhancement of the incident electromagnetic field, demonstrated to be up to five orders of magnitude [27]. This field enhancement can be understood through the dispersion relation in Equation (1.1). This important relationship, governing the important frequency behaviour of surface plasmons, can be derived by applying Maxwell's equations to the metal-dielectric interface and imposing suitable boundary conditions [26],

$$\omega_{pl} = \sqrt{\frac{e^2 n_e}{(m_e \epsilon_0)(1 + \epsilon_d)}}, \tag{1.1}$$

where ω_{pl} is the frequency of the surface plasmon, ϵ_d is the permittivity of the dielectric and n_e is the electron density in the metal, m_e is the mass of an electron. The dispersion relation demonstrates the characteristic square root relationship between the surface plasmon frequency of a metal and the electron density of the metal [28]. From Equation (1.1), the wavevector of the plasmon is greater than a free space photon, leading to enhanced electric fields. The high field confinement and the enhanced fields surrounding at the surface of the metal are a very attractive feature of surface plasmons. The large fields are a suggested mechanism for the observed enhancement in techniques for probing surface chemistry, such as Raman spectroscopy [29] and are attractive for a variety of technologies, such as detecting biomolecules [30]. The large confinement of surface plasmons, relative to the excitation beam, opens the door for the ability to control light on a subwavelength scale [31]. Through the design of suitable waveguides, surface plasmons have potential for a variety of complex plasmonic circuits, such as Mach-Zehnder interferometers and Schottky detectors, making them an interesting field of research [32] [33][34] [35]. However, in order for free space light to excite a surface plasmon with its larger wavevector, extra momentum has to be provided to incident light.

Two widespread techniques for providing this extra momentum to the incident light are a prism, or an array of metallic particles [36][37]. The sophisticated nanofabrication techniques that are available now, allow nanoparticles to be combined in complex geometries to optimise performance and facilitate easy integration for future devices [38] [39]. Since the plasmonic properties of a nanoparticle are sensitive to various geometric properties, such as the size, shape, pitch and the material of the nanoparticle, a limited degree of control can be achieved [40][41][42][43].

The field of plasmonics is currently concerned with designing suitable metallic arrays to interact with light [44]. The use of plasmonics allows for control of the interaction between light and matter to extend beyond using the light as a probe to investigate the existing physical properties of a material and allows investigations on a nanometre scale [45][46]. As a result, plasmonics has been suggested as a possible route for overcoming the diffraction limits of fibre optic technology [47]. Overcoming the diffraction limit would allow the data transmission capabilities of fibre optic technology to be combined with existing electronic devices, greatly improving the bandwidth of electronic devices [48] [49]. Plasmonics has other applications facilitated by the nanoscale, such as highly sensitive biosensors [43][50], optical modulators [51], and optical tweezers [52][53]. By incorporating recently discovered materials [54], such as graphene, the performance of plasmonic devices can be improved. These new materials are of particular interest for the low losses they exhibit and extending the accessible wavelength range [44][55] [56].

1.1 Graphene

The desire to investigate increasingly smaller length scales has been facilitated by the isolation of graphene, creating a new subfield of physics in low dimensional materials [57][58]. As mentioned in the introduction, graphene displays a large number of intriguing physical properties when compared to other materials. First of all, under the application of a perpendicular magnetic field, graphene displays a difference to the conventional quantum Hall effect of a two dimensional electron gas. In these two dimensional electron gases, increasing the applied magnetic field causes the longitudinal conductivity to display a series of spikes and the transverse conductivity to display a series of flat steps [28]. In graphene, this sequence occurs at half-integer steps of $4e^2/h$, hinting that the charge carriers in graphene behave very differently to other two dimensional gases, being more accurately described by a Dirac-like relativistic equation [59]. Despite being a monolayer, the Young's modulus of graphene has been measured to be surprisingly large ~1 TPa [60][61]. This value of the Young's modulus is comparable to diamond and much higher than other conducting materials such as copper [62][63]. The extraordinary value of the Young's modulus of graphene has allowed mechanical sensing applications to be pushed down to the nanoscale [64] [65]. Graphene also exhibits a surprisingly large thermal conductivity of $5 \times 10^3\ \mathrm{Wm^{-1}K^{-1}}$, again outperforming copper [66] [67]. These superior mechanical and thermal properties make graphene an interesting alternative for the future, making flexible and heat-efficient electronic devices possible. While graphene is widely known to be highly transparent it also displays other interesting electromagnetic behaviour. This thesis will focus on the interaction between electromagnetic radiation and graphene.

1.1.1 Structure of Graphene

A microscale description of materials is a useful tool for understanding the properties of a material. For graphene, this starts with the iconic carbon honeycomb, formed by the highly directional σ bonds between two carbon atoms, as shown in Figure (1.1) [68]. This structure has even been experimentally imaged by electron microscopy [69]. Mathematically, the hexagonal structure is comprised of a triangular lattice, constructed with lattice vectors, v_1 and v_2, with a two atom basis; as displayed by the red and blue circles in Figure (1.1), indicating atoms belonging to independent sub-lattices, A and B respectively [70].
From Figure (1.1) the lattice vectors, v_1 and v_2, are given by,

$$v_1 = \frac{a_0}{2}(3, \sqrt{3}), \qquad v_2 = \frac{a_0}{2}(3, -\sqrt{3}). \qquad (1.2a, 1.2b)$$

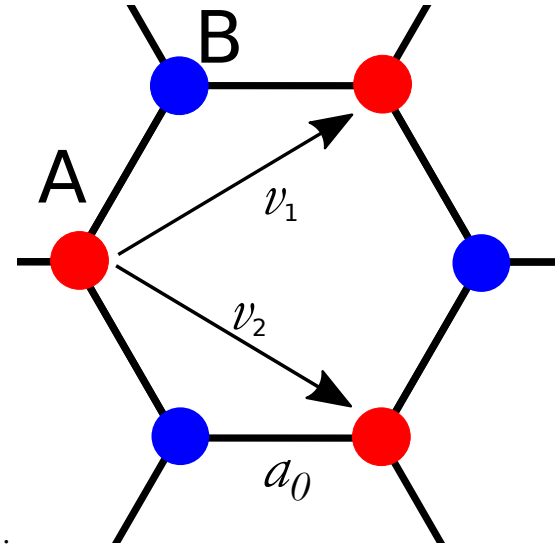

FIGURE 1.1: The interconnected triangular lattices of A (blue circles) and B (red circles) with the two lattice vectors, v_1 and v_2, $a_0 = 1.42$ Å is the interatomic distance between A and B [70].

Consequently, the Brillouin zone is constructed using the Bravais lattice vectors [71],

$$\vec{b_1} = \frac{2\pi}{3a_0}(k_x, \sqrt{3}k_y), \qquad \vec{b_2} = \frac{2\pi}{3a_0}(k_x, -\sqrt{3}k_y), \tag{1.3a, 1.3b}$$

with the interatomic distance between carbon-carbon bonds $a_0 = 1.42$ Å[70]. These Bravais lattice vectors allow for the band structure of graphene to be calculated. Following the approach laid out by Wallace in 1947, only the nearest neighbour interactions are considered i.e. between sites A and B on Figure (1.1) [72]. These Bravais lattice vectors can then be incorporated into a tight binding Hamiltonian to find the band structure of graphene [73].The resulting explicit form of the band structure is given by,

$$E(\vec{k}) = \pm t\sqrt{3 + 2\cos\left(\sqrt{3}k_y a_0\right) + 4\cos\left(\frac{\sqrt{3}k_y a_0}{2}\right)\sin\left(\frac{3k_x a_0}{2}\right)}, \tag{1.4}$$

where a_0 is the interatomic distance from Figure (1.1), $|k| = \sqrt{k_x^2 + k_y^2}$ and the intersite hopping energy, $t = -0.297\,\text{eV}$ [74]. The next-nearest neighbour interaction, $t' = -0.073\,\text{eV}$, is very small, justifying the nearest neighbour approximation in Equation (1.4). This approximation applies across the whole Brillouin zone, preserving the symmetry between electrons and holes [68].

For undoped and unstrained graphene, the unit cell contains two electrons, one from each of the A and B sublattices. The valence band is completely filled and the Fermi

level sits where the conduction and valence band touch, as shown as the blue plane on Figure (1.2a) [75]. The full electronic band structure, as shown in Figure (1.2a), does not immediately reveal any peculiar properties, however at the energy range considered in this work, ($E < 2\,\mathrm{eV}$), the band structure can be approximated as linear, as seen in Figure (1.2b). The points where the conduction and valence band meet are known as Dirac points, reflecting the relativistic nature of equation that describes electrons in graphene [68]. This linear band structure demonstrates a striking difference between graphene and conventional materials, where the band structure can be approximated as parabolic, and is the origin of many of the unique phenomena that graphene displays.

.

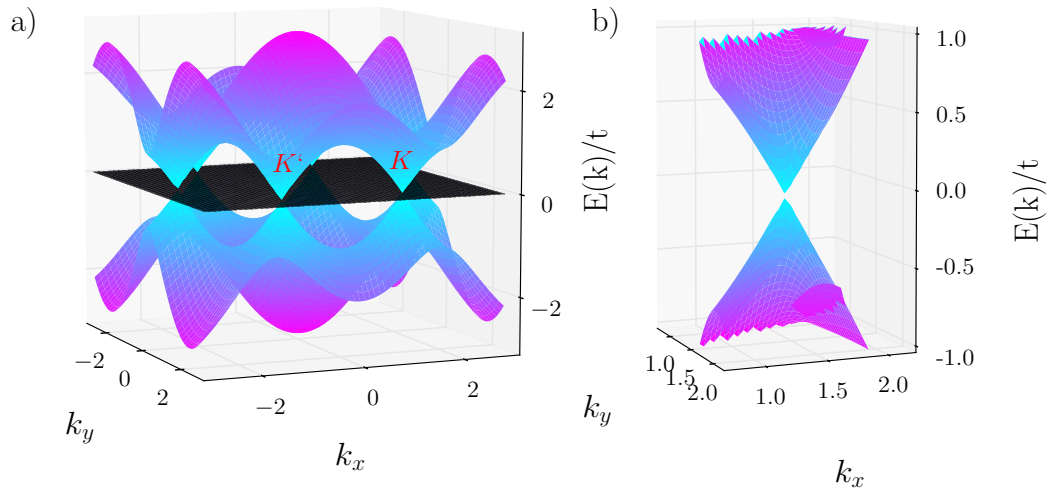

FIGURE 1.2: a) The full band structure as given by Equation (1.4) with the inequivalent Dirac points, K and K', labelled. b) A zoom into a section of the full band structure, displaying the linear behaviour. The Fermi level is shown as the blue plane exactly between the valence and conduction band.

1.1.2 Synthesis of Graphene

To explore these phenomena requires the synthesis of high-quality, large-area, single layer graphene. This challenge has spawned a huge variety of fabrication techniques [76]. The original experiments into identifying graphene by Geim et al. exploited a mechanical exfoliation technique to strip small flakes of single layer graphene from a larger graphite sample. This fabrication method produces graphene, virtually free from defects [77] and with very high mobilities between $1 \times 10^4\,\mathrm{cm^2V^{-1}s^{-1}}$ and $1 \times 10^5\,\mathrm{cm^2V^{-1}s^{-1}}$ [57][78]. However, typical flakes are only tens of microns in size, severely limiting the practical

application of this synthesis method. Single layer graphene can also be obtained from bulk graphite through sonication, but this approach has a low yield of single layer graphene [79]. Chemical solutions do improve the yield of single layer graphene, however these chemicals are expensive and hazardous, again limiting wide spread use [80]. It must be mentioned that some success has been achieved from fabricating graphene nanostructures from carbon-based materials such as carbon nanotubes. Narrow channels of graphene known as nanoribbons, <20 nm wide, display unique electrical properties but fabricating such narrow channels is challenging as this is close to the resolution limit of electron-beam lithography. Suitable channels can be made by "unzipping" carbon-nanotubes through careful Argon etching or chemical etching [81][82].

To increase the area of graphene generated, an alternative to slicing graphite layers apart, is growing graphene on a substrate from molecular components. A highly lauded approach for such growth is the thermal treatment of crystalline silicon carbide (SiC) [83]. Exposing SiC to high temperatures between, 1000 °C and 1500 °C, in ultra-high vacuum, 1×10^{-10} Torr, causes the silicon to sublime, leaving a layer of graphene at the surface [84] [85][86]. While this method of growth can produce high-quality graphene, transferring the tightly bonded graphene to an arbitrary substrate remains a problem [87][88].

A widespread technique for creating large areas of reliably single-layer graphene which can easily be transfered to arbitrary substrates is through chemical vapour deposition (CVD)[89]. While graphene can be grown on many metals, e.g. nickel [90] or palladium [91], the affordability of copper makes it the metal of choice [92]. The CVD process starts by placing a film of copper into a furnace, where the pressure inside the chamber is lowered to ~10 mTorr. The chamber is then heated to high temperatures, ~1000 °C, and methane gas is passed over the copper foil [93][94]. The CVD process has a large number of experimental parameters such as: the rate of heating, the choice of gas, the subsequent flow rate and pressure of gas. These parameters can be used to optimise the quality of the graphene produced and were investigated by Li et al. to show an increase from 7000 $\mathrm{cm^2V^{-1}s^{-1}}$ to 16 000 $\mathrm{cm^2V^{-1}s^{-1}}$ in the mobility of the graphene [95].

Transferring the graphene from the copper film to a substrate of choice relies on a PMMA-assisted technique. First a layer of PMMA is spun over the graphene as a protective and supportive layer. The copper film is then removed by chemical etching and the PMMA-graphene structure mechanically transferred to the substrate. This transfer technique will be expanded upon in Chapter 2 and been demonstrated as a method of transferring large areas of graphene to a substrate of choice [96][97]. Despite CVD graphene typically having much lower mobilities ~4×10^3 $\mathrm{cm^2V^{-1}s^{-1}}$[93], than exfoliated graphene, typical mobilities remains high compared to conventional materials. The discrepancy between the mobilities of CVD and mechanically exfoliated graphene has been demonstrated by Banszerus et al.

to arise from the transfer technique rather than a limitation of the CVD growth method. A delicate transfer technique allowed Banszerus et al. to measure an extremely high mobility of $3.5 \times 10^5\,\mathrm{cm^2V^{-1}s^{-1}}$ from CVD graphene [98]. The ability to fabricate large areas of high-quality graphene makes CVD graphene an attractive approach for a range of technological applications and will be used in this thesis.

1.1.3 Optical Properties of Graphene

Earlier, graphene was introduced as highly transparent material. This section explores the physics underlying this transparency and related optical phenomena. Optical absorption occurs as a result of transitions between bands, as shown in Figure (1.3). This diagram shows doped graphene in which the Fermi level has been shifted away from the Dirac point compared to Figure (1.2). The linear dispersion of Equation (1.4) is plotted in solid black lines and the position of the Fermi energy, relative to the the Dirac point, marked by the red shaded region. A photon with an energy greater than the Fermi energy, ω_1 in Figure (1.3), can be absorbed by promoting an electron from the valence band to the conduction band. However, a photon with an energy less than the Fermi energy, ω_2, cannot be absorbed by an interband transition due to the lack of an initial electronic state for that electron to promote. With the graphene incorporated into a FET device, frequency at which this cut off occurs can be controlled via the Fermi level through the application of an external voltage. For typical values of doping in a single layer of graphene the Fermi energy sits at $0.1\,\mathrm{eV}$ or $232\,\mathrm{THz}$. This Pauli blocking, or cut off frequency, in the absorption spectrum has been observed by Wang et al and Li et al [99] [100].

Experiments into the transmission and absorption properties of graphene also show for a broad range of optical frequencies, absorption of graphene becomes a constant. The working laid out by Katsnelson offers an insight into how this phenomena arises [68]. The power of plane wave, incident on the graphene, derived from the Poynting vector [101] can be written as,

$$W_{inc} = \frac{c}{4\pi}|\vec{\mathbf{E}}|^2, \tag{1.5}$$

where the electric field of the incident plane wave is given by $\vec{\mathbf{E}}$. Secondly, by using a first order perturbation theory, the power absorbed by the graphene layer can be written as [68],

$$W_{abs} = \frac{e^2|\vec{\mathbf{E}}|^2}{4\hbar}. \tag{1.6}$$

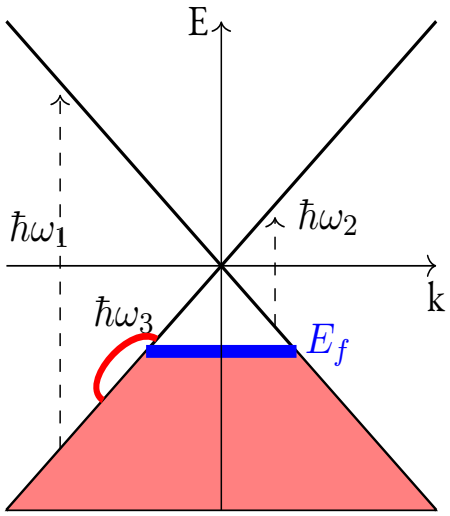

FIGURE 1.3: Schematic of the linear approximation of the band structure from Equation (1.4), (solid black lines), with allowed optical transitions, ω_1, and blocked transitions, ω_2, labelled. Intraband transitions are labelled as ω_3. The Fermi level, shifted from the Dirac point, is shown in blue and the occupied states shaded in red.

These two expressions can be combined to find an expression for the absorption coefficient in graphene Ω_{abs},

$$\Omega_{abs} = \frac{W_{abs}}{W_{inc}} = \frac{\pi e^2}{\hbar c} = \alpha\pi \approx 2.3\%, \tag{1.7}$$

where α represents the fine structure constant, the dimensionless quantity governing the strength of the electromagnetic interaction [102]. This rare example, in solid state physics, of a phenomena exclusively depending on fundamental constants has been simply, but very effectively, demonstrated by Nair et al [103]. The broad absorption spectrum of graphene also highlights its potential for photodetection applications [104]. As a result, graphene is being considered for numerous applications, such as solar-cells, photodetectors, and displays, that aim to exploit the combination of a highly conductive yet transparent single layer [105]. Another attractive feature of graphene-based devices is the degree of tunability that can be achieved over the Fermi level. A ubiquitous technique for controlling the electrical properties of semiconducting materials is through the application of an external voltage using a field effect transistor (FET) geometry [28]. Reducing the scale of the FET devices has been the focus of the computing industry. However, traditional silicon based devices face problems that come with the relentless demand for miniaturisation [106]. Graphene has been suggested as an attractive solution to the problems associated with miniaturisation due to its atomic thickness in combination with the efficiency of the doping that can be achieved

[107][57]. This dynamic control over the Fermi level in graphene has been demonstrated to perform at very high frequencies, approaching 100 MHz [108]. By combining planar graphene with metamaterials, impressive modulation depths can be achieved [109][110]. These fast switching speeds combined with low dimensionality, mean graphene could also be useful for high speed communication devices [111]. Modern communications rely on the ability to control light, as optical based devices allow for technologies to meet the ever increasing demand for smaller and faster devices. On the other hand, this presents a challenge in how to control light.

Moreover, the benefits of the low absolute value of the absorption in Equation (1.7) creates an experimental challenge of identifying graphene on the substrate. Depositing graphene onto a silicon substrate, with a 300 nm oxide layer, improves the optical contrast compared to glass but the optical contrast remains low at ~8% Blake2007 With experience, the optical contrast method can be used to identify regions of monolayer graphene. A routinely used optical technique for characterising graphene samples is Raman spectroscopy. This non-destructive and non-contact technique can be used to uniquely identify the number of layers in few-layer and monolayer graphene samples. A Raman spectrum can also yield detailed chemical information about a graphene sample, such as the level of strain and doping [112]. The application of Raman spectroscopy to graphene will be expanded on in Chapter 2.

Having a mathematical model for how the interaction between an incident electromagnetic wave and graphene is mediated will give greater understanding as to why graphene displays these optical phenomena. For other metallic materials, the interaction with electromagnetic waves is mediated by the free electrons of the metal being driven by an incident electromagnetic field, as described by the conductivity of the metal [113]. For graphene, the conductivity can be found by starting with the the Kubo formalism. This approach describes an explicit, Fermi level, temperature and frequency dependant conductivity as the following [114][115][116][117][118],

$$\sigma_g(\omega, E, \tau^{-1}, T) = \frac{-ie^2(\omega + i\tau^{-1})}{\pi\hbar^2}\left[\frac{1}{(\omega + i\tau^{-1})^2}\int_0^\infty E\left(\frac{\partial f(E)}{\partial E} - \frac{\partial f(-E)}{\partial E}\right)\mathrm{d}E - \int_0^\infty \frac{f(-E) - f(E)}{(\omega + i\tau^{-1})^2 - 4\omega^2}\,\mathrm{d}E\right], \tag{1.8}$$

where $f(E) = \{\exp[(\hbar\omega - E_f)/k_bT] + 1\}^{-1}$ is the Fermi-Dirac distribution. The scattering rate, τ, for this thesis is considered to be dominated by impurity scattering, $\tau = \mu E_f/ev_f^2$, typically, ~$50 \times 10^{-15}\,\mathrm{s}^{-1}$ [119], where μ is the mobility and v_f, the Fermi

velocity. A derivation of Equation (1.8) from a time dependent Hamiltonian, can be found in the work of P.A.D. Gonçalves and N.M.R. Peres [120]. Equation (1.8) describes two distinct contributions to the total conductivity, namely intraband and interband. For clarity this can be re-written as $\sigma_g = \sigma_{intra} + \sigma_{inter}$. These processes are shown in Figure (1.3) with σ_{intra} arising from transitions within the valence band, ω_3, and σ_{inter} describing electrons being excited from the valence band to the condition band, ω_1. Evaluating the integral for the first term in Equation (1.8) gives [121],

$$\sigma_{intra} = \frac{2ie^2T}{\pi\hbar(\omega + i\tau^{-1})} \ln[2\cosh(E_f/2T)]. \tag{1.9}$$

For typical values of the Fermi level, $E_f \gg k_bT$ [122], so Equation (1.9) asymptotes towards [123] [124],

$$\sigma_{intra} = \frac{ie^2E_f}{\pi\hbar(\omega + i\tau^{-1})}. \tag{1.10}$$

Notably, Equation (1.10) is in the form of a modified Drude expression, which describes electrons as being free to move in a lattice [125][126]. This modified Drude behaviour was observed by Horng et al. [127]. Evaluating the second integral in Equation (1.8) with the same condition on the Fermi level gives,

$$\sigma_{inter} = \frac{e^2}{4\hbar}\left[\Theta(\hbar\omega - 2E_f) + \frac{i}{\pi}\log_{10}\left|\frac{\hbar\omega - 2E_f}{\hbar\omega + 2E_f}\right|\right], \tag{1.11}$$

where $\Theta(x)$ is the Heaviside step function. These two competing contributions to the total conductivity, $\sigma_{total} = \sigma_{intra} + \sigma_{inter}$, are plotted in Figure (1.4) with $E_f = 0.3\,\mathrm{eV}$ and $\tau = 50 \times 10^{-15}\,\mathrm{s}^{-1}$. Figure (1.4) exhibits three distinct features. Most notable is the sharp step, which is smoothed with increasing temperature, at $145\,\mathrm{THz}$, corresponding to a frequency of twice Fermi level showing the transition between the intraband and interband contributions to the conductivity [121]. For frequencies below twice the Fermi level the conductivity is dominated by the intraband contributions given in Equation (1.10). Finally, for frequencies above twice the Fermi level the interband transitions dominate over the intraband contribution as these transitions are not Pauli blocked. At these high frequencies, moving into the optical regime ($700\,\mathrm{nm}$) as marked by the shaded region in Figure (1.4), the conductivity reaches the expected constant value, of 2.3% at optical frequencies [100].

With this expression for the conductivity, the interaction between light and graphene can be considered. As a comparison to plasmons supported by a metallic nanoparticle, governed by Equation (1.1), the dispersion relation of plasmon supported by a graphene layer between two dielectrics is given by,

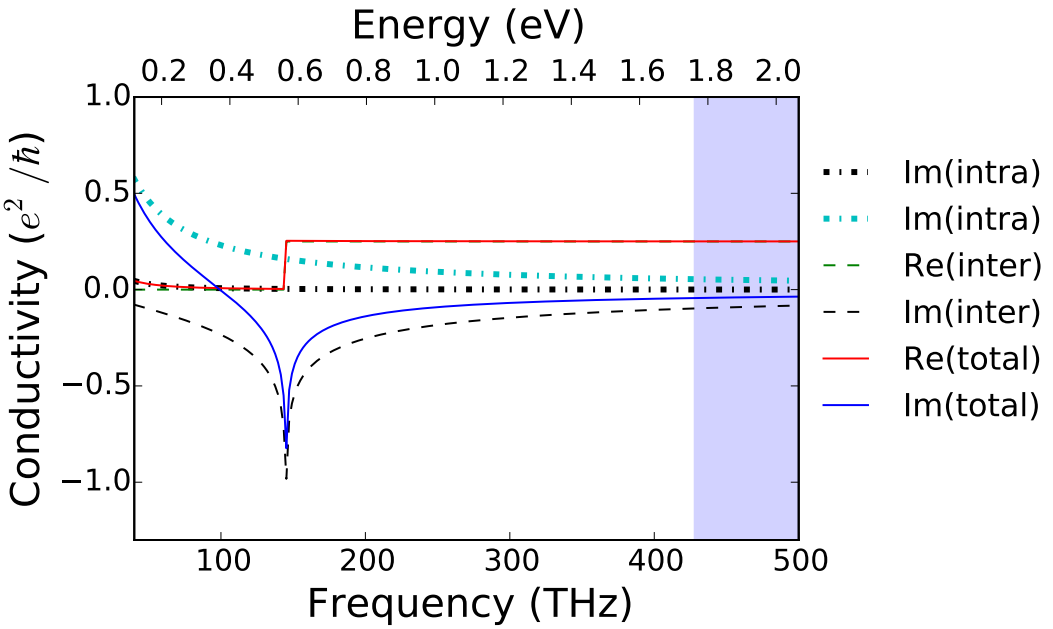

FIGURE 1.4: Conductivity of graphene given by Equation (1.8). with $E_f = 0.3\,\mathrm{eV}$ and $\tau = 50 \times 10^{-15}\,\mathrm{s}^{-1}$. At low frequencies, <130 THz, intraband contributions dominate, at frequencies >200 THz interband contributions dominate. The onset of the optical frequency regime (700 nm), where the absorption of graphene becomes constant, is shown as the shaded blue region.

$$\omega_p = \sqrt{\frac{e^2 E_f}{\pi \epsilon_0 \hbar^2 (\epsilon_1 + \epsilon_2)} q}, \tag{1.12}$$

where q is the surface plasmon wavevector, ϵ_1, ϵ_2 are the permittivities of the dielectric regions surrounding the graphene and n_0 is the electronic density of the graphene. While the plasmon frequency still scales as $\omega_p = \sqrt{q}$, the linear band structure means the electron density in graphene is linked to the Fermi energy as, $E_f = v_f \hbar \sqrt{n_0 \pi}$ [68] with $v_f = 1 \times 10^6\,\mathrm{ms}^{-1}$ the Fermi velocity, so the plasmon frequency scales as $\omega_p = n_0^{1/4}$, in contrast to metallic plasmons where $\omega_p = \sqrt{n_e}$, see Equation (1.1).

1.1.4 Graphene Plasmons

Even from a brief inspection of Equation (1.12), it can be seen that graphene plasmons will display interesting physics. Directly, it can be seen that the frequency of a plasmon in graphene depends on the Fermi level. As discussed in relation to Figure (1.3), the Fermi level of graphene can be altered post-fabrication with FET devices. This allows the plasmon frequency of graphene to be altered in-situ, which is a stark contrast to metallic plasmons [41].

The change in frequency response has been demonstrated to be approximately 1.5 times the resonant FWMH, representing a huge degree of tunability, opening new opportunities for novel technologies [128].

Hidden in Equation (1.12) is a description of the high field confinement of graphene plasmons [120]. The field confinement is described by comparing the plasmon wavevector q to the wavelength of light used to excite it. By inserting an easily accessible Fermi level of graphene, $E_f = 0.2\,\mathrm{eV}$, [129][130] into Equation (1.12), the confinement can be demonstrated. For this level of doping, the plasmon wavelength is found to be 33 times smaller than the free space equivalent at 6 THz. This degree of confinement is not only larger than can be achieved in metallic plasmons but importantly occurs deep into the infrared frequency regime, where the confinement of metallic plasmons becomes much worse [131]. As graphene displays plasmons at infrared frequencies it is of great interest for the wide range of useful technological applications that lie in this frequency range [132] [133]. For example, a recent, graphene-based light modulator has demonstrated the combination of low power and small physical footprint that graphene based devices can offer [134].

The combination of the high field confinement and the sensitivity of the plasmon frequency to the Fermi level, at infrared frequencies, makes surface plasmons in graphene suitable for sensing applications. FTIR spectroscopy as a sensing tool makes use of the unique fingerprint molecules have at infrared frequencies [135] [136]. As FTIR spectroscopy is a well established technique, the ability for graphene to integrate well with this technique is very attractive. A recent demonstration using FTIR spectroscopy has shown that an un-optimised graphene based biosensor can achieve femtomole sensitivity; this sensitivity is comparable to that achievable in mass spectrometry without the required expensive equipment [137][138][139]. Graphene plasmons have been experimentally used by Rodrigo et al. to extend the effectiveness of FTIR spectroscopy by improving the sensitivity of the measurement [140] and by Li et al. demonstrate how graphene plasmons can be used as a label-free and molecule-specific detection tool [141].

However, as discussed in relation to Equation (1.12), the wavevector of graphene plasmons is much greater than that of the free space light. Whilst this larger wavevector has the enormous benefit of surface plasmons in graphene having greatly enhanced fields, providing the required momentum to the incident light presents a serious challenge for exciting graphene plasmons. One method for providing the required momentum to the incident light is by using the enhanced near fields created from a very sharp tip, allowing graphene plasmons to be imaged spatially [142][143]. From these spatial images, the distance over which plasmons can propagate over can be measured. The propagation distance is a useful parameter for quantifying fundamental properties, such as losses, and in determining the

practical use for graphene plasmons. In both the experiments of Fei et al. and Chen et al. this propagation distance was measured to be several times the plasmon wavelengths [143]. The observation of graphene plasmons displaying a long propagation length suggests that surface plasmons in graphene suffer from low losses when compared to metallic plasmons [131][144][145]. These low losses, when combined with the observed large field enhancement, provide a potential avenue for investigating single photon optics [146][147].

Another method for exciting surface plasmons is through directly patterning a graphene sheet. Ju et al. showed how an array of graphene ribbons can support graphene plasmons [148]. This experiment also demonstrated that the resulting plasmon resonance occurs across a broad range of terahertz frequencies and at room temperature, which is promising for technological applications [148]. Following the demonstration of ribbons supporting plasmons, a large range of other pattern geometries, such as disks [149][150][151], antidots [152][153] and patches [154] [155] have been investigated. These were investigated theoretically with the aim of increasing the absorption properties of surface plasmons. Both ribbons and disk geometries have been modelled to exhibit perfect absorption [156] [150].

Being atomically thin, graphene offers an avenue for achieving unique spatial patterns in the surface properties of a material. This patterning is of interest to the field of transformation optics. The low losses of plasmons in graphene offers unique possibilities for wave guiding, greatly enhancing current performance, reducing the thickness of material required [157] and allowing new cloaking applications [158]. Additionally, the use of carefully designed back-gates allows the Fermi level in graphene to be actively controlled with high spatial resolution [159]. Vakil and Engheta suggested a route for creating traditional optical devices, such as lenses, in an atomically thin layer [160]. Additionally, Wu and Gao suggest how these advanced surfaces might be fabricated [161]. The dynamic control over the electric properties of graphene has immediate applications for creating switchable devices [162]. The results of designing a spatial variation in the properties of graphene to modify the plasmonic response of graphene will be presented in Chapter 3.

1.2 Nonlinear Response of Graphene

For the previously discussed physics, the polarisation induced by an electric field is sufficiently described as being linearly proportional to the applied electric field. As might be expected, this linear relationship is only an approximation. The field of nonlinear physics has a long history, the early part echoing that of graphene, with early progress being limited by the fabrication techniques required [163][164]. Presently, nonlinear physics underpins many technologies. Examples include the Kerr effect and the resulting self focusing behaviour of light with in these nonlinear materials, enabling the creation of ultrashort

laser pulses [165][166][167]. Another important effect is the change in birefringence, due to an applied electric field, known as the Pockels effect which is vital for laser technology [164]. This thesis will focus on the nonlinear generation of optical frequencies in graphene. The invention of pulsed laser sources allowed intense electric fields to be created with the magnitude of the electric field in these pulses is of the order of $1 \times 10^7\ \mathrm{Vm}^{-1}$. With these large electric fields, the linear relationship between the polarisability and the electric field can be investigated. Following the ground breaking observation of second harmonic generation by Franken et al., a more complete description of the polarisation was required [168]. To explain the observation of a second feature with half the wavelength of the incident pulses requires a nonlinear description of interaction between the incident light and the material. The nonlinearity is introduced by extending the definition of the induced polarisation with a power series expansion,

$$P(t) = \epsilon_0(\chi^{(1)}E(t) + \chi^{(2)}E(t)^2 + \chi^{(3)}E(t)^3 + ...), \tag{1.13}$$

where $\chi^{(2)}$ and $\chi^{(3)}$ describe the second and third order susceptibilities of the material. For typical glass-like materials $\chi^{(2)} \approx 1 \times 10^{-12}\ (\mathrm{mV}^{-1})$ and $\chi^{(3)} \approx 1 \times 10^{-20}\ (\mathrm{mV}^{-1})^2$ [169]. Treating these nonlinear susceptibilities as constants, as in Equation (1.13), is a simplification, as this ignores the full vector nature and frequency of the multiple incident electric fields involved in different nonlinear processes just as is the case for the linear susceptibility [28]. For a full description, $\chi^{(2)}$ and $\chi^{(3)}$should be treated as tensors [170]. Due to the fixed geometry used in this thesis, these nonlinear susceptibilities will be treated as constants. However these constant susceptibilities are still very useful and help to classify the "order" of a nonlinear processes and describes the number of photons involved in the process. More complex examples exist where the frequencies produced, act as new source frequencies for subsequent nonlinear processes [171][172]. As an introduction it is helpful to introduce common examples of second order processes, involving two photons, and a third order process, involving three, are shown in Figure (1.5). Second harmonic generation (SHG), Figure (1.5a), involves two incident photons which combine to generate a new photon at twice the input frequency [164]. As mentioned earlier, second harmonic generation has applications in microscopy, for background free measurements and has been demonstrated as a technique for imaging live cells [173][174].

Sum frequency generation (SFG), Figure (1.5 b), is a very similar effect where two photons with unequal frequencies combine to create a photon with the frequency equal to the sum of the incident frequencies. A mathematical description for these second order nonlinear processes, known as the coupled-wave equation can be developed from Maxwell's equations as outlined by Boyd [169]. The second order process depicted in Figure (1.5c)

is subtly different to SHG and SFG in that the generated frequency, ω_1 is lower than the input frequency. This process involves a source, or pump, driving the creation of a new beam, or signal, via a third, or idler, frequency and is also known as optical parametric amplification (OPA). This process allows a laser output to be tuned over a large range of optical and infrared wavelengths [175]. Figure (1.5d) shows the simplest third order effect and illustrates the origin of nonlinear frequency generation, where the generated frequency is three times the input frequency. It is easy to see that variations on SFG and DFG can occur as third order processes with the addition of an extra photon and can result in a great deal more complexity. The quantum mechanical models of nonlinear processes are complicated, so the current frontier is concerned with extending these models to find a more fundamental description and attempting to investigate extreme length scales with the associated large nonlinearity [176][177]. It is important to note that the efficiency of these nonlinear processes is highly dependent on the phase matching between the incident and generated frequencies through the nonlinear material. A perfectly phase-matched conditions, can bring enormous an increase in the efficiency of the nonlinear process [178]. With this context, investigating the nonlinear properties of an atomically thin layer of graphene seems like an odd choice.

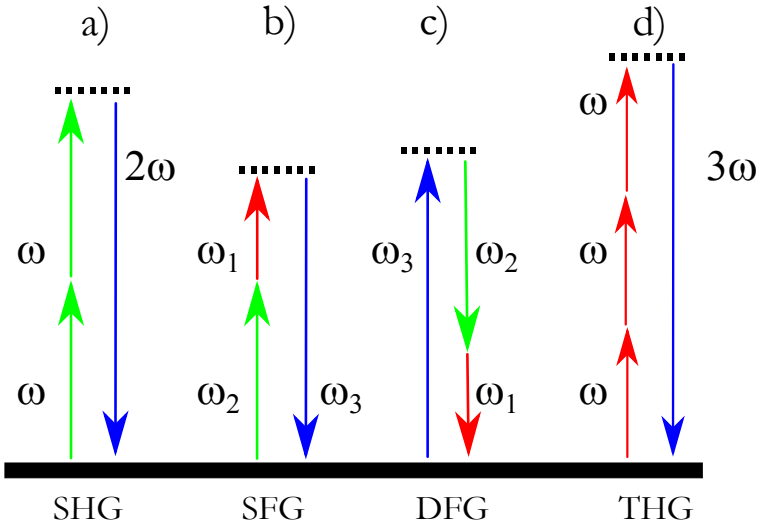

FIGURE 1.5: A Jablonski diagram of nonlinear processes. a) Second harmonic generation (SHG). Two photons of equal frequency (green arrow) ω combine to create a new photon of 2ω (blue arrow). b) Sum frequency generation (SFG). Two photons of unequal frequency ω_1 and ω_2 (green and blue arrow respectively) combined to create a photon with frequency $\omega_3 = \omega_1 + \omega_2$. c) Difference frequency generation (DFG). A photon with frequency ω_3 combines with ω_2 to create a new photon ω_1 so that $\omega_1 = \omega_3 - \omega_2$. d) Third harmonic generation (THG) as a third order version of SHG from a), taking three photons of equal frequency to create a fourth photon of 3ω.

While the invention of the laser has made investigations into nonlinear wave-mixing physics much easier, studies have focused on materials which display an intrinsically large

value of $\chi^{(3)}$. When introducing the optical absorption of graphene, the focus was on the striking, frequency-independent, behaviour of absorption of $\pi\alpha \approx 2.3\%$. Initially this might suggest that graphene interacts weakly with electromagnetic radiation and that the $\chi^{(3)}$ of graphene is also small. However, considering this interaction is mediated by a single atomic layer, graphene was predicted to have a surprisingly large $\chi^{(3)}$[179] [180], as was subsequently observed experimentally [181]. To date there have been several experiments and theoretical investigations into the various nonlinear processes in graphene, from two photon absorption [182] to difference frequency generation [183].

These nonlinear wave-mixing processes are known as parametric as they exploit transitions to virtual energy levels. Conversely, processes which use real energy levels are known as nonparametric [169]. An important nonparametric effect is saturable absorption, where the absorption of a material is decreases with increasing laser intensity. Saturable absorption underpins passive mode-locking technology used for generating ultrashort laser pulses, as an improvement compared to active mode-locking [184][185]. Constructing a laser cavity from a saturable absorber reinforces pulse propagation through the cavity by providing minimum losses for the peak intensity in the cavity. Additionally the saturable absorber acts to shorten the leading edge of the pulse every round trip of the cavity. One promising technological application for graphene is as a saturable absorbing material for ultrashort pulse generation. The linear band structure, shown in Figure (1.2), means that graphene e-h pairs can be resonantly excited for a broad range of wavelengths, in contrast to traditional semiconductor saturable absorber mirrors (SESAMs) [186]. Graphene has been successfully incorporated into laser designs with technologically relevant output wavelengths, ~1.5 µm and ~400 fs pulse durations [187][188][189]. Further studies have shown that a graphene-based saturable absorber can be incorporated to produce ultrafast pulses with a continuously tunable output wavelength in the range of $1570\,\mathrm{nm}$ to $1600\,\mathrm{nm}$ [190].

However, this thesis focuses on third harmonic generation. Mikhailov predicted that the third order susceptibility, $\chi^{(3)}$, of graphene is large, especially in comparison to dielectric materials [191][192]. The strength of the nonlinear interaction arises from the current that a uniform electric field, $\bar{E}(t) = E_0 \cos(\omega t)$ generates from the motion of the electrons in graphene. The linear energy spectrum, as shown in Figure (1.2b), means the current generated will contain surprisingly large higher-order harmonics, to account for the motion of electrons whose velocities can instantaneously switch from $+1 \times 10^6\,\mathrm{ms}^{-1}$ to $-1 \times 10^6\,\mathrm{ms}^{-1}$. This considerable acceleration leads to the emission of electromagnetic radiation at these higher-order harmonic frequencies [180]. Meanwhile, third harmonic generation in graphene has been experimentally investigated in mechanically exfoliated graphene flakes by Kumar et al. [193] and studied theoretically by Zhang et al, with a quantum-dynamical theory [194] and Cheng et al. with a perturbative calculation [195].

Whilst these studies report a comparatively large value of $\chi^{(3)}$ in graphene, the absolute energy conversion is limited by the atomically thin nature of graphene. Therefore, methods for enhancing the nonlinear effects are desirable. One such approach to enhance these nonlinear interactions in graphene is to utilise a planar cavity [196]. To exploit this, Savostianova and Mikhailov theoretically proposed a layered structure, consisting of a graphene layer combined with a dielectric on top of a gold film. Compared to utilising surface plasmons, a previously demonstrated method of enhancing nonlinearity [197], a layered structure removes the precise requirements on the frequency and wavevector required for coupling incident photons to surface plasmons. Such a planar cavity is predicted to enhance the third harmonic generation from graphene by up to two orders of magnitude [196]. Measurements from such a planar cavity is presented in Chapter 4.

1.3 Photoluminescence

The interaction between light and a material can reveal intricate properties without the intense electric fields used to access the nonlinear behaviour. Photoluminescence describes the phenomena of a material absorbing a light and emitting light of a different wavelength and was first observed in 1565 [198]. Fluorescence occurs when an incident photon with energy greater than the first excited electronic state is absorbed by a fluorescent molecule. The absorption of this photon promotes the fluorescent molecule from the ground state, S_0, to a higher, unstable electronic level S_1. The molecule rapidly loses energy non-radiatively through these vibrational energy levels [199]. The unstable state of S_1 decays back to the ground state S_0, by emitting a lower energy photon [200]. The time scale for the fluorescent molecule to decay from the excited energy level back to the ground state is known as the fluorescence lifetime and is typically on the order of nanoseconds [201]. The difference in energy between the incident and emitted light is known as the "Stokes shift" and has useful practical applications. The shift to longer wavelengths of the emitted light, relative to the incident wavelength, allows for effective filtering of the incident beam. This filtering allows fluorescence measurements to be performed virtually free from background noise [202]. With suitable filtering equipment, the ratio between wanted and unwanted light collected from the sample can approach $1{:}10^5$ [200][203]. In addition to the background free measurements, the surface chemistry of fluorescent molecules makes them particularly suited to biological experiments as they exclusively bind to very specific proteins [204][205]. As a result, fluorescence microscopy has become a universal imaging tool that is central to modern biomedical research [5]. Fluorescence microscopy has been improved in many ways; from a technological perspective [206][207] and via the use of multiple, nonlinear excitations, [208][209] [210][211] and sophisticated post-processing [1][209].

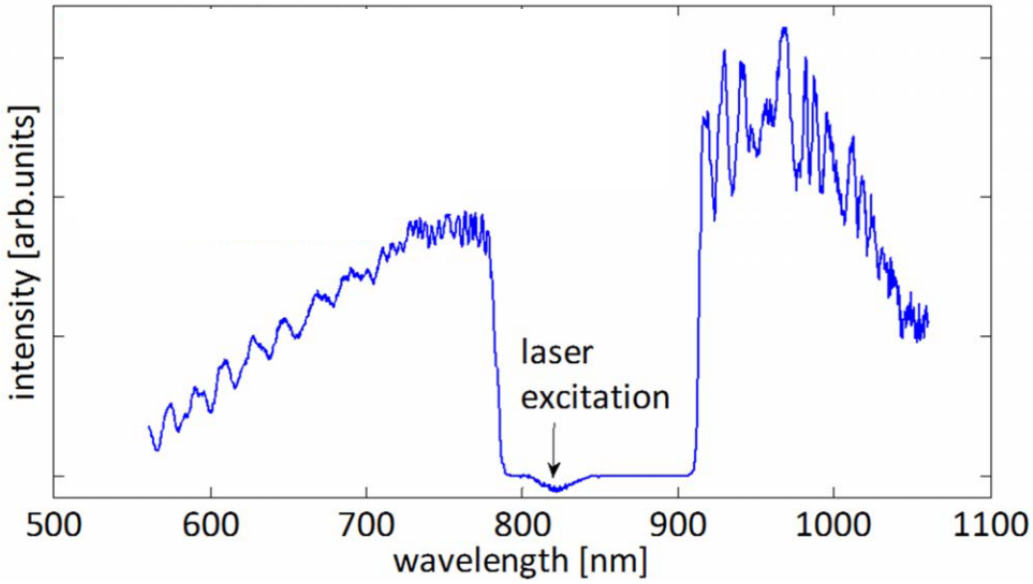

FIGURE 1.6: An example emission spectrum from a single graphene layer from a 7 ps pulse, with a central wavelength of 820 nm (marked with a black arrow). Note the broad spectrum across which the luminescence is displayed and the significant contribution for wavelengths shorter than the excitation wavelength. The dip between 800 nm and 900 nm is a result of filtering the incident beam. The rapid oscillations are attributed to an artifact arising from multiple reflections within the experiment. Image adapted from the experiments of Stöher et al. [212].

In addition to specific fluorescent molecules, some semi-conducting materials also display fluorescent behaviour, e.g. gallium arsenide (GaAs) [213]. GaAs is a direct bandgap material resulting in efficient luminescence [128]. The compatibility of GaAs with silicon based devices and the control over the optical properties that can be achieved with doping, make GaAs an interesting material [214][215][216]. To generate luminescence, light with energy larger than the bandgap energy is used to excite electron-hole (e-h) pairs. The excited carriers scatter, creating a thermal distribution of carriers [213]. These e-h pairs then spontaneously recombine to emit light. Since the emitted luminescence is tied to the charge carrier dynamics in a material, detailed information about the material such as the band structure, the nature of defects and fundamental properties of electron dynamics can be extracted from photoluminescence measurements.

Despite the lack of a bandgap, graphene does have unique luminescent properties which can be revealed by using ultrafast laser pulses. In other semiconducting materials, luminescence arises from the light emitted from excited carriers as they recombine across the bandgap between the conduction band and valence band [217]. As graphene lacks a bandgap, the mechanism for emitting light is not immediately available, so luminescence

from graphene is not expected. However, ultrafast pulses can cause graphene to emit luminescence over a spectrally broad range of frequencies [218]. The broad spectrum obtained from measurements of Stöhr et al. using a 7 ps pulse is shown in Figure (1.6). Stöhr et al. used a 7 ps pulse with a central wavelength of 820 nm to excite a layer of graphene and the resulting light was directed onto a CCD spectrometer to record the emitted spectrum. Significantly, the emitted luminescence spectrum contains a sizable contribution from wavelengths higher in energy than the excitation wavelength, i.e. wavelengths between 550 nm and 750 nm on Figure (1.6). Additionally, no change in the spectral shape of the luminescence was observed for a range of incident pulse energies. This observation demonstrates that the observed luminescence is a not a result of black-body emission [212]. The luminescence arises instead from fundamental charge scattering mechanisms within the graphene layer, allowing these to be studied. As shown in Figure (1.7), upon ultrafast excitation, $\hbar\omega_1$, a large number of e-h pairs are created. Through e-e scattering these rapidly, ~10 fs, form a thermal distribution, (red shaded region) [219][220]. This broad distribution of e-h pairs recombine to create the observed luminescence over a wide spectrum, from $\hbar\omega_2$ to $\hbar\omega_3$.

While measurements using femtosecond pulses show similar spectral behaviour to the luminescence emitted from the picosecond pulses described, the quantitative behaviour is different due to the shorter timescale [221]. These timescales can be accessed with a two-pulse, pump-probe measurement to resolve the early dynamics. The results of Brida et al. show that carrier dynamics in graphene occur on an extremely short timescale, electron-electron scattering occurring at ~10 fs before electron-phonon scattering on ~100 fs before e-h recombination occurs, emitting the broad band fluorescence[222].

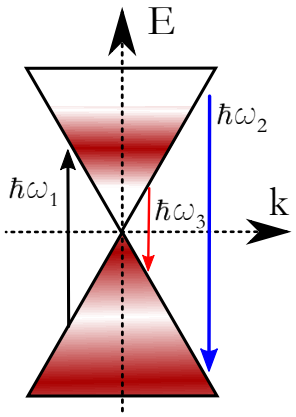

FIGURE 1.7: Origin of ultrafast photoluminescence from the linear band structure of graphene. Ultrafast excitation, $\hbar\omega_1$, excites e-h hole pairs. These rapidly scatter to form a thermal distribution. Upon recombination the luminescence is emitted across a broad spectral range from $\hbar\omega_2$ to $\hbar\omega_3$

The luminescence emitted from graphene contrasts with traditional fluorescence microscopy, which relies on exciting a fluorescent molecule with an incident beam. Studies into controlling luminescence behaviour began with Purcell who manipulated the rate of emission of excited dipoles [223]. This experiment suggested that the decay rate of an excited dipole was not a fundamental property of the molecule. This claim is supported by the theoretical work of Kleppner, who proposed large modifications in the rate of emission of an excited molecule are possible [224]. Experimentally, a carefully prepared cavity was shown to influence the transition rate of excited sodium atoms [225].

In addition to radiative decay, an excited molecule, or donor, can also decay non-radiatively by coupling with an acceptor state. This donor-acceptor pair is commonly between two fluorescent molecules but has also been observed between metallic nanoparticles [226] [227]. Andrew and Barnes experimentally demonstrated control of this Förster energy transfer by incorporating optical dyes into a tunable cavity [228]. Whilst non-radiative decay might not be desirable for confocal imaging, this quenching behaviour of the radiative decay is very sensitive to the distance between the excited molecule and the acceptor. This extreme distance sensitivity means that the quenching of fluorescent molecules has the potential to be used a distance sensing tool.

The system of a molecule, described as a dipole, in close proximity to a metal surface has been heavily studied in the context of surface enhanced Raman spectroscopy (SERS) [229] [230] [231] [232] and reviewed in detail by Metiu [233]. This model starts by considering the electromagnetic fields incident on a molecule, to calculate the resulting polarisation and the emitted field. Bringing a surface close to a molecule can result in a variety of effects, from acting as a mirror for the emitted electromagnetic fields, or in the case of metals, coupling to electron-hole pairs, which quenches the luminescence emitted from the molecule [5]. The specific case of a molecule near to a layer of graphene was studied analytically by Gómez-Santos and Stauber who aimed to elucidate the mechanism that allows an atomically-thin layer to be able to produce a significant quenching effect observed in several fluorescence experiments [23] [234] [235]. The dependence of the quenching effect on the separation, d, from the graphene layer that Gómez-Santos and Stauber theoretically derive is $\gamma_{quench} \propto (\lambda/d)^4$ and is valid for unusually small separations. At these small separations the quenching effect becomes very large which supports the experimental observations [236]. Importantly, the dependence of the quenching effect on the distance between the layer of graphene and the excited molecule, d, was observed to scale as d^{-4}. This new scaling behaviour was demonstrated by Gaudreau et al. with graphene [237] [238] [239][240][241]. This dependence of the quenching effect on the distance between the graphene layer and the excited molecule allowed Reserbat-Plantey et al. to perform sensitive nanoscale distance measurements, with interesting potential for

single photon experiments [242]. The quenching effect of graphene on the fluorescence was then measured for impressively large distances, up to 30 nm, by Gonçalves et al. [243]. Additionally, stacking of monolayer graphene, into multilayer graphene, allows for further control over the quenching properties of graphene. Increasing the number of layers in a multilayer stack was shown to increase the quenching effect, as each layer adds additional decay channels for the excited molecule [244].

The fluorescence quenching of graphene can also be modified though applying a sufficiently large Fermi level [245]. As introduced with Figure (1.3), the Fermi level can be changed post fabrication, providing a method of control over the electrical properties of graphene [107][57]. The large changes in Fermi level that are possible in graphene, for example with ionic top gates [246], allow for an interesting combination with fluorescent molecules. For sufficiently large Fermi levels, equivalent to the photon emission of a fluorescent molecule in the visible frequency range, i.e. $|E_f| > \hbar\omega$ [247], there is a decrease in the quenching effect of graphene. By moving the Fermi level away from the Dirac point, where the cones touch in Figure (1.2b), the electronic states which the fluorescent molecule decays through are blocked, reducing the quenching. This gate-voltage tunable quenching effect has been observed by Lee et al. [247]. While Lee et al. compare the the gate-voltage behaviour of two different fluorescent molecules, Tielrooij et al. chose a molecule with a much lower excitation energy [245]. The energy of emission coupled with the large shifts in Fermi level gives access to a regime in which the Fermi level is above the frequency of emission, allowing the excitation of surface plasmons. In contrast, Chapter 5 explores an alternate method for controlling fluorescence with a layer of graphene, by correlating spatial variations in intrinsic strain with the variation in the fluorescence profile.

This chapter has dealt with the basics of the honey-comb arrangement of carbon atoms in graphene and how this leads a linear band structure. This linear band structure is the origin of many interesting light-matter interactions, such as the ability for graphene to support infrared plasmons, strongly nonlinear behaviour and unique photoluminescence properties. The next chapter will discuss the techniques used to investigate these phenomena, from computational modelling through to experimental techniques and the required device fabrication.

Chapter 2

Methods

2.1 Modelling

The nanostructuring of graphene required to excite plasmons, is technologically challenging. This means that the desired parameters must first be carefully designed. Numerical modelling approaches provide a useful tool for optimising this complicated fabrication procedure. In this thesis, two modelling techniques are presented: a semi-analytical modal-matching technique and a finite difference time domain (FDTD) method. Compared to FDTD, the speed of the modal-matching technique aids the investigation into a wide range of parameters. Despite the computational cost, the FDTD model directly allows an investigation into the nonlinear properties of graphene. The flexibility of FDTD model also allows for an easy investigation into arbitrary geometries.

2.1.1 Modal Matching Model

The system of interest is one of a continuous layer of graphene with an array of alternating regions of conductivity with sharply defined regions, as shown as in Figure (2.1b). In order to analyse this system, a full-wave modal-matching model is developed. Key components of this model are the form of the conductivity, Equation (2.8), and how the transmission is calculated, Equation (2.34). Starting with Maxwell's equations,

$$\vec{\nabla} \times \vec{\mathbf{E}} = -\frac{\partial \vec{\mathbf{B}}}{\partial t}, \tag{2.1}$$

$$\vec{\nabla} \times \vec{\mathbf{B}} = \mu_0 J_f + \frac{1}{c^2}\frac{\partial \vec{\mathbf{E}}}{\partial t}, \tag{2.2}$$

and the allowed transverse magnetic (TM) surface mode which is given by $\vec{\mathbf{E}} = (E_x, 0, E_z)$ and $\vec{\mathbf{B}} = (0, B_y, 0)$ with a time dependence of $e^{-i\omega t}$, the electric and magnetic fields become,

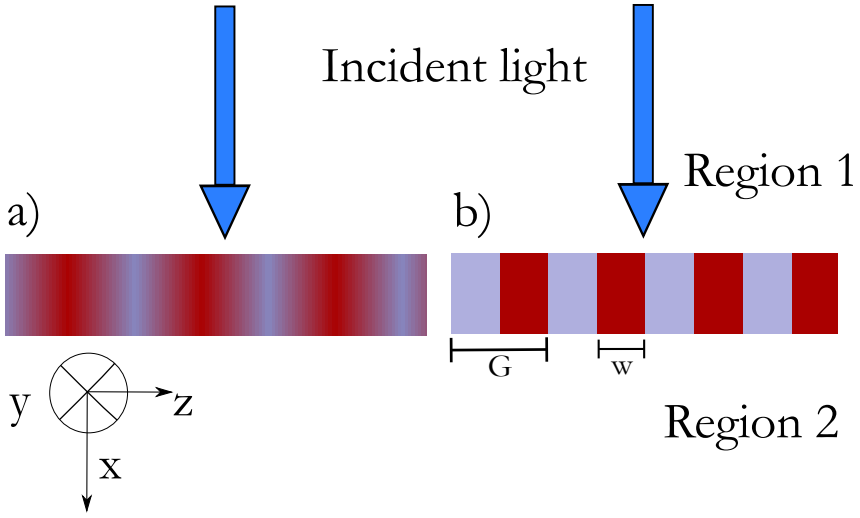

FIGURE 2.1: A schematic of graphene sheets with a periodically modulated conductivity with a period of G and a width of w. a) Conductivity profile described with a single Fourier term. b) Conductivity profile with many Fourier terms. Region 1 is above the graphene layer and region 2 is below the graphene layer.

$$\partial_z E_x^{(\eta)} - \partial_x E_z^{(\eta)} = i\omega B_y^{(\eta)}, \tag{2.3}$$

$$\partial_y B_z^{(\eta)} - \partial_z B_y^{(\eta)} = \frac{-i\omega}{c^2}\epsilon_{(\eta)} E_x^{(\eta)}, \tag{2.4}$$

$$\partial_x B_y^{(\eta)} - \partial_y B_x^{(\eta)} = \frac{-i\omega}{c^2}\epsilon_{(\eta)} E_z^{(\eta)}, \tag{2.5}$$

with the value of $\eta = 1, 2$ depending on the region considered, as shown in Figure (2.1). The in-plane wave vector is defined as,

$$q_n^{(\eta)} = \sqrt{\frac{\omega^2}{\nu_{(\eta)}^2} - (k_0 \sin\theta - nG)^2}. \tag{2.6}$$

where $\nu_\eta = \sqrt{1/(\mu_0 \epsilon_\eta)}$ and the free space wave vector is, $k_0^2 = \omega^2 \epsilon_1 / c^2$ or $q_0^{(\eta)} \equiv k_0 \cos\theta$ and G is the period of the graphene ribbons as shown in Figure (2.1). With this description of the fields in place, the material properties of the graphene are now considered. Since the range of frequencies considered is below the interband absorption threshold, the conductivity of graphene can be modelled using the intraband expression,

$$\sigma_g = \frac{e^2 E_f}{\pi\hbar} \frac{i}{(\omega + i\tau^{-1})}, \tag{2.7}$$

where the scattering rate, τ, is assumed to be determined by impurity scattering, so that $\tau =$

$\mu E_f/e\, v_f^2$ [248], where E_f is the Fermi level and v_f is the Fermi velocity = $1 \times 10^6\,\mathrm{ms}^{-1}$. The mobility, μ, is set to $1000\,\mathrm{cm}^2\mathrm{V}^{-1}\mathrm{s}^{-1}$, which is typical of chemical vapour deposition (CVD) graphene [122]. In order to describe a conductivity profile of a periodically alternating array of high and low conductivity regions as shown in Figure (2.1) the conductivity is described as $\sigma(z) = s(z)\sigma_g$, where σ_g is the intraband expression Equation (2.7). A central part of the modal-matching model is the full form of the spatial profile used to describe the periodic regions in the conductivity, of a graphene layer lying in the zy-plane, is given by a rectangular wave,

$$s(z) = \sum_n A_0 \left[\frac{\mathrm{w}}{G} + \frac{1}{n\pi} \sin\left(\frac{2\pi n \mathrm{w}}{G}\right) \cos\left(\frac{2n\pi}{G} z\right) + \frac{1}{n\pi}\left(1 - \cos\left(\frac{2\pi n \mathrm{w}}{G}\right)\right) \sin\left(\frac{2n\pi}{G} z\right) \right]. \tag{2.8}$$

represented using a Fourier sum to n, where G, is given by $\mathrm{G} = 2\pi/\mathrm{w}$, and w, is the fraction of the high conductivity region as shown in Figure (2.1b). A_0 is the difference between the high and low conductivity region, and z is the in-plane spatial dimension. Figure (2.2) shows the difference in the conductivity profiles of Figure (2.1a, b) more explicitly, with the red shaded region denoting the low conductivity region and the blue shaded region the high conductivity region. A low number of Fourier terms describes a conductivity profile with a soft edge between the high and low conductivity areas and increasing the number of Fourier terms sharpens this edge. Including an increasing number of Fourier terms and including more than 10 yielded a negligible effect on the results of Chapter 3. In practice, a modulated conductivity, such as in Figure (2.1b), could be achieved using a patterned gate [128] or functionalization [249], both utilising the distinctive dependence of the conductivity of graphene on the Fermi level. One route for fabricating such a device could be through combining electron-beam lithography and an ion gel to create the required spatially-varying top-gated structure. Consequently, realistic parameters are chosen for a system constructed using ion gel top gates [246]. The relative permittivity, $\epsilon_{(\eta)}$, of a calcium fluoride substrate, region 1, and an ion gel top gate, region 2, are both taken to be 1.96 [250][251].

With the conductivity model for graphene established, the fields above and below the graphene layer need to be defined. Starting in the region above the graphene layer, $\eta = 1$, the fields take the form,

$$B_y^{(1)} = b_i e^{izk_0 \sin\theta} e^{ixk_0 \cos\theta} + \sum_n \mathcal{A}_{n,y}^{(1)} e^{i(k_0 \sin\theta - nG)z} e^{-iq_n^{(1)} x}, \tag{2.9}$$

$$E_x^{(1)} = \mathcal{Q}_{i,x} e^{izk_0 \sin\theta} e^{ixk_0 \cos\theta} + \sum_n \mathcal{Q}_{n,x} e^{i(k_0 \sin\theta - nG)z} e^{-iq_n^{(1)} x}, \tag{2.10}$$

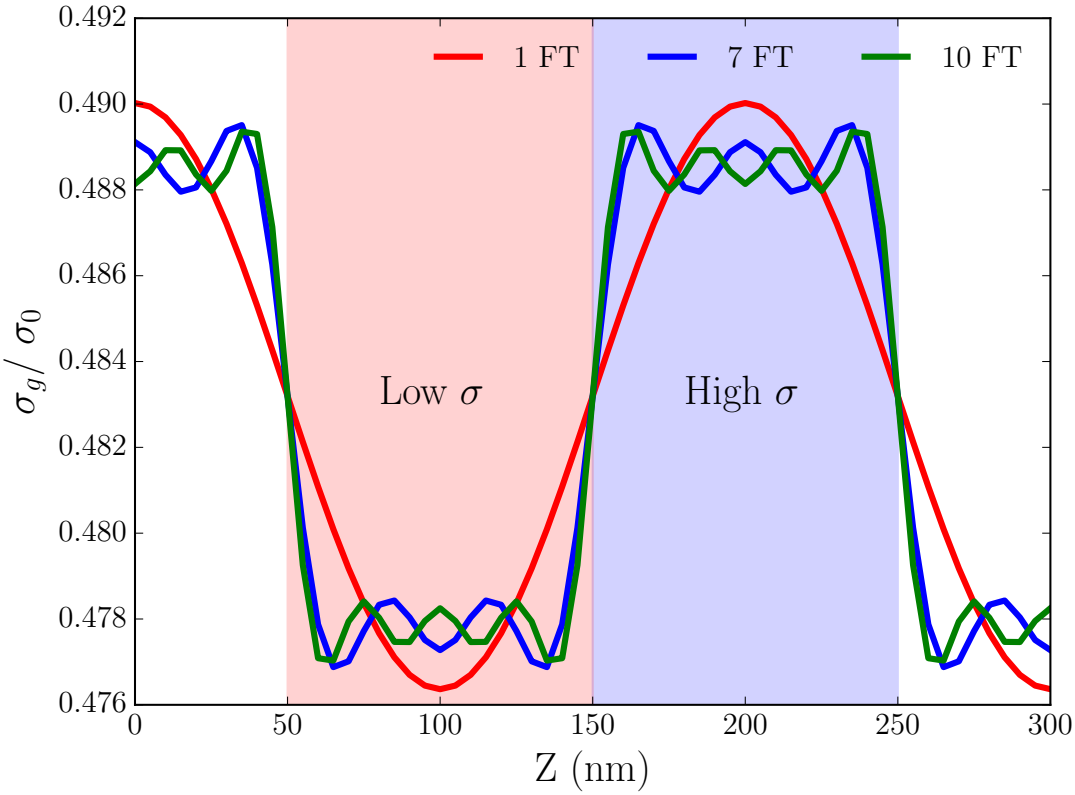

FIGURE 2.2: A plot of the spatial conductivity, σ_g, profile given by Equation (2.8) with increasing number of Fourier terms, where $\sigma_0 = (e^2/4\hbar)$. For a profile with one Fourier term (red line) has softly defined edges between the high and low regions, this is schematically represented in Figure (2.1a). Adding further Fourier terms, (7, blue line and 10 green line) sharpens the edge of the high and low conductivity regions as shown in Figure (2.1b). Adding further Fourier terms has a negligible effect on the results.

$$E_z^{(1)} = \mathcal{Q}_{i,z} e^{izk_0 \sin\theta} e^{ixk_0 \cos\theta} + \sum_n \mathcal{Q}_{n,z} e^{i(k_0 \sin\theta - nG)z} e^{-iq_n^{(1)} x}. \tag{2.11}$$

For the region below the graphene layer, $\eta = 2$, the fields take the form,

$$B_y^{(2)} = \sum_n C_{n,y} e^{i(k_0 \sin\theta - nG)z} e^{iq_n^{(2)} x}, \tag{2.12}$$

$$E_x^{(2)} = \sum_n F_{n,x} e^{i(k_0 \sin\theta - nG)z} e^{iq_n^{(2)} x}, \tag{2.13}$$

$$E_z^{(2)} = \sum_n \mathcal{P}_{n,z} e^{i(k_0 \sin\theta - nG)z} e^{iq_n^{(2)}x}, \tag{2.14}$$

Applying the form of a TM mode Equations (2.3, 2.4, 2.5), on the incident field, Equations (2.9, 2.10, 2.11), (i.e. x<0 and n=0), reduce to,

$$\mathcal{Q}_{i,x} \sin\theta - \mathcal{Q}_{i,z} k_0 \cos\theta = \omega b_i, \tag{2.15}$$

$$b_i = \frac{\omega \epsilon_1}{k_0 c^2 \sin\theta} \mathcal{Q}_{i,x}, \tag{2.16}$$

$$b_i = -\frac{\omega \epsilon_1}{k_0 c^2 \cos\theta} \mathcal{Q}_{i,z}. \tag{2.17}$$

Equating Equation (2.16), with Equation (2.17) the unknown coefficient b_i can be removed to give,

$$\mathcal{Q}_{i,x} = -\frac{\sin\theta}{\cos\theta} \mathcal{Q}_{i,z}. \tag{2.18}$$

Now consider the reflected, scattered field, (i.e. x <0, n≠0), Equations (2.12, 2.13, 2.14) become,

$$k_0 \sin\theta \mathcal{Q}_{n,x} - q_n^{(1)} \mathcal{Q}_{n,z} = \omega\, a_{n,y}^{(1)}, \tag{2.19}$$

$$k_0 \sin\theta a_{n,y}^{(1)} = \frac{\omega \epsilon_1}{c^2} \mathcal{Q}_{n,x}, \tag{2.20}$$

$$\mathcal{A}_{n,y}^{(1)} = \frac{\omega \epsilon_1 \mathcal{Q}_{n,z}}{c^2 q_n^{(1)}}. \tag{2.21}$$

Equate Equation (2.20) and Equation (2.21) to eliminate the unknown coefficient $\mathcal{A}_n$ which results in,

$$-\frac{k_0 \sin\theta}{q_n^{(1)}} \mathcal{Q}_{n,z} = \mathcal{Q}_{n,x}. \tag{2.22}$$

Now a similar procedure is applied to the region above the graphene layer, $\eta = 2$, i.e. the fields described by Equations (2.12, 2.13, 2.14) become,

$$(k_0 \sin\theta - nG)(F_{n,x}) - q_n^{(2)} \mathcal{P}_{n,z} = \omega C_{n,y}, \tag{2.23}$$

$$\frac{(k_0 \sin\theta - nG)c^2}{\omega\epsilon_2} C_{n,y} = F_{n,x}. \tag{2.24}$$

Equating Equation (2.23) and Equation (2.24) removes another unknown coefficient to become,

$$C_{n,y} = -\frac{\omega c^{-2}\epsilon_2}{q_n^{(2)}} \mathcal{P}_{n,z}. \tag{2.25}$$

2.1.2 Boundary Conditions at the Graphene Layer

In order to solve these equations with all the unknown Fourier coefficients, extra information is required. This information comes from considering the boundary conditions of the electromagnetic fields at the graphene layer. First, the electric field must be continuous across the graphene layer, the following boundary condition can be imposed,

$$E_z^{(1)} = E_z^{(2)}. \tag{2.26}$$

Explicitly, this is equated as,

$$\mathcal{Q}_{i,z} e^{izk_0 \sin\theta} e^{ixk_0 \cos\theta} + \sum_n \mathcal{Q}_{n,z} e^{i(k_0 \sin\theta - nG)z} e^{-iq_n^{(1)}x} = \sum_n \mathcal{P}_{n,z} e^{i(k_0 \sin\theta - nG)z} e^{iq_n^{(2)}x}. \tag{2.27}$$

Equation (2.27) has two important conditions to consider, normal incidence, $n = 0$, when $E_{0,z} = \mathcal{P}_{0,z} - E_{i,z}$, and the remaining terms with, $n \neq 0$, where $E_{n,z} = \mathcal{P}_{n,z}$. A second boundary condition arises from considering the continuity of electric charge in the graphene layer,

$$B_y^{(1)} - B_y^{(2)} = -\mu_0 \sigma^{(1)} E_z^{(2)}, \tag{2.28}$$

which becomes,

$$b_i + \sum_n (a_{n,y}^{(1)} - (C_{n,y} + D_{n,y}))e^{-inGz} = -\mu_0 \sum_{p,n} \sigma_{n-p}^{(1)} (\mathcal{P}_{p,z} + J_{p,z}) e^{-inGz}, \tag{2.29}$$

where the conductivity as defined in Equation (2.7), has been expressed as a Fourier series with p = $-\infty$ to ∞ and the Fourier series for the electric field n= $-\infty$ to ∞. Using Equation

(2.17) for b_i, and Equation (2.21) for $\mathcal{A}^{(1)}_{0,y}$, combined with Equation (2.25) and Equation (2.27) a continuity equation can be produced, for $n = 0$,

$$\frac{\omega\epsilon_1}{q_0^{(1)}}\mathcal{P}_{0,z} + \frac{\omega\epsilon_2}{q_0^{(2)}}\mathcal{P}_{0,z} + \frac{1}{\epsilon_0}\sum_p \sigma_{-p}\mathcal{P}_{p,z} = \frac{2\omega\epsilon_1}{k_0\cos\theta}\mathcal{Q}_{i,z}. \tag{2.30}$$

For $n \neq 0$ the continuity equation becomes,

$$\frac{\omega\epsilon_1}{q_n^{(1)}}\mathcal{P}_{n,z} + \frac{\omega\epsilon_2}{q_n^{(2)}}\mathcal{P}_{n,z} + \frac{1}{\epsilon_0}\sum_p \sigma_{n-p}\mathcal{P}_{p,z} = 0, \tag{2.31}$$

The continuity equations, Equation (2.30) and Equation (2.31), can be recast into a matrix form in order to solve them, for the terms, $n = -1, 0, 1$. These become,

$$\begin{pmatrix} \Phi_{-1} & -\gamma & 0 \\ \gamma & \Phi_0 & -\gamma \\ 0 & \gamma & \Phi_1 \end{pmatrix} \begin{pmatrix} \mathcal{P}_{-1} \\ \mathcal{P}_0 \\ \mathcal{P}_1 \end{pmatrix} = \begin{pmatrix} 0 \\ \frac{2\omega\epsilon_1}{k_0\cos\theta}\mathcal{Q}_{i,z} \\ 0 \end{pmatrix}, \tag{2.32}$$

where the symbols have the following meaning,

$$\gamma = \frac{i4\sigma_g\eta}{2\pi}, \qquad \Phi_n = \left(\frac{\omega\epsilon_1}{q_n^{(1)}} - \frac{\omega\epsilon_2}{q_n^{(2)}} + \frac{\sigma_g}{\epsilon_0}\right). \tag{2.33}$$

Since Equation (2.32) is in the form of Ax=b, it can be evaluated through standard numerical routines found in MATLAB [252]. Finally, once the unknown Fourier coefficients have been found, they can be used in Equations (2.3, 2.4, 2.5) for a full description of the fields surrounding the graphene. Importantly for experimental studies, these fields allow the transmission through the structure to be calculated as,

$$T = \left|\frac{\mathcal{P}_0}{\mathcal{Q}_{i,z}}\right|^2 \left(\frac{\epsilon_1}{\epsilon_2}\right)^{\frac{1}{2}}. \tag{2.34}$$

This description for the fields and the transmission allows the modal-matching model to be used to investigate the plasmonic behaviour of a single layer of graphene with alternating regions of high and low conductivity. The results of this investigation are presented in Chapter 3.

2.1.3 Finite Difference Time Domain Modelling

A well established tool for solving electromagnetic problems is finite difference time domain modelling (FDTD). The FDTD method is a computational approach of solving Maxwell's equations. In this thesis, the FDTD simulations are performed by commercial solver, "Lumerical FDTD Solutions", which adapts the method developed by Taflove [253] [254]. Initially, the FDTD method discretizes a region of interest into finite volumes, known as Yee cells, after their creator, as shown in Figure (2.3)[255]. The carefully offset components of the electric and magnetic field in each Yee cell are inserted into the differential form of Maxwell's equations and solved using a finite difference approach [256]. These fields are then stepped forward in discrete time steps, allowing the electromagnetic fields to propagate through the meshed region and around the objects of interest, see Figure (2.3) and Figure (2.4).

By necessity, the extent of the meshed region is finite, raising the problem of how to treat the edges of the simulation region. An important improvement for the FDTD method was describing the boundaries of simulation region as "perfectly matched layer" (PML), as shown schematically at the edge of Figure (2.4) [257]. The PML boundary is acts a reflectionless absorber for any electromagnetic fields allowing a source to be injected into a simulation region, interact with a sample of interest, and propagate away. Further computational advantages come from describing the remaining boundaries as periodic. These periodic boundaries allow an infinite array of graphene nanoribbons to be simulated with a $200\,\mathrm{nm}$ unit cell.

An important weakness of the FDTD method in modelling graphene nanostructures is the requirement imposed on the mesh size. In order to accurately model a layer of graphene, mesh cells with a dimension of $0.025\,\mathrm{nm}$ are required, perpendicular to the graphene. While Lumerical's graded meshing algorithm reduces the total number of mesh cells, as shown in Figure (2.4), a very large number, ~10^6, of mesh cells are still required. In order to keep the calculations stable, the Courant-Fredrichs-Lewy stability condition dictates that very small time steps are also required so the final simulation is computationally costly [258].

Despite this computational cost, an advantage of the FDTD method is the ease with which the frequency-dependant properties of a material can be implemented. The material data detailed by Palik allows realistic frequency behaviour of materials to be simulated [259]. The surface conductivity of a graphene layer is achieved by defining a very thin, but finite volume in the model, as shown in Figure (2.4), which is described by a frequency-dependent permittivity. This permittivity arises from considering how a layer of graphene interacts with an electromagnetic field [121],

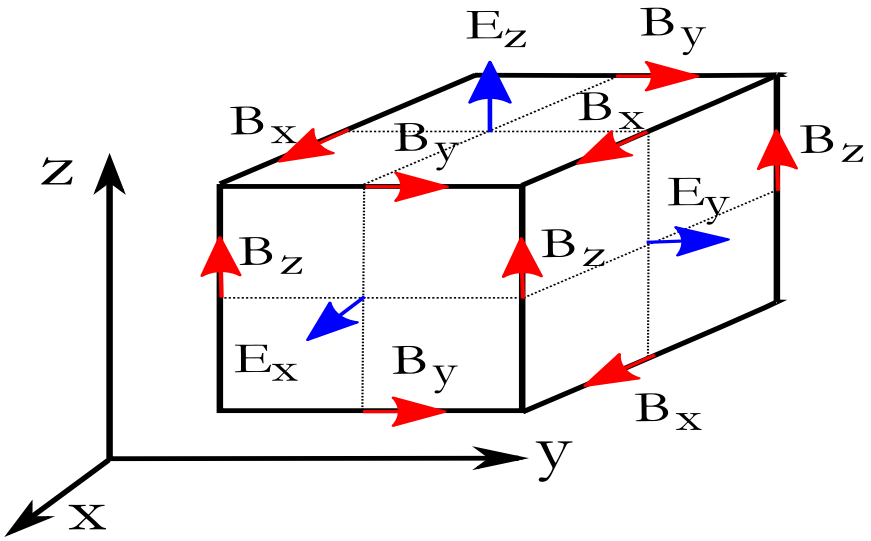

FIGURE 2.3: A schematic of a Yee Cell, demonstrating where the various electric and magnetic components of the fields are evaluated within a single mesh cell, (solid black lines). The FDTD model contains thousands mesh cells over the region of interest. This image has been adapted from Taflove and Hagness [254].

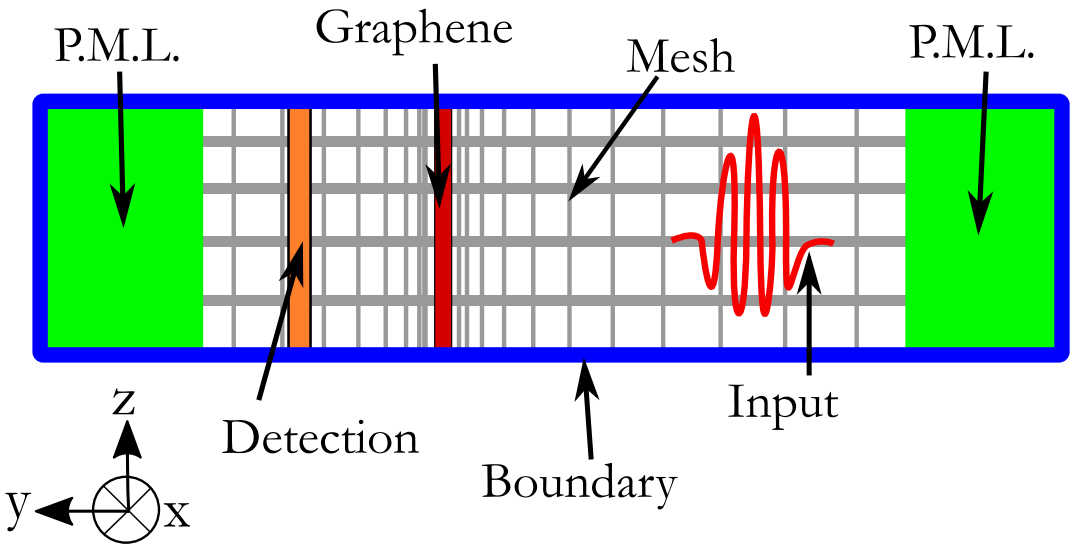

FIGURE 2.4: A schematic of the FDTD model geometry. The model consists of an air box (blue box), bounded by PML ends (green box) with a graded mesh (grey lines). The graphene (red box) is introduced as a thin cuboid, the excitation is a pulse of a fixed carrier frequency, modulated with a Gaussian envelope (red line). The transmission is calculated from a plane 2 μm away from the surface of the graphene (orange box).

$$\left(\frac{\partial}{\partial x} + k_g^2 + 2k_g \frac{2\pi i \sigma_g}{\epsilon_b \omega} \delta(x - \Lambda)\right) E_z = 0, \tag{2.35}$$

where z is in the plane of the graphene and x is perpendicular to the graphene layer, as shown in Figure (2.1) and k_g is the in-plane wavevector. The thickness of graphene is set to $\Lambda = 0.34\,\mathrm{nm}$ as determined by ellipsometry measurements [260] and $\epsilon_b = 2.5$ is the background permittivity [261]. The frequency dependant conductivity conductivity, σ_g, is described using the Kubo formula [114] as discussed in Chapter 1. In the long wavelength limit, $k_g \ll 1/\Lambda$, Equation (2.35) reduces to an effective bulk permittivity [113],

$$\epsilon(\omega) = \epsilon_b + \frac{i\sigma_g}{\Lambda \epsilon_0 \omega}. \tag{2.36}$$

As introduced in Chapter 1, patterning planar graphene into an array of ribbons allows free space light, polarised perpendicular to the ribbons, to excite a surface plasmon. As a demonstration of the FDTD model, the behaviour of an array of separated graphene ribbons, $100\,\mathrm{nm}$ wide in a $200\,\mathrm{nm}$ period, is investigated. The simulated transmission spectra through these ribbons at a range of Fermi levels, are shown in Figure (2.5a). The transmission spectra exhibit two characteristic features of graphene plasmons. First, the transmission spectra displays a transmission minima. The incident electric field causes the electrons with the graphene ribbon to oscillate collectively, screening the incident field leading to the observed transmission minima. Second, increasing the Fermi level of the graphene increases the frequency that this dip occurs at according to $\omega_p \propto \sqrt{E_f}$, in agreement with the results of Gao et al. [248] and is shown on Figure (2.5a). Increasing the Fermi level from $0.25\,\mathrm{eV}$ (red) to $0.4\,\mathrm{eV}$ (purple), increases the effective restoring force of the oscillation, increasing the resonant frequency from ~$22\,\mathrm{THz}$ to ~$28\,\mathrm{THz}$ as well as increasing the depth of the minima.

The nature of the FDTD method allows for the electric fields at the resonant frequency to be extracted directly. As is shown in Figure (2.5b), the electric field, surrounding the graphene (central black region) is strongly enhanced, relative to the incident electric field, and rapidly decays away from the graphene surface. Plotting the electric field as a function of the distance from the surface of graphene, at $y = 0\,\mathrm{nm}$, Figure (2.5c) shows the rapid decay in the electric field enhancement, on the order of $10\,\mathrm{nm}$, characteristic of a plasmon.

2.1.4 FDTD Modelling of Third Harmonic Generation from Graphene

An attractive feature of the FDTD method is the capacity to use ultrafast pulses as an excitation, which is more representative of the ultrafast pulses used in experiment. As introduced in Chapter 1, the very intense electric fields generated by ultrashort laser pulses,

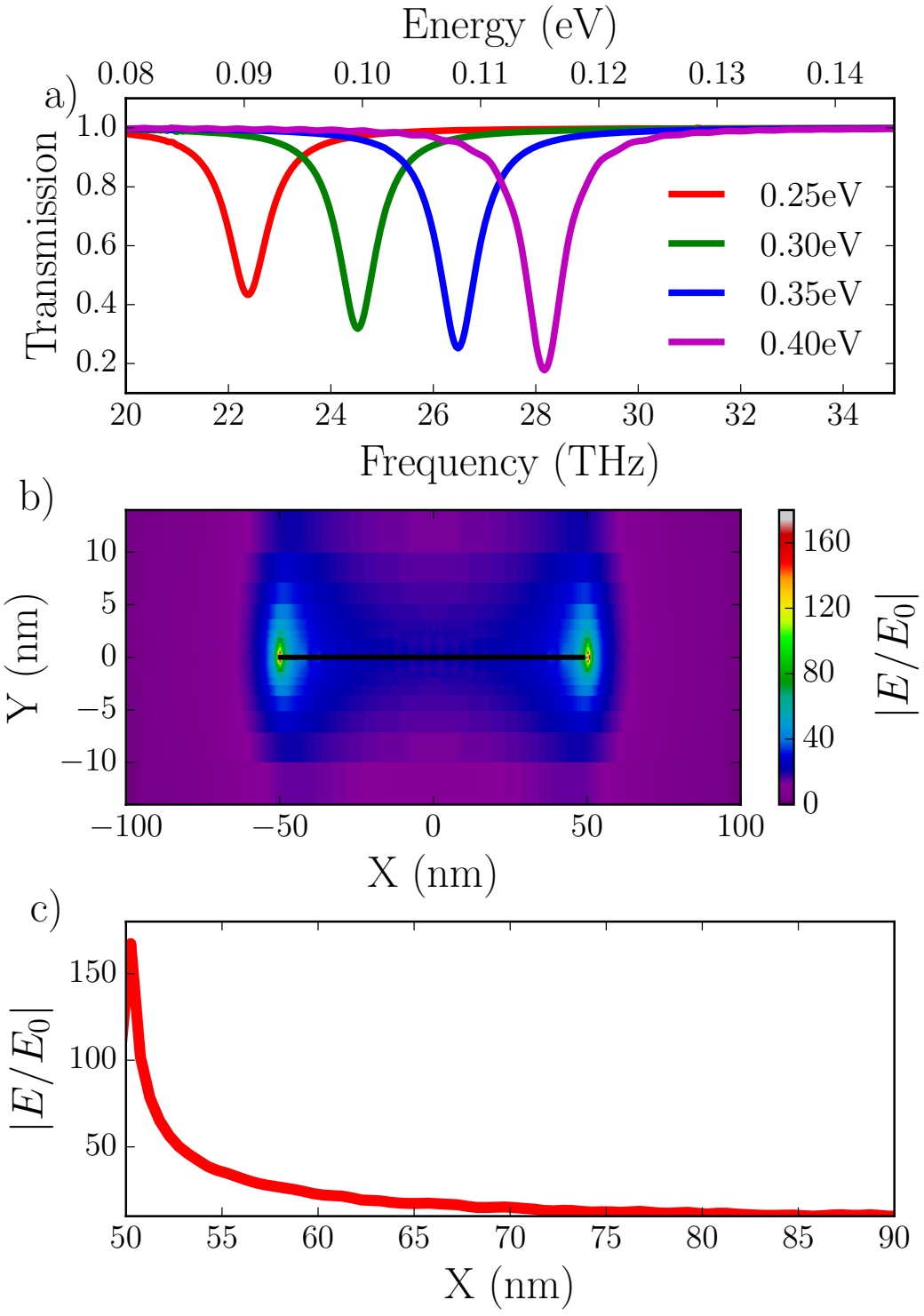

FIGURE 2.5: FDTD calculations for the electric field and transmission through an array of graphene nanoribbons. a) Plot of transmission through an array of graphene nanoribbons with increasing Fermi levels, as a function of wavelength and the equivalent energy scale. The plot shows the characteristic decrease in transmission at the resonant frequency and the increase in resonant frequency with Fermi level. b) The highly enhanced electric fields surrounding a graphene ribbon (black region). c) Exponential decay of the electric field from the edge of graphene ribbon, at $y = 0$ as taken from b).

the linear relationship between the electric field breaks down. To capture the nonlinear effects, the definition of the polarisation used when updating the electric and magnetic fields in the graphene layer in the model is extended to,

$$P(t) = \epsilon_0(\chi^{(1)}E(t) + \chi^{(3)}E(t)^3), \tag{2.37}$$

where $\chi^{(3)}$ describes the third order susceptibility of graphene. Note, that the centrosymmetric symmetry of graphene prevents second order processes from occurring, so $\chi^{(2)} = 0$ [170].

The FDTD model provides a tool for characterising the behaviour of the stacked structure, proposed by Savostianova and Mikhailov to enhance the third harmonic generation from graphene [196]. Following the same meshing procedure as for the nanoribbon models, shown in Figure (2.5), the wavelength dependent reflection of the cavity is calculated from a broadband pulse and by integrating the power derived from the Poynting vector, through a plane, parallel to the graphene layer. The nature of the FDTD method also allows the fields inside the cavity for different wavelengths to be determined.

For determining the third-order enhancement, the experimental conditions were matched as close as possible. A pulse of a fixed carrier frequency, modulated with a Gaussian envelope was applied to the graphene layer. Due to the implementation of the boundary conditions, the simulations were performed with pulses at normal incidence. This pulse has a full width half maximum (FWHM) of $100\,\mathrm{fs}$, and a peak electric field amplitude of $2.3 \times 10^8\,\mathrm{Vm}^{-1}$ corresponding to an average power of $6.5\,\mathrm{mW}$. The central wavelength is varied in the range of $1630\,\mathrm{nm}$ to $2400\,\mathrm{nm}$. At each input wavelength, the average power of third harmonic power generated is determined by integrating the power derived from the Poynting vector across a parallel plane placed $2\,\mu\mathrm{m}$ away from the graphene. The results of the modelling and corresponding experimental results are presented in Chapter 4.

2.2 Sample Fabrication Methods

With these analytical tools in place, this section details the methods used to fabricate the desired sample. The fabrication of the stacked structure, presented in Chapter 4, required multiple steps; thermal evaporation, sputter coating and finally, wet chemical transfer of chemical vapour deposition (CVD) graphene. To fabricate the sample required for the photoluminescence experiments, presented in Chapter 5, optical lithography is combined with thermal evaporation of aluminium before the wet chemical transfer of a layer of CVD graphene.

2.2.1 Lithography and Thermal Evaporation

A widely used method for creating bespoke patterns in thin films of metal is to combine lithography with thermal evaporation of metals, which is more commonly used to create small scale electrical contacts to graphene [262][263][57][245]. The lithography in this thesis is performed with a positive photoresist, S1813, which is dropcast onto the sample and spin-coated at $4000\,\mathrm{rpm}$ to achieve a layer of ~2 $\mu\mathrm{m}$ thick. The sample is then treated with a prebake stage on a hotplate set to 120° C for 60 seconds, as shown in Figure (2.6a) [264]. A Durham Magneto-Optics MicroWriter ML2, using a $405\,\mathrm{nm}$ CW laser, exposes areas of the sample according to an automated pattern. The sample is then placed in MF319, as a developer, for 17 seconds, dissolving the exposed regions before washing in deionised water for 60 seconds, in preparation for thermal evaporation as shown in Figure (2.6b).

All thermal evaporation processes presented in this thesis are performed with a HHV Auto306 thermal evaporator. This system is comprised of a vacuum chamber containing a sample mount and a selection of metals. Once the sample is inside the chamber and a pressure of ~$1 \times 10^{-6}\,\mathrm{Torr}$ is achieved, a current is passed through the desired metal. The current heats the metal causing it to evaporate onto the sample in areas defined exposed by the pattern in the photoresist, as shown in Figure (2.6c). The thickness of the deposited layer can be controlled with sub nanometre precision, essential for the requirements of the stacked structure for Chapter 4. Once the desired thickness has been deposited the sample is removed from the thermal evaporator and placed in warm acetone, at a temperature of ~40° C, to remove the undesired photoresist. Finally the sample is then placed in IPA to remove residual acetone and blown dry with N_2.

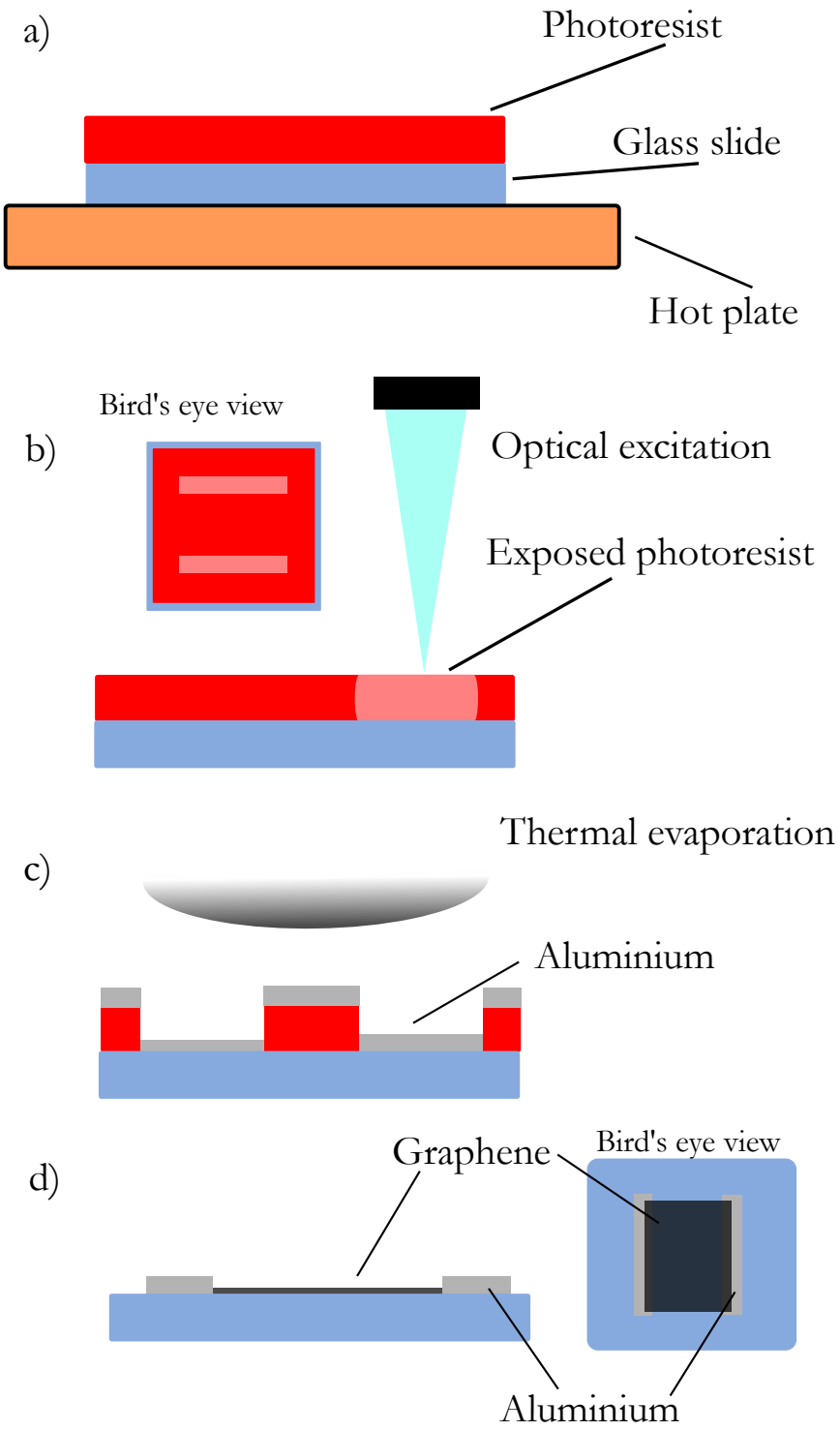

FIGURE 2.6: Schematic diagram of sample fabrication process showing photolithography and thermal evaporation. a) Schematic of the sample at the prebake stage with a 2 µm layer of the photoresist, S1813 spun-coated on top. b) Schematic diagram of the selective optical exposure of the photoresist in the MicroWriter ML2, with a bird's eye view of the final pattern. c) Schematic diagram of thermal evaporation of metal, with metal being deposited onto the sample exposed regions. d) View of the final device, with the aluminium markers and graphene transfered.

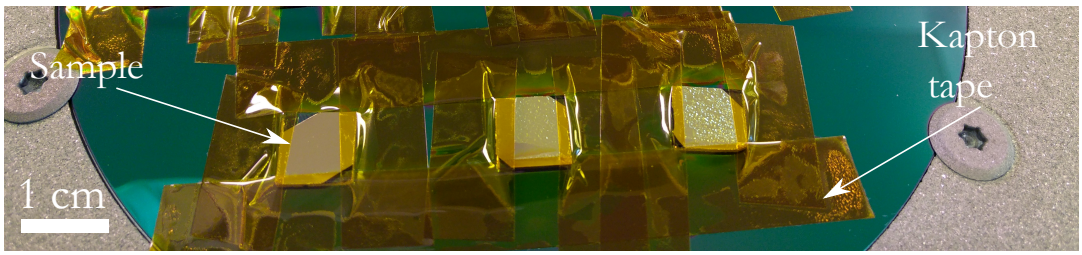

FIGURE 2.7: Photograph of gold/glass substrates after SiO_2 deposition, secured down by Kapton tape. The scale bar is 1 cm.

2.2.2 Sputter Coating

The fabrication of the stacked structure, used in Chapter 4 to investigate the nonlinear properties of graphene requires several steps, guided by FDTD modelling. The fabrication of the cavity starts by thermally evaporating a 5 nm layer of chrome onto a glass coverslip to provide an adhesive layer for thermal evaporation of a 150 nm layer of gold. The samples are then cleaned in acetone, IPA and water and dried. Before the silicon dioxide deposition, the sample is exposed to an argon etch of 1 minute at a pressure of 30 mTorr and at 30 W RF power to remove possible contaminants. A second, 5 nm layer of titanium, adhesion layer is then sputter-coated at a pressure of 2 mTorr and at 300 W DC power. From initial attempts the titanium adhesion layer was vital for achieving good adhesion for the sputtered SiO_2. However, the adhesion layer reduces the magnitude of the resonant enhancement of the cavity, as will be shown in Chapter 4, Figure (4.1). The final step of the fabrication is sputter-coating, a SiO_2 layer from a SiO_2 target, with a 2:1 Ar to O_2 gas ratio, at 2 mTorr and at 150 W RF power, using an AJA Orion sputter coater. The sample, secured to the base of the sputter coater with Kapton tape, after this sputter coating procedure is shown in Figure (2.7), showing the importance of thorough cleaning with the right hand sample showing signs of the SiO_2 layer not fulling adhering to the substrate. Using ellipsometric measurements, the thicknesses of the titanium and SiO_2 layers were confirmed to be 8 nm and 309 nm, respectively. A 1 cm^2 x 1cm area CVD graphene, sourced from graphene--supermarket.com, is then transferred onto the sample using a PMMA assisted transfer technique.

2.2.3 Wet Chemical Transfer of Graphene

The initial demonstration of the range of physical phenomena unique to graphene generated huge scientific interest. As mentioned in the introduction, fabricating such graphene flake samples is a laborious process and yields small, ~10 μm^2, flakes of graphene [57]. The desire to create larger area graphene devices has driven research into methods of synthesising

graphene [265][266]. The two competing factors in producing graphene are the cost of production and the quality of the graphene produced. CVD-grown graphene produces reasonable quality, displaying mobilities ~$4 \times 10^3\ \mathrm{cm^2 V^{-1} s^{-1}}$ [267] [268], and has been demonstrated as a method for synthesising graphene over huge areas [93]. The graphene used in this thesis is CVD-grown graphene and was sourced from graphene-supermarket-.com. This allows large areas, ~$1\ \mathrm{cm^2}$ of the substrate to be covered in graphene, allowing easier integration with optical experiments. The CVD method of growing graphene uses a copper foil as a seed layer, which requires a wet chemical treatment to remove [93] [269]. A schematic of this wet transfer technique is shown in Figure (2.8). Initially, a ~$300\ \mathrm{nm}$ layer of PMMA is spin-coated on top of a layer of graphene to form a protective and supportive layer, as shown in Figure (2.8a), the underlying graphene layer is removed through plasma etching. The exposed copper is floated in a solution of $1.3\ \mathrm{mg}$ of ammonium persulfate (APS) in $50\ \mathrm{mL}$ of deionised water as a chemical etchant and left overnight as shown in Figure (2.8b). After this etching process the PMMA-graphene structure is floated in fresh DI water to remove residual APS. The PMMA-graphene structure is transfered to the substrate and left to dry in air overnight. Finally, the PMMA layer is removed in acetone and the sample is washed with IPA and dried with N_2.

2.3 Measurement Techniques

2.3.1 Raman Spectroscopy

Characterising and improving the process of synthesising graphene requires a powerful characterisation tool. One such technique is atomic force microscope (AFM) measurements which can give detailed information about the number of layers present in a sample but at a severe time cost [77][270]. A subtle optical contrast effect makes monolayer graphene, which is deposited on a silicon substrate with a $300\ \mathrm{nm}$ oxide layer, visible in an conventional microscope Blake2007 However, this optical contrast technique requires experience to make it effective and lacks the ability to extract chemical information about the graphene.

Raman spectroscopy has been used for many years as a noninvasive characterisation technique for carbon based materials, from graphite, carbon nanotubes [271], and nanodiamonds [272], to provide rich information about the sample. Raman spectroscopy uses laser light, as a source of photons with a well defined energy, to excite lattice vibrations in a graphene layer. Exciting these lattice vibrations is an inelastic process, which leads to a characteristic decrease in the energy of the re-emitted photon, known as the Stokes shift [68]. Note, while an increase in the energy of the re-emitted photons is possible, this anti-Stokes process is much weaker [213]. The types of modes that graphene can support is

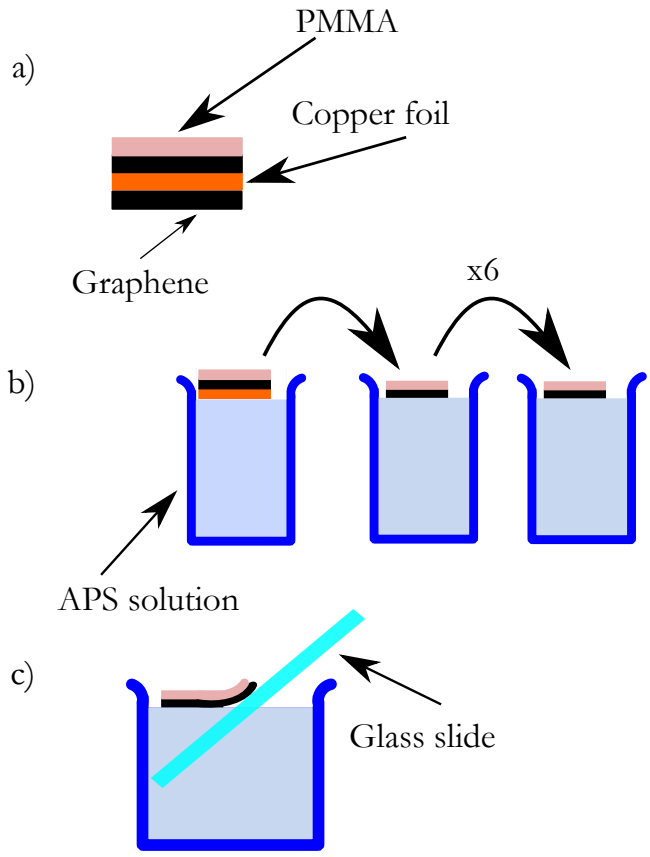

FIGURE 2.8: Schematic diagram of the wet chemical graphene transfer technique. a) Copper foil with graphene grown on both sides. The top side has a ~300 nm protective PMMA layer spun coated on top, the exposed underside is removed with reactive ion etching. b) Chemical etching in a solution of APS and DI water followed by floating the PMMA-graphene structure in multiple beakers of DI water to remove residual APS. c) CVD transfer onto the glass slide.

governed by symmetry-based selection rules [273][213] and results in the Raman spectrum for graphene containing three characteristic peaks.

These characteristic peaks are the D peak, G peak and 2D peak, as shown in Figure (2.9). All Raman spectra in this thesis were obtained, in air and at ambient temperatures, with a Horiba Xplora Raman system using a 532 nm excitation laser and a 100x objective lens and a 2400 $\mathrm{l(mm)^{-1}}$ grating with a movable stage. By recording spectra at multiple positions of the stage, area maps of a graphene sample could be obtained. The important features in this spectrum are labelled; the D peak, centred at 1350 $\mathrm{cm^{-1}}$; G peak centred at 1583 $\mathrm{cm^{-1}}$ and the 2D peak, centred at 2693 $\mathrm{cm^{-1}}$. The G peak arises from a first order process exciting the LO phonon mode [276]; the motion of the carbon atoms of this LO mode is shown in the inset Figure (2.9a) [112]. The origin of the 2D peak arises from a peculiarity in the band structure of graphene which means phonons from the K and K' points can have exactly

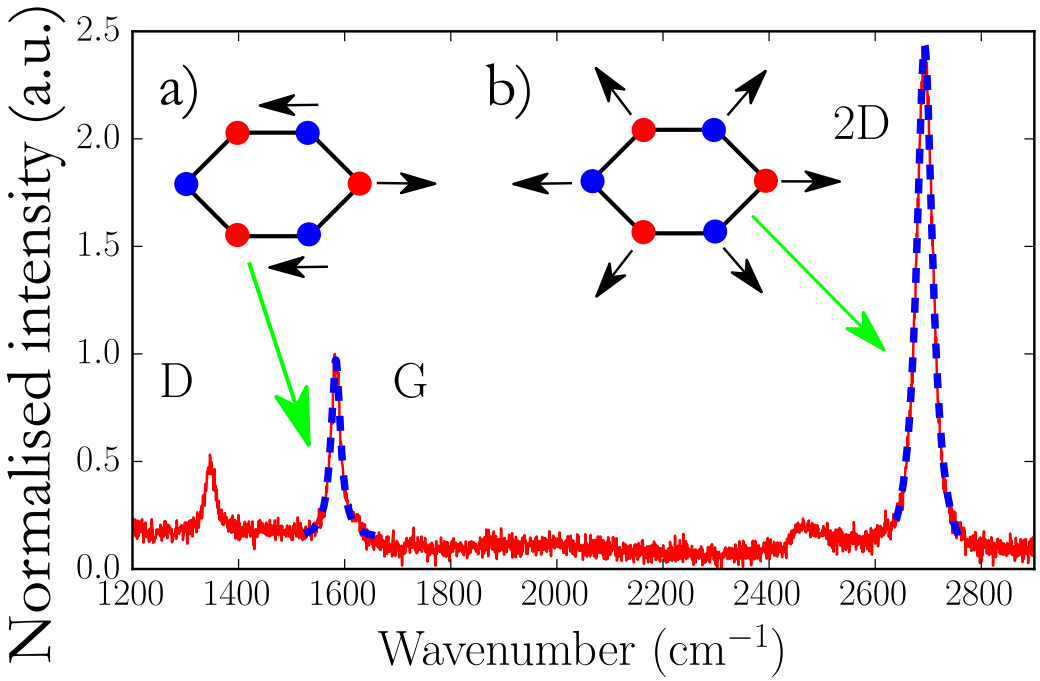

FIGURE 2.9: A typical Raman spectrum of CVD grown graphene sample, deposited on a glass substrate and normalised to the G peak intensity. Peaks of particular interest have been labelled, (blue line is a Gaussian fit) and labelled; D peak, centred at 1350 cm^{-1}; G peak centred at 1583 cm^{-1}; and the 2D peak centred at 2693 cm^{-1}. The symmetric shape of the 2D peak and the ratio of 2.4 in the intensity between the 2D/G peak is indicative of single layer graphene [274][275].

compensating wavevector and take part in a second order scattering process [276]. The intensity of this second order scattering process can be commensurate with the intensity first order process behind the G peak because it is resonant [68]. The D peak arises from the presence of a defect in the lattice which provides the required wavevector matching requirements [112]. The motion of the atoms behind the breathing mode of the 2D peak is shown in the inset Figure (2.9b). Analysis of these characteristic Raman peaks allows detailed chemical information about a graphene sample to extracted. For example, the symmetric shape of the 2D peak and a ratio of 2.4 in the intensity between the 2D:G peak is indicative of single layer graphene [274][275]. The D peak is typically present in CVD graphene, and the relative peak intensities of the G:D peak gives information about the density of defects in the sample [277]. As mentioned in Chapter 1, the D peak is usually absent for the highly crystalline flake samples [77].

Additionally, the positions of the G and 2D peak are both related to the Fermi level and strain [262], as the photon-electron interaction is mediated by electronic states [278]. Creating strain within a graphene layer changes the interatomic distances between the

carbon atoms. As can be imagined from the inset Figure (2.9a, b), the changes in the carbon-carbon bond lengths changes the frequency of the phonon modes and therefore the Raman spectrum. Compression (tension) causes the Raman modes to stiffen (soften), increasing (decreasing) the frequency at which they occur [129].

This dual dependence of the G and 2D peak positions on both Fermi level and strain requires careful analysis to isolate the separate contributions. Before Raman spectra from graphene samples were taken, the Horiba system was carefully calibrated. The first calibration was to the TO phonon mode in silicon at $520\,\mathrm{cm}^{-1}$. The second calibration was to the spectrum of paracetamol [279] [280]. As shown in Figure (2.10), the spectrum of paracetamol has multiple, peaks, which occur at well known frequencies. These peaks occur across approximately the same frequency range as the graphene spectrum, making it a suitable calibration sample. Once these calibration measurements were performed Raman measurements of graphene samples were taken.

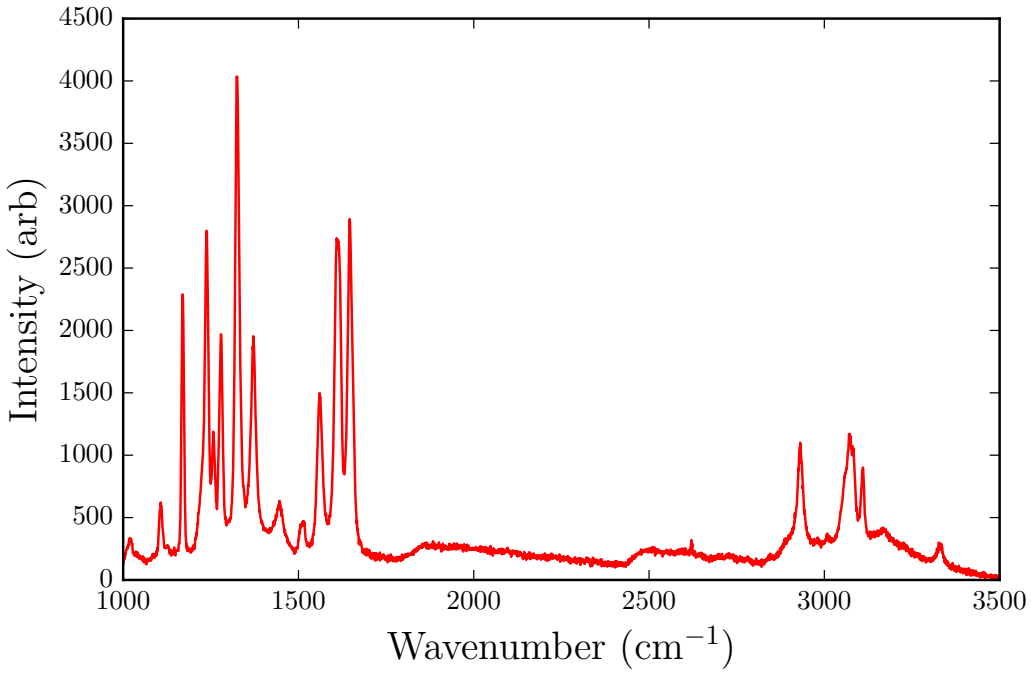

FIGURE 2.10: Example of a typical Raman measurement of a reference paracetamol sample, providing a calibration spectra. Note the frequency range from $1200\,\mathrm{cm}^{-1}$ to $3000\,\mathrm{cm}^{-1}$ is similar to the spectral frequency range of interest for the graphene measurements.

Fortunately, the changes in the strain and Fermi level cause different changes to the position of the G and 2D peak. These contributions can be separated by performing a vector decomposition as outlined by Lee et al. [129]. The vectors used for the vector decomposition are constructed by comparing the peak positions of unstrained and undoped graphene, as

shown with the green star in Figure (2.11) [281], with an example experimental position marked by the red circle, in Figure (2.11). The gradients of the vectors, $\Delta\omega_{2D}/\Delta\omega_G$, are shown by the blue and red line in Figure (2.11), and are dependent on the type of strain as well as the nature of Fermi level shift, either hole or electron doped.

For biaxial strain, $\Delta\omega_{2D}/\Delta\omega_G$ has been measured to be in the range of 2.45 to 2.8[282] [283][284]. For uniaxial strain, the value of $\Delta\omega_{2D}/\Delta\omega_G$ is sensitive to the direction of the strain relative to the crystal axis of the graphene, i.e. relative to the arm-chair or zig-zag direction [285]. For sufficiently large strain, ~0.74%, the G peak splits into two distinct modes, a G^+ and G^- peak [278]. However, for small strains, the mean of the G^+ and G^- behaviour, $\Delta\omega_{2D}/\Delta\omega_G = 2.2$, gives a good agreement to the measurements of Lee et al. [129] [278]. The change in the G position has been measured to correspond to a linear change in the percentage strain proportional to, $-23.5\,\mathrm{cm}^{-1}/\%$ [278][286].

The behaviour of the G and 2D peak changes for electron or hole doping. The the samples used are assumed to be hole-doped since the PMMA assisted transfer process [287] and atmospheric moisture [288] are known to hole-dope graphene devices. Typical CVD transferred samples display hole doping [127] [289]. For small Fermi levels, $E_f < 1\,\mathrm{meV}$, the divergent behaviour of the electron density in graphene means the position of the G peak cannot be uniquely identified within the vector decomposition [290][291][292]. However due to the slight hole-doping from the PMMA transfer technique, this effect can be ignored. As a result, the vector associated with doping, the red line in Figure (2.11), is $\Delta\omega_{2D}/\Delta\omega_G = 0.7$ [129]. From the measurements of Das et al. the G peak position changes with Fermi level as; $1.02\,\mathrm{cm}^{-1}$ per $1 \times 10^{12}\,\mathrm{cm}^{-2}$ [262].

2.3.2 Luminescence Measurements

As introduced in Chapter 1, the luminescence intensity emitted from a molecules in close proximity to a graphene layer is strongly reduced, or quenched, relative to molecules in free space. The quenching effect can be used for microscopy applications to investigate small length scales from the fluorescent molecule and for complicated combinations of multiple fluorescent emitters [293]. For graphene, this quenching effect has been shown by Guo et al. to be proportional to defect density of graphene samples [294]. By systematically plasma ashing the sample and characterising the sample with Raman spectroscopy measurements Guo et al. demonstrated a significant reduction in the quenching factor with increasing defect density. The results of a similar method are presented in Chapter 5; where a spatial strain profile is investigated by combining Raman spectroscopy and luminescence measurements. By exploiting the interaction between CVD graphene and luminescent molecules the strain profile can be mapped over large areas. The fabrication of the required sample starts with a

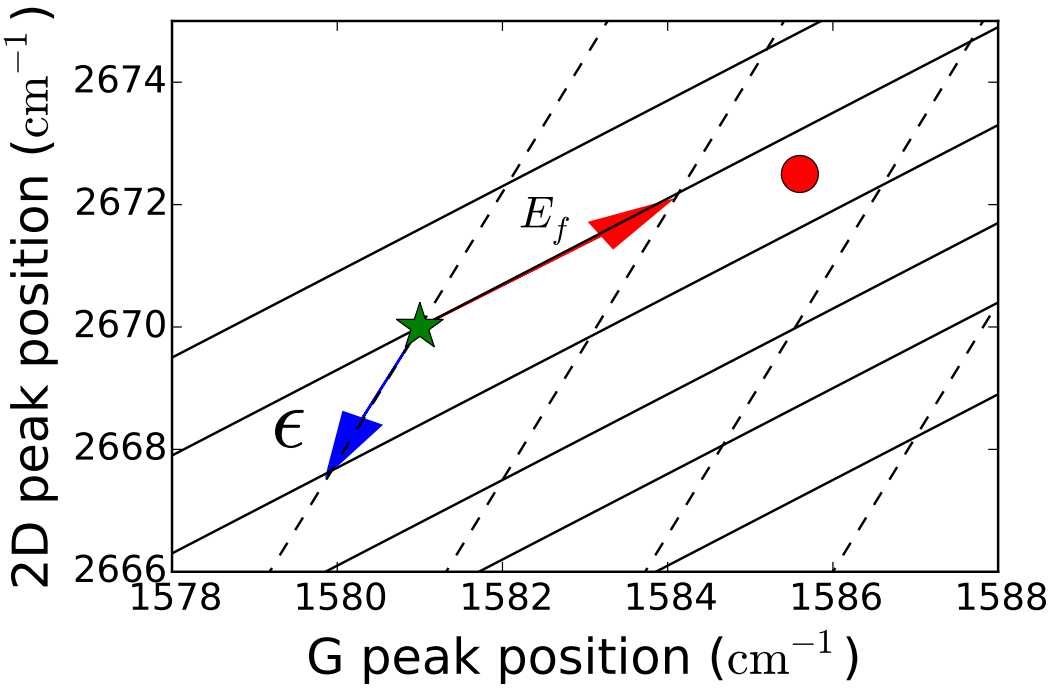

FIGURE 2.11: A plot of the vector contributions to an example position of the G peak and 2D peak, (red circle), relative to unstrained and undoped graphene (green star), (1581 cm^{-1}, 2670 cm^{-1}) [281]. This plot has been adapted from [129]. The red vector showing the contribution from changes in Fermi level, the blue vector showing the contribution from strain induced tension. The black lines are a guide to the eye to indicate the contributions from strain (dashed) and doping (solid) to an experimental position (red circle).

glass coverslip, ~140 $\mu\mathrm{m}$ thick, as an optically transparent support substrate. Following the fabrication procedure outlined be earlier in this chapter, 30 nm tall aluminium markers, are deposited onto the glass substrate to provide a reference point between the Raman and luminescence mapping. Subsequently, a ~1 cm^2, area of CVD graphene is transfered on top. A fluorescent molecule is dissolved in methanol and dropcast onto the graphene. The fluorescent molecule is rhodamine-6G [295] conjugated with pyrene, as a binding molecule [296][297], as shown in Figure (2.12a). Noncovalently bound pyrene molecules have previously been used to protect biosensing molecules on graphene [298] [299]. The pi-pi bonding of the pyrene to graphene could potentially allow the luminescent molecule to be removed [300][301].

Rhodamine is chosen as the fluorescent molecule as it has well characterised absorption and emission spectrum [302][303] and even at monolayer concentrations the emitted fluorescence is still detectable with the PMT R:9624 used in the confocal microscope [304][305]. The rhodamine-pyrene (RP) molecule is dissolved in methanol and dropcast

on top of graphene. Since the methanol wets the surface of the graphene very well a 1 µL volume of RP solution results in a drop with a radius of ~1.5×10^{-3} m. With this volume of methanol and noting the diameter and molecular weight [306], the required mass of PR molecule for a monolayer is 60 µg using a volume of 30 mL of methanol.

The luminescence measurements were taken using a Leica TCS SP5 confocal microscope, as shown schematically in Figure (2.12b), and were measured at a 10 Hz refresh rate in air at ambient temperatures. An acousto-optical tunable filter (ATOF) is used to select an excitation wavelength of 514 nm, chosen from absorption spectrum of rhodamine [303]. The incident light is then focused onto the sample through an 63x oil immersion lens. The use of scanning mirrors allow the focused spot to be rastered over the sample. The field of view of the microscope allows 250 μm^2 images to be taken. The emitted luminescence is collected back through the lens and directed through a pinhole using an acousto optical beam splitter (AOBS) to select wavelengths between $550 - 680$nm as selected from by the emission spectrum of rhodamine [302]. As shown in Figure (2.12) The pinhole, kept at 1 Airy radius, spatially filters the emitted light allowing light from the focal plane, α (green), to enter the detector, rejecting the rest of the light β (red). The light is then directed onto a PMT and synchronised with the scanning mirrors to build an image.

In addition the ubiquitous technique of controlling the Fermi level with an external voltage, as introduced in Chapter 1, strain engineering gives an extra route for dynamically manipulating the properties of a graphene layer with the potential for use in highly sensitive strain detectors. This reversible control has been demonstrated by transferring graphene onto piezoelectric substrates [283][284], flexible substrates [307] and exploiting the mismatch between the thermal expansion of graphene and the underlying substrate [308]. The reversibility of an applied strain profile was demonstrated by Elibol et al. by inducing a strain profile in micron-scale graphene flakes with an AFM tip [309].

These studies highlight the importance of understanding the strain in a graphene sample. While Raman spectroscopy is a powerful tool, producing high-resolution maps is time-intensive and requires careful post-processing. Fluorescence imaging provides a faster alternative. In Chapter 5 the results of these luminescence measurements are compared to the vector decomposition analysis from Raman spectroscopy maps of strained graphene samples.

2.3.3 Nonlinear Measurement

To experientially investigate the nonlinear properties of graphene, large electric fields, $1 \times 10^8\,\mathrm{Vm}^{-1}$ are required. These intense electric fields are achieved with high energy, pulsed laser light. The schematic of the two-pulse correlation measurement used to measure

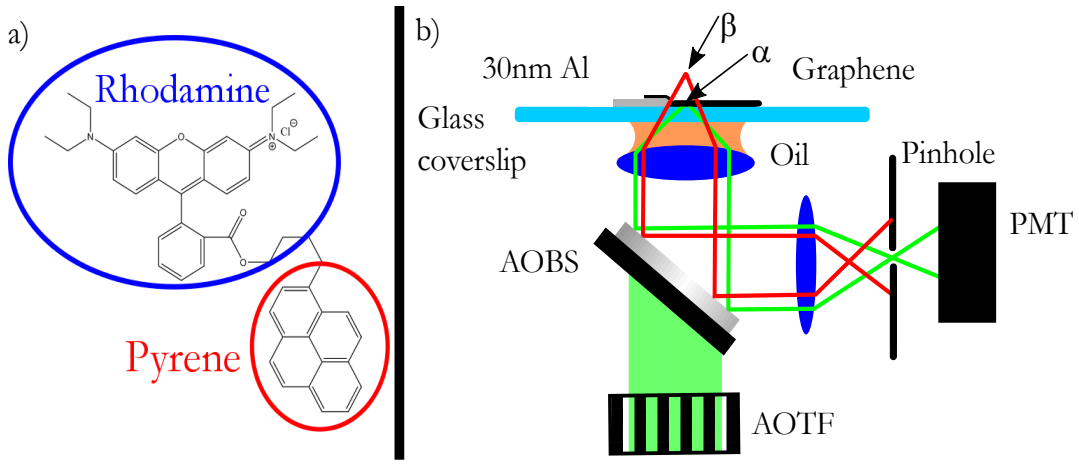

FIGURE 2.12: a) Molecular diagram of the pyrene-rhodamine molecule. b) Schematic of the confocal microscope used to acquire the luminescence images. An AOTF is used to select a precise wavelength of excitation which is focused onto the sample using an oil immersion lens. The use of a pinhole, selects light exclusively from the image plane,α, onto the PMT and rejects light from out of focus planes β.

the third harmonic generation from graphene is shown in Figure (2.13a). The high energy pulses are generated by the use of a regenerative amplifier (Coherent Legend Elite) with a 800 nm seed laser (Coherent Vitesse) with 85 fs pulses and a 532 nm pump (Verdi). These pulses are then stretched in time, lowering the instantaneous power to avoid damaging the gain medium of the cavity. After multiple passes through the cavity, a polarisation change switches the pulses out of the cavity where they are re-compressed to approximately 100 fs. The pulses leave the amplifier with an energy of 3 mJ per pulse. When these amplified pulses enter the TOPAS-C they are immediately directed to a beamsplitter, creating an 800 nm pump beam, with ~80%-90% of the incident power, and an 800 nm seed beam. The seed beam is passed through two Brewster angled plates in order to control the time delay between the pump and the seed beam. This seed beam is used to generate a white light continuum and focused onto a nonlinear crystal where the seed beam is pre-amplified by the pump beam. The angle of this crystal is controlled from a computer which controls the wavelength output from the TOPAS-C. Since the generated signal beam from the nonlinear crystal is spatially separated from the pump beam, the signal beam is easy to direct through collimation optics and towards a second nonlinear crystal. At the second nonlinear crystal the signal beam is parametrically amplified with the pump beam. The resulting signal and idler frequencies are then directed out of the TOPAS-C and into an external frequency mixer, to generate the wavelength range required for this thesis. Once the desired wavelength has been generated, the beam is directed towards a beam splitter to create two beam paths, both with comparable fluences. One beam path has a motorised

delay stage to control the arrival time between the pulses at the sample. The beams are then weakly focused onto the sample and carefully spatially overlapped.

2.3.4 Optimisation of the Spatial and Temporal Overlap

Initially, a barium borate (BBO) nonlinear crystal was used to achieve the required temporal and spatial overlap the two incident pulses. The BBO crystal generates a second harmonic beam from the incident pulses in the visible range. This second harmonic beam was directed onto a photodiode as shown in Figure (2.14c). By adjusting the alignment of the incident beams the signal from the photodiode was maximised to optimise the spatial overlap of the incident beams. The graphene-cavity sample was then placed at this spatial overlap position with an xyz micrometer stage. To confirm the position of the temporal overlap, a differential reflection measurement was performed. One of the incident beams is then modulated at $525\,\mathrm{Hz}$ via a mechanical chopper, and the unmodulated beam is directed to a photodiode which is connected to a lock-in amplifier. A motorised delay stage is used to adjust the relative path length between these beams and the voltage from the lock-in amplifier is recorded. A typical time-delay scan is given in Figure (2.15), showing the reflected intensity decreasing, indicating the time delay where pulses are temporally overlapped. This decrease in intensity arises from the energy in the overlapped pulses being used to generate nonlinear harmonics, as introduced in Chapter 1, reducing the intensity of the measured beam. This optimisation procedure limits the incident angle of the pulses to $\phi_2 = 8°$, $\phi_1 = 30°$ as shown in Figure (2.13b). Additionally, the non collinear incident beams highlight a degeneracy within the third harmonic generation process. As a result, third harmonic light is generated at four angles, allowing for simple spatial filtering of the third harmonic signal. The third harmonic photons generated in R_1 and R_2 are a result of three photons coming from the respective incident beams. The photons generated in R_3, the detected beam, come from combining two photons from I_1 with a single photon from I_2. The photons from in R_4 come from combining two photons from I_2 and one photon from I_1.

Recording the voltage from the lock-in amplifier brings up the question of converting the voltage to a more comparable quantity such as Watts. The procedure for this conversion is shown schematically in Figure (2.14). The conversion aims to measure the output power of the TOPAS-C with a thermal power meter, Figure (2.14b) and compare this to the value recorded by the APD and lock-in amplifier. A wavelength of $650\,\mathrm{nm}$ from the TOPAS-C was selected because as it inside the detection range of both the APD and the thermal power meter and close to the resonant third harmonic wavelength. These measurements allow the recorded lock-in voltage to be converted to an average power.

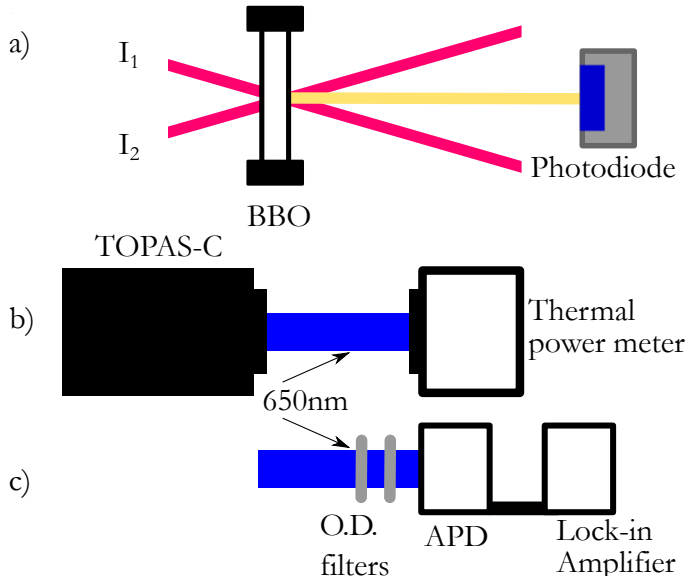

FIGURE 2.14: a) Schematic for optimising spatial overlap. The input beams, I_1 and I_2 are from Figure (2.13) and the second harmonic, R, is generated by the BBO and directed towards a photodiode. b,c) Schematic of the calibration procedure, setting the output of the TOPAS-C to 650 nm and consecutively measuring the beam with b) a thermal power meter and c) a APD and lock-in amplifier. Note the optical density filter used to reduce the average power below the damage threshold of the APD.

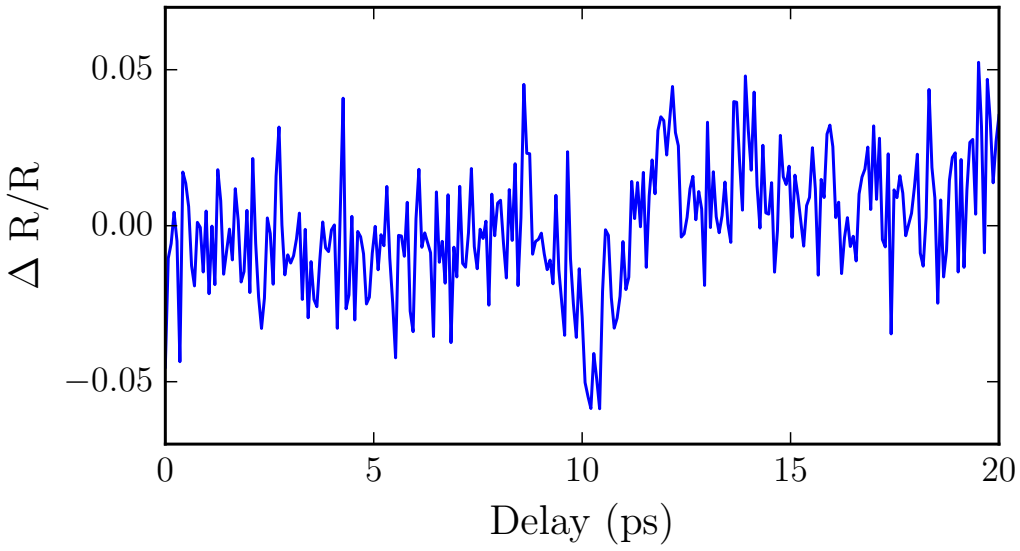

FIGURE 2.15: Typical differential reflection time-delay scan measurement with the photodiode. Note the central dip at ~10 ps, indicative of the temporal overlap of the two pulses.

With this temporal and spatial overlap, the avalanche photodiode detector (APD) was placed at the calculated angle of $\phi_3 = 15°$ and the incident beams were spectrally filtered using a silicon wafer which is transmitting for wavelengths $> 1130\,\mathrm{nm}$) to remove any optical contamination in the beams. The fluence of the pulses is kept below $1\,\mathrm{mJ\ cm^{-2}}$, well below the photo-modification threshold for graphene [130]. The FWHM of the spot was measured to be ~$800\ \mu\mathrm{m}$ using a CCD camera beam profiler. By measuring the average power with a thermal power meter, the fluence of the pulses is kept below $1\,\mathrm{mJcm^{-2}}$, well below the photomodification threshold for graphene [130]. The thermal power meter is also used to measure the reflection of the incident pulse to continuously monitor the average incident power, which is typically ~$6\,\mathrm{mW}$. The temporal overlap of these two beams, Δt, at the sample interface is controlled by a motorised delay stage, which changes the path length for one pulse and therefore the arrival time. To measure the third harmonic signal, an avalanche photodiode (APD), protected by an $800\,\mathrm{nm}$ short pass filter, is connected to a lock-in amplifier. One of the incident beams is then modulated at $525\,\mathrm{Hz}$ via a mechanical chopper, and the voltage from the lock-in amplifier, is recorded. Through characterising the detector with a known average power, this voltage can be converted into an average power. The sample is mounted on an xyz micrometer stage so that areas of the sample covered with graphene can be easily compared to areas free from graphene. The results of the two pulse correlation measurements are presented in Chapter 4.

This chapter detailed the techniques used to investigate the phenomena of interest to this thesis. Starting with the FDTD and modal-matching models before detailing the fabrication methodology for the wet-chemical transfer of graphene and thermal evaporation and sputter coating needed for the cavity device presented in Chapter 4. Finally the experimental techniques for measuring the third harmonic generation and the luminescence intensity were presented. The following chapters present the results using these techniques starting with modelling of nanostructured graphene.

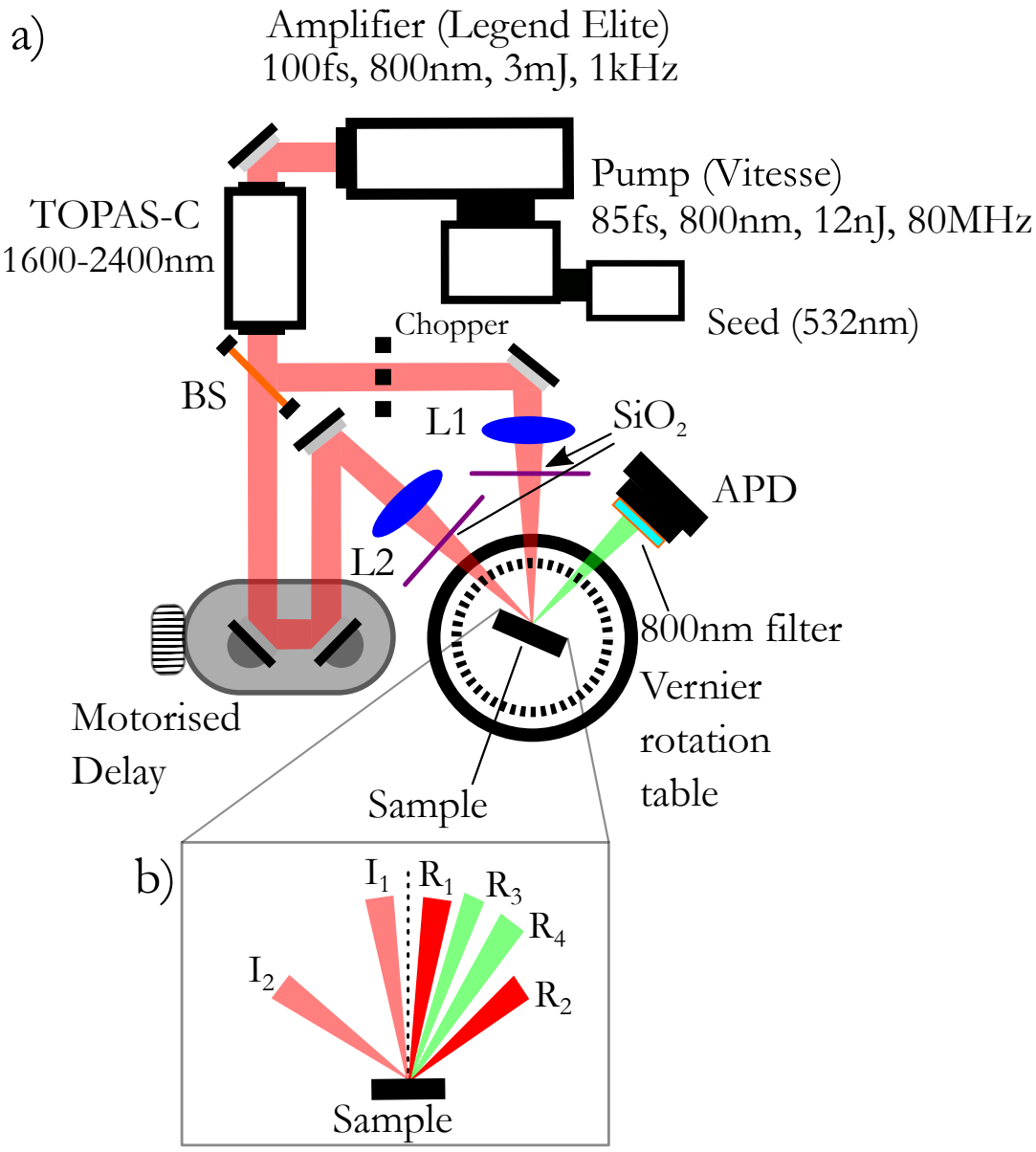

FIGURE 2.13: a) A schematic showing the experimental set up for the third harmonic generation experiments. The ultrafast pulses generated are by the Legend Elite and the desired wavelengths generated by the the TOPAS-C. This beam is directed towards a beam splitter (BS), one beam is modulated by the mechanical chopper and focused by a lens (L1) onto the sample, the other is directed towards a motorised delay stage and focused by a lens (L2) onto the sample. The beams are spectrally filtered by a 100 µm SiO_2 wafer. The APD is mounted, protected by an short pass 800nm filter (FES800), on a Vernier rotation stage to allow for fine control of the sample orientation. b) A detailed schematic showing the incident and outcoming beams from the sample. The incident beams from a), measured from the surface normal, (dashed black line) are I_1=8°, I_2=30° and their reflections, R_1 and R_2. A third harmonic signal is generated at R_3=15°, the detected beam, and R_4=22°.

Chapter 3

Modulated Graphene Conductivity

As has been introduced in previous chapters, graphene has been the focus of intense study since being identified [57]. While initial research was driven by its novel electronic properties [107], the electromagnetic properties of graphene are of increasing interest. This chapter focuses on the ability of graphene to support surface plasmons at infrared frequencies [131]. The infrared frequency regime holds a broad range of potential infrared applications, so the promise of being able to control plasmons in graphene is also of technological interest [135], [136]. Moreover, the deeply subwavelength confinement of surface plasmons in graphene and the associated high field enhancement could be of potential benefit for nanophotonic and sensing applications [105], [137], [156]–[158], [162], [310], while the response is also highly tunable [148]. However, in order to couple to surface plasmons from incident radiation, one must overcome the wave-vector mismatch between the highly confined plasmons in graphene and the incident light. One approach to overcome this phase matching restriction involves nano-structuring the graphene, either using an external grating [311], patterning the graphene directly by etching ribbons as shown in Chapter 2 in Figure (2.5) [148] or by corrugating the surface [312]. However, the post-fabrication or etching of the graphene and surrounding materials used in these approaches invariably introduces defects; which have a negative impact on the electron mobility and therefore plasmon losses [313]. Peres et al [314] suggested an alternative approach is to periodically modulate the conductivity of the graphene. This could be achieved using the post-application of polymer top-gates to control the local Fermi level in graphene [315], functionalizing the graphene itself using scanning tunnelling microscopy [249], or by supporting the graphene layer with an array [316], removing the need for etching of the graphene. It was demonstrated in the models of Peres et al. that representing a spatial variation in conductivity with a single cosine leads to plasmons being supported by the graphene sheet [317]. In this thesis, a more attainable ribbon-like modulation in the conductivity of a graphene sheet, with areas of high and low conductivity as illustrated in Figure (2.1b), is considered.

3.1 Analytical modelling

It will be shown that the total response of this periodic system, of a continuous sheet of graphene with a spatially varying conductivity, arises from a hybridisation between the multipolar resonances supported by two regions in each unit cell. Extending this model to two layers, due to a small interlayer separation, compared to the incident wavelength, this system only supports symmetric resonances in each layer. By carefully tuning the conductivity profile, an increase, approaching 50%, can be achieved in the resonant absorption when both regions are made dipole resonant.

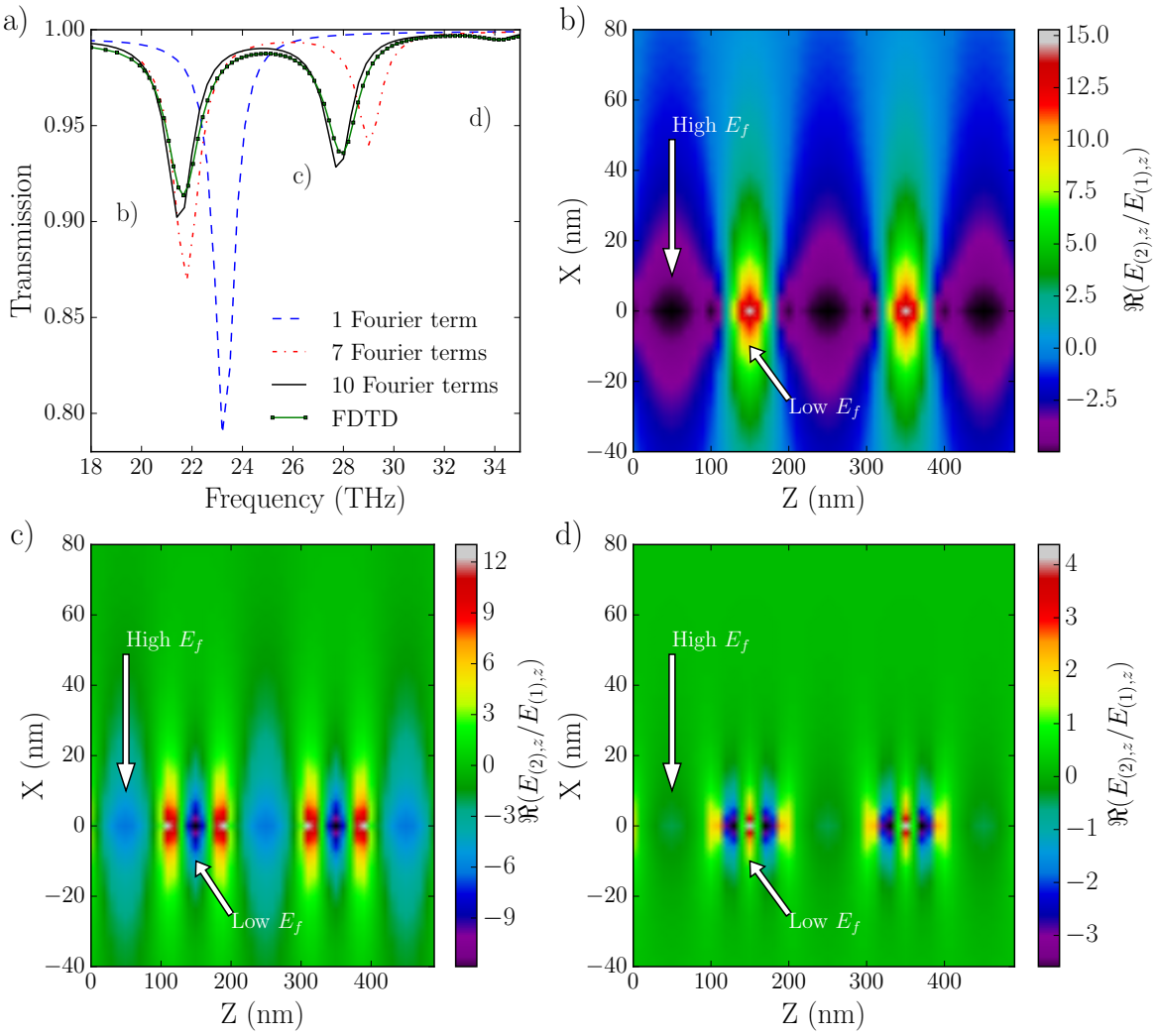

FIGURE 3.1: a) Modelling results for a single Fourier term, blue dashed line, 3 Fourier terms, (red dot-dashed line), 10 Fourier terms, (black solid line), and the finite difference time domain (FDTD) comparison in green circles. b), c), d) Real part of the in-plane electric field (E_z) normalised to the incident field at 22 THz, 27 THz, and 34 THz as labelled on a).

Following the model laid out in Chapter 2, the conductivity profile presented in Equation (2.8) is a sum over a number of Fourier terms. By increasing the number of Fourier components used to describe the square wave of Equation (2.8), the edges of the conductivity profile become more sharply defined, as illustrated in Figure (2.1a), with a single term, and Figure (2.1b), with many. In Figure (3.1a), the calculated transmission through a structure with profile described by a single Fourier term are compared to profiles described with an increasing number of Fourier terms. The period is taken to be $200\,\mathrm{nm}$ and the width of the high and low conductivity regions each taken to be $100\,\mathrm{nm}$. The Fermi level of the low conductivity region, the blue areas in Figure (2.1b), is fixed at a value of $0.1\,\mathrm{eV}$ with respect to the Dirac point, which is comparable to experimentally determined Fermi levels of ungated graphene [127].

All results presented in Figure (3.1) assume the Fermi level of the high conductivity region to be $0.3\,\mathrm{eV}$. For a conductivity profile with a single Fourier term (blue dashed line of Figure (3.1a)) the transmission displays a single deep minimum, as observed by Peres et al [314]. This behaviour arises due to the singular nature of the Fourier decomposition of the spatially varying response function, i.e. it is similar in origin to singular diffracted order observed for sinusoidal amplitude gratings [318]. Including higher order Fourier terms, (red dot-dashed line), results in the appearance of extra features in transmission. The results converge towards those obtained from a commercial finite difference time domain modelling package, when ten or more Fourier terms (black line) are included [253].

The most striking feature of the data in Figure (3.1a) is the appearance of extra dips in the transmission at $22\,\mathrm{THz}$, $28\,\mathrm{THz}$, and $34\,\mathrm{THz}$ as indicated by labels b, c, d. Through inspecting the electric fields at these resonant frequencies the origin of the minima in transmission can be understood. The real part of the in-plane electric field is plotted in Figure (3.1 b,c,d), at the frequencies indicated by Figure (3.1a). The regions corresponding to high and low conductivity are indicated by white arrows. Note that, while the out-of-plane electric field components change sign near the tips of a dipole, the in-plane electric field component are expected to be the same sign. Across the entire the region of high conductivity the electric field in Figure (3.1b) (purple region), c), and d) (light blue region) does not change sign, indicating a dipolar field. The electric field in the low conductivity region, on the other hand, displays multiple maxima and minima, indicative of multipolar resonances: one b) (red region) , three c) (red-blue-red) and five d) (red-blue-red-blue-red) peaks indicating a dipole, quadrupole and hexapole resonance, respectively. It is somewhat surprising that a modulation of conductivity gives rise to localised surface plasmons. However, it should be noted that if the conductivity in the low and high conductivity regions are similar, then the amplitude of the localised plasmons will be small.

3.1.1 Comparison to Isolated Ribbons

It is interesting to compare these complicated transmission spectra, presented in Figure (3.1a), with their multiple resonances, to the transmission expected for an array of isolated graphene ribbons. For a ribbon, the resonant frequency ω_0 of the dipole resonance is determined by

$$\omega_0 = \alpha_c \sqrt{\frac{e^2 E_f}{\hbar^2 \epsilon_{avg} \epsilon_0 w}}, \tag{3.1}$$

where E_f is the Fermi level of the graphene, ϵ_{avg} is the average permittivity of the regions 1 and 2 from Figure (2.1), w is the width of the graphene ribbon and $\alpha_c = 0.62$ is a dimensionless constant [148].

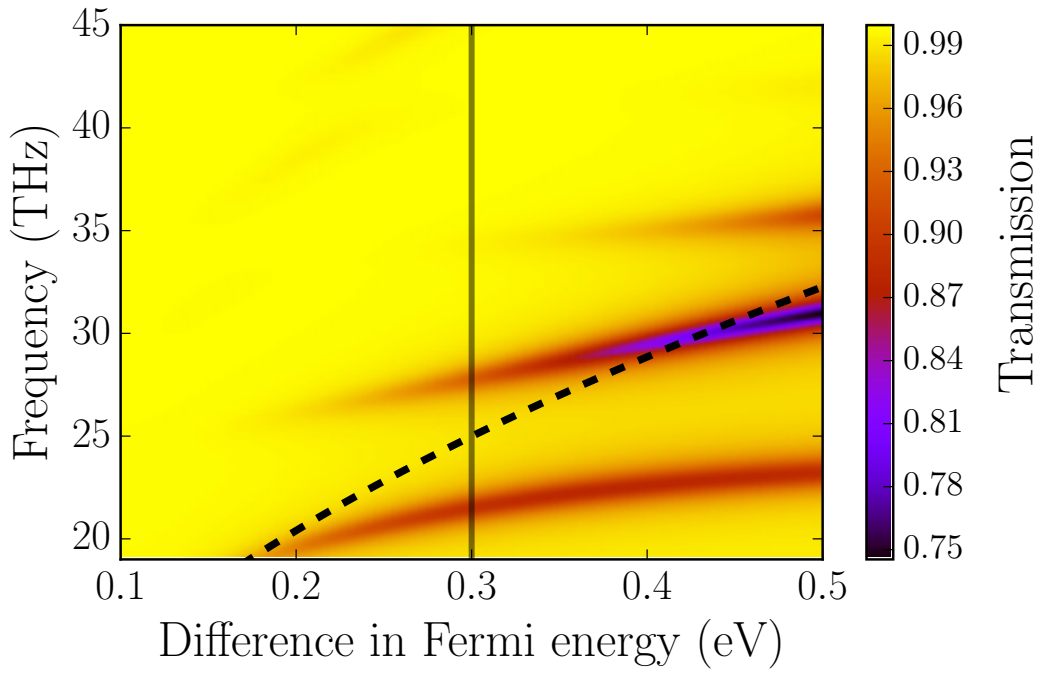

FIGURE 3.2: Transmission as a function of frequency and the difference between the Fermi level of the high and low conductivity regions. The structure is an array of modulated high and low conductivity regions, with different Fermi levels, with a period of 200 nm. The high conductivity region has a width of 100 nm. Dashed line is the position of the dipole resonance of an etched ribbon, with equivalent geometry and Fermi level as the highly conducting region. The dashed line is given by Equation (3.1). The shaded region indicates the equivalent of Figure (3.1a).

In Figure (3.2), the prediction for ribbons (Equation (3.1), dashed line) is compared with the transmission through the modulated conductivity structure, as the Fermi level of the

high conductivity region increases. The black-dashed lines represents the resonant frequency that isolated ribbons, with the same geometry and Fermi as to the highly conducting section of the modulated structure. Multiple resonances are observed occurring in the vicinity of the predicted dipole resonance given by Equation (3.1), when the multipolar modes of the low conductivity region overlap in frequency with the dipole mode of the high conductivity region. This indicates that the frequencies of the resonances supported by the structure are broadly determined by the dipole set up in the region of high Fermi level. Rather unexpectedly, these multipolar modes, which correspond to plasmon standing waves, as shown in Figure (3.1), excited in the low conductivity region, also depend on the Fermi level of the high conductivity region. These multipolar resonances couple more strongly to the incident radiation for frequencies near the expected dipolar resonance of the high conductivity region. The coupling between the dipole and multipolar modes in the two different regions is a defining feature of the system.

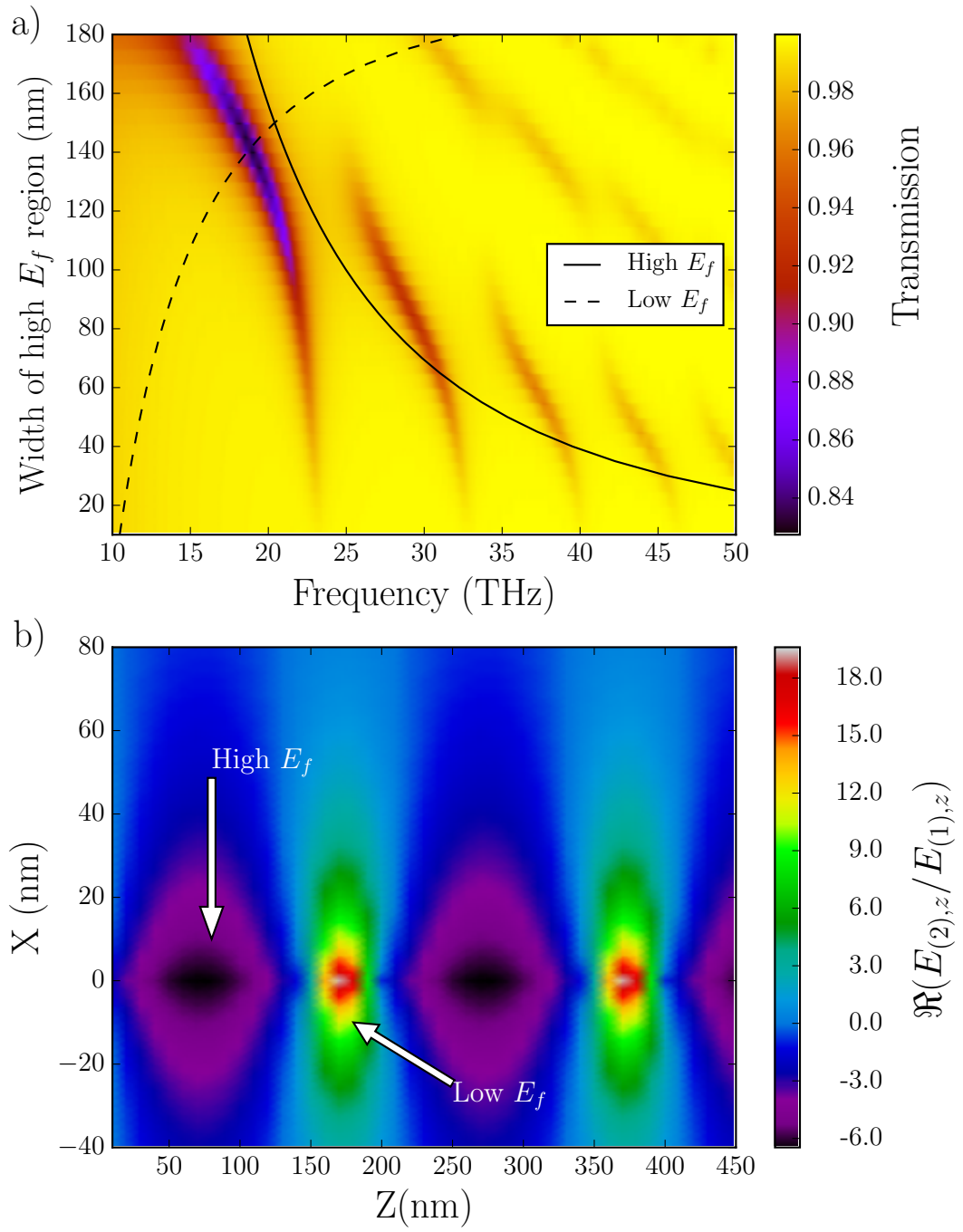

FIGURE 3.3: a) Transmission through a single layer, as a function of frequency and width of the high conductivity level region. The periodicity of the structure is 200 nm and the high conductivity region has a Fermi level of 0.3 eV. The position of the dipole frequency for the high conductivity region (solid line) and the low conductivity region (dashed line) is shown according to Equation (3.1). (b) The real part of the in-plane electric field, normalised to the incident field, at the cross over between the high Fermi level region and low Fermi level region, from (a).

3.1.2 Geometric Tuning

Since the resonance frequencies are determined by both material conductivity and geometry, it suggests the ability to independently tune these resonances, finding optimal conditions under which they couple to incident radiation. This question is addressed by fine tuning the widths of the high and low conductivity regions. To investigate this, the width of the high Fermi level region is varied, in a fixed period of 200 nm. The calculations for the transmission through this structure are presented in Figure (3.3a) along with the predictions for the dipole mode for the high (solid black line) and low (dashed line) conductivity regions. Again, several features are observed, corresponding to the mixing of the dipole resonance in the high conductivity region with the multipole resonances supported by the low conductivity region. However, by far the largest modulation of the transmission occurs where the dipole predictions for the regions of high and low conductivity intersect (given by the intersection of the dashed and solid lines in Figure (3.3a)). The in-plane electric field for the intersection point on Figure (3.3a) is shown in Figure (3.3b), with the regions of high and low conductivity indicated by arrows. As before, the absence of a change in sign of the electric field inside *both* regions indicates their dipolar nature. This doubly resonant behaviour results in a 50% increase in the modulation of the transmission compared to a structure with equally sized high and low conductivity regions.

3.1.3 Effect of a Multi-Layer Structure

An additional approach that one can follow to further increase the modulation of the transmission is to create stacked structures. The model is now extended to investigate two equivalent layers of graphene, each with an identical conductivity modulation, separated by a dielectric gap. This requires modification of Equations (2.12, 2.13, 2.14), in order to describe reflection from the second graphene layer. By applying the boundary conditions to both graphene layers, the modified form of Equations (2.30, 2.31) can be solved numerically, as before.

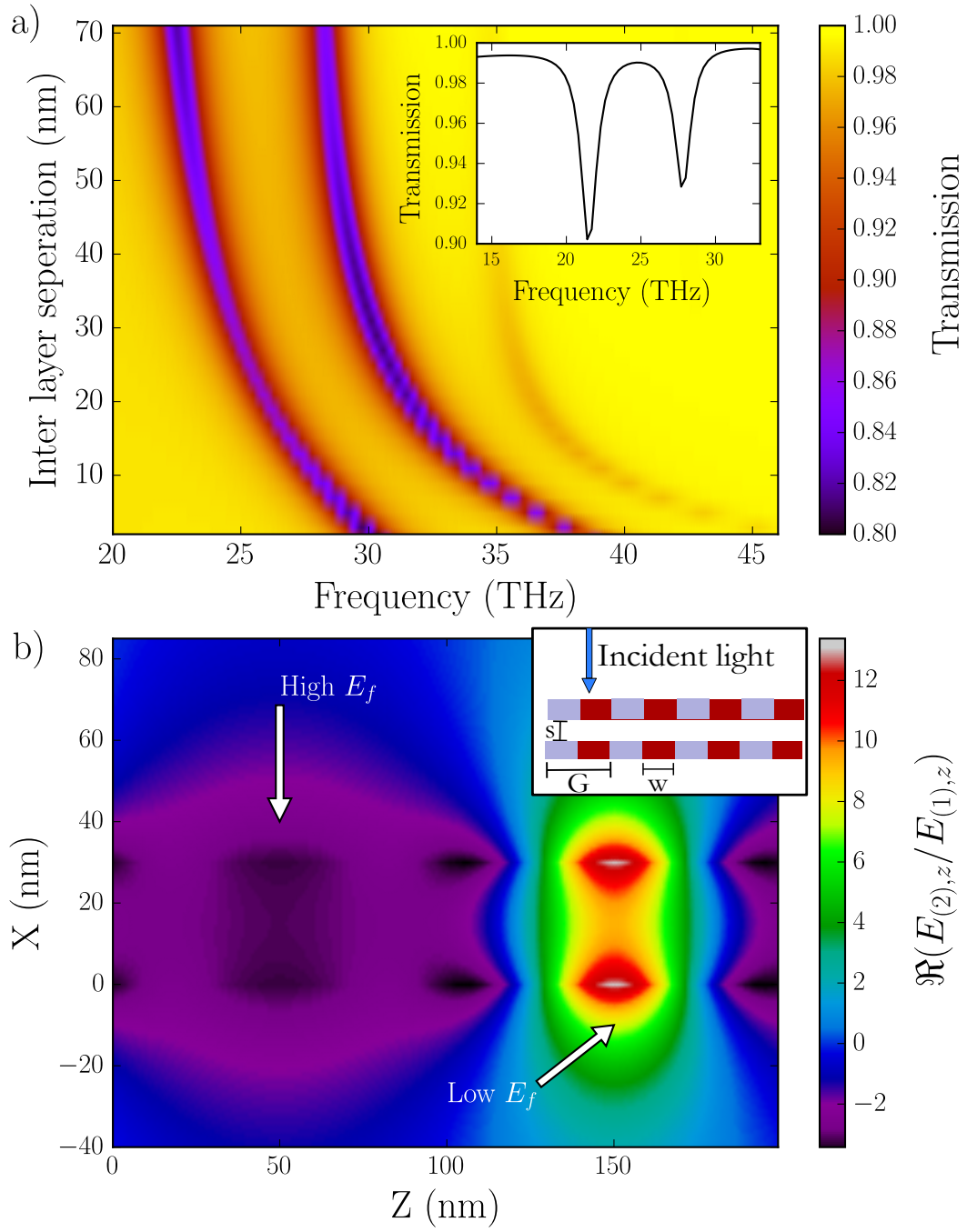

FIGURE 3.4: a) Transmission through a double layer of graphene with modulated conductivity regions as a function of the frequency and the interlayer separation. The width of the high conductivity region is 100 nm in a period of 200 nm and has a Fermi level of 0.3 eV. The minima (1) and maxima (2) in the modulation in the transmission are indicated. Inset: transmission through the equivalent single layer. The frequency behaviour of the double layer approaches that of a single layer of large separations ($d > 80nm$). b) Real part of the in-plane electric field, normalised to the incident field, for 100 nm conductivity region of 0.3 eV, separated by 30 nm. The regions of high and low conductivity are indicated. Inset: Schematic of the double layer of graphene with identical modulated conductivity profiles

In Figure (3.4), the effect of the separation between the layers on the transmission through the double layer structure is investigated. The conductivity modulation is defined by aligned low and high conductivity regions, each 100nm wide, with Fermi levels of $0.1\,\mathrm{eV}$ and $0.3\,\mathrm{eV}$ respectively. Firstly, the addition of a second layer leads to the expected twofold increase in the modulation of the transmission. However the resonant frequencies are observed to be dependent on interlayer separation. For large interlayer spacing, greater than the decay length of plasmons, the resonant frequencies approach those of a single layer, as shown by the inset in Figure (3.4a). For interlayer spacing smaller than approximately $70\,\mathrm{nm}$, the transmission minima shift to higher frequencies. This behaviour is similar to that observed for symmetrically coupled plasmon resonators [319], and arises from the alignment of dipolar fields of one plasmon resonator with the Coulomb field of the other. Since the separation between the layers is around two orders of magnitude smaller than the wavelength of incident light, coupling to the corresponding antisymmetric resonance is expected to be negligible, as confirmed in Figure (3.4b) by the absence of antisymmetric in-plane electric fields.

A rather subtle but surprising feature of the transmission behaviour shown in Figure (3.4 a) is the observed fluctuation in oscillator strength between the dipole (1) and quadrupole (2) modes as a function of interlayer spacing, for the conditions indicated by the arrows compared to large separations. The resonant transmission for the low frequency mode (1) firstly increases to a maximum at ~$20\,\mathrm{nm}$, before decreasing again for larger separations. Precisely the opposite behaviour is observed for the high frequency mode (2). A possible origin is the differing spatial decays of dipole and quadrupole fields.

Finally, both the interlayer spacing and widths of the conducting regions are tuned, in order to optimise coupling conditions. In Figure (3.5), the effect of varying the width of the high conductivity region is investigated, assuming an interlayer spacing of 30nm. The greatest modulation in the transmission is observed when the regions with high and low Fermi levels are both dipole resonant. Repeating these calculations for a range of separations shows that the strength of the modulation in the transmission is relatively insensitive to the separation between the graphene layers. Designing a structure, in which both regions in both layers support dipole resonances leads again to a large, ~50%, increase in the modulation of the transmission, compared to a double layer of equally sized high and low conductivity regions.

It is interesting to note the dependence of the resonant frequencies on the width of the high conductivity region (y-axis) as depicted in Figure (3.5). For certain conditions, the frequencies appear to follow the predictions for the dipole and quadrupole resonances of the high conductivity region (solid lines), while in other regions, a dependence similar to that predicted for the dipole, quadrupole and hexapole resonances of the low conductivity

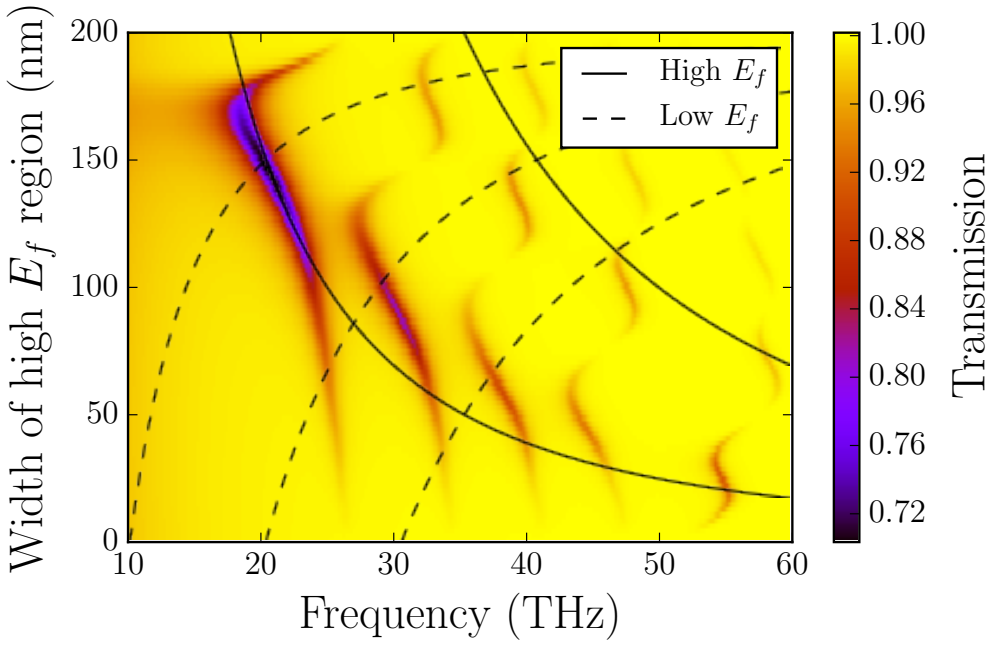

FIGURE 3.5: Transmission through a double layer structure as a function of frequency and the width of the high Fermi level region. The interlayer separation is 30 nm. The dipole and quadrupole frequency for the region of high conductivity region (solid line) and the dipole, quadrupole and hexapole frequency for the low conductivity region (dashed line) are shown according to Equation (3.1).

region (dashed lines) is observed. This leads to the rather curious S shaped features in Figure (3.5), and is indicative of the anti-crossing behaviour typical of strongly coupled resonators [320]. This anti-crossing behaviour is also observed to a lesser extent for a single layer (see Figure (3.3a)).

In conclusion a graphene sheet with a modulation in the conductivity has been investigated, using a modal matching approach. The total response of this periodic system arises from a hybridisation between the multipolar resonances supported by two regions in each unit cell. Extending this model to two layers, that due to the small interlayer separation compared to the incident wavelength, only symmetric resonances can be supported in each layer. By carefully tuning the conductivity profile, an increase, approaching 50%, can be achieved in the resonant absorption, when both regions are made dipole resonant. Given that these structures could in principal be fabricated from a continuous graphene sheet, i.e. without the need for graphene etching, with modulation depths comparable in magnitude to isolated nanostructures [321], such modulated structures may be a promising route to eliminating losses, introduced through fabrication, which currently plague etched samples [313].

Chapter 4

Third Harmonic Generation

As hinted at in Chapter 1 and Chapter 2, graphene displays a surprisingly large third order susceptibility. Moreover, the atomically thin nature of graphene allows for simple integration in cavity designs to increase this even further. In this chapter, the third harmonic generation from a graphene topped planar cavity, one specifically designed for this purpose, is measured. The nonlinear FDTD approach outlined in Chapter 2 is used to optimise the cavity dimensions and thicknesses. The integrated cavity is then characterised in experiment by recording the intensity of generated third harmonic as a function of incident wavelength. By comparing the graphene-integrated cavity and the cavity by itself, the harmonic signal can be seen to originate almost entirely from the graphene layer. A clear 117-fold enhancement in the normalised third harmonic power is observed at the resonant wavelength, relative to the third harmonic power for non-resonant wavelengths. Finally, a bulk value of $\chi^{(3)}$ can be deduced by comparing the measurements to the FDTD simulations. From this comparison, the bulk third order susceptibility of the graphene is found to be $\chi^{(3)} = 4 \times 10^{-17}\,(\mathrm{m/V})^2$.

4.1 Nonlinear FDTD Modelling

The FDTD model used starts by defining the linear optical response of the graphene layer through a bulk susceptibility, $\chi^{(1)}$, as,

$$1 + \chi^{(1)} = \epsilon_b + \frac{i\sigma_g}{\epsilon_0 \omega \Lambda}, \tag{4.1}$$

where ω is the frequency, ϵ_0 the permittivity of free space, $\epsilon_b = 2.5$ the background permittivity [261] and $\Lambda = 0.3\,\mathrm{nm}$, the thickness of the graphene sheet (as determined by ellipsometry measurements [260]). As introduced in Chapter 1, by applying the Kubo formula to graphene, and assuming $k_b T \ll E_f$, the surface conductivity of the graphene,

σ_g , can be expressed as [322] [121] [118],

$$\sigma_g = \frac{ie^2 E_f}{\pi\hbar(\omega + i\tau^{-1})} + \frac{e^2}{4\hbar}\left[\Theta(\hbar\omega - 2E_f) + \frac{i}{\pi}\log_{10}\left|\frac{\hbar\omega - 2E_f}{\hbar\omega + 2E_f}\right|\right]. \tag{4.2}$$

This expression accounts for both interband and intraband transitions in the graphene layer and describes the conductivity of graphene from infrared frequencies into the optical regime, as demanded in these experiments. The scattering rate, τ , is defined as, $\tau = E_f\mu/ev_f^2$, and Θ is the Heaviside step function. The Fermi energy, E_f = 0.2 eV, and mobility, $\mu = 1000\,\mathrm{cm^2V^{-1}s^{-1}}$, are set to values typical values for chemical vapour deposition (CVD) graphene [148][323]. The cavity is formed from a dielectric layer of SiO_2, with a thickness of 310 nm, and a conducting layer of gold with a thickness of 150 nm, as depicted in Figure (4.1a); the optical responses of these materials are wavelength dependent, as described by Palik [259]. In the experimental sample, a thin (8 nm) layer of titanium is required for adhesion, and this layer is also included in the model for completeness. The entire structure is modelled in 2D, assuming periodic boundary conditions in the planar directions. A vacuum box of 8 µm depth perpendicular to the graphene and a width of 200 nm in the plane of the graphene is included on the incident half space. Since the gold is optically thick, a vacuum box in the transmission half space is not required. A rectangular, conformal mesh is imposed on the entire structure, with a minimum mesh size of 0.025 nm. The wavelength dependent reflection of the cavity is calculated using a broadband pulse and by integrating the power derived from the Poynting vector, through a plane parallel to the graphene layer, 2 µm away from the surface. The nature of the FDTD method allows the fields inside the cavity for different wavelengths to be determined, as shown in Figure (4.1b, c).

Nonlinearity is introduced into the model by expanding the polarisation as a power series; introducing an effective third order susceptibility, $\chi^{(3)}$, as, [169]

$$\vec{P} = \epsilon_0(\chi^{(1)}\vec{E} + \chi^{(3)}\vec{E}^3). \tag{4.3}$$

Due to the centrosymmetry of graphene, $\chi^{(2)} = 0$. In the FDTD models, $\chi^{(3)}$ is treated as a perturbative fit parameter, allowing the generated third harmonic in the model to match that observed in experiment. To simulate as close as possible the experimental conditions, a pulse of a fixed carrier frequency, modulated with a Gaussian envelope was applied to the graphene layer, at normal incidence. This pulse has a full width half maximum (FWHM) of 100 fs, and a peak electric field amplitude of $2.3 \times 10^8\,\mathrm{Vm^{-1}}$ corresponding to an average power of 4.5 mW at the 1.05 kHz repetition rate used the experiment. The central wavelength is varied in the range of 1630 nm to 2400 nm. At each input wavelength, the

average power of third harmonic power generated is determined by again integrating the power derived from the Poynting vector across a plane parallel to the graphene, placed 2 μm from the surface. Figure (4.1d) shows how the generated third harmonic power is predicted to vary with the input wavelength, which is greatly enhanced at the resonance of the cavity. The cavity enhancement is defined as the ratio of the third harmonic power generated by a pulse with the resonant wavelength of 2080 nm, to the third harmonic power generated by a pulse with a non-resonant incident wavelength of 1630 nm. With this definition, the expected enhancement increases by factor of 85. This is comparable to the prediction made by Savostianova and Mikhailov [196].

The FDTD modelling can be used to explain the origin of the resonant enhancement. In Figure (4.1b, c), the time-averaged electric fields calculated for two different cases: on and off resonance are plotted. From Equation (4.3), it can be seen that the electric field plays an important role in determining the intensity of any nonlinear harmonic generation. The electric field profile of the resonant incident wavelength, 2080 nm, (blue dotted line) has a maximum at the surface of the graphene layer. The electric field profile of the third harmonic generated by this resonant wavelength, 693 nm (red solid line), also has a maximum at the graphene surface, making the cavity doubly resonant. This contrasts with a non-resonant case as shown in Figure (4.1c), plotted for an input wavelength of 1630 nm. While the field for the incident wavelength has a smaller magnitude at the surface of the graphene compared to that for the resonant wavelength, the electric field profile of third harmonic wavelength generated (i.e. 543 nm) is reduced by around a factor of four from the resonant condition.

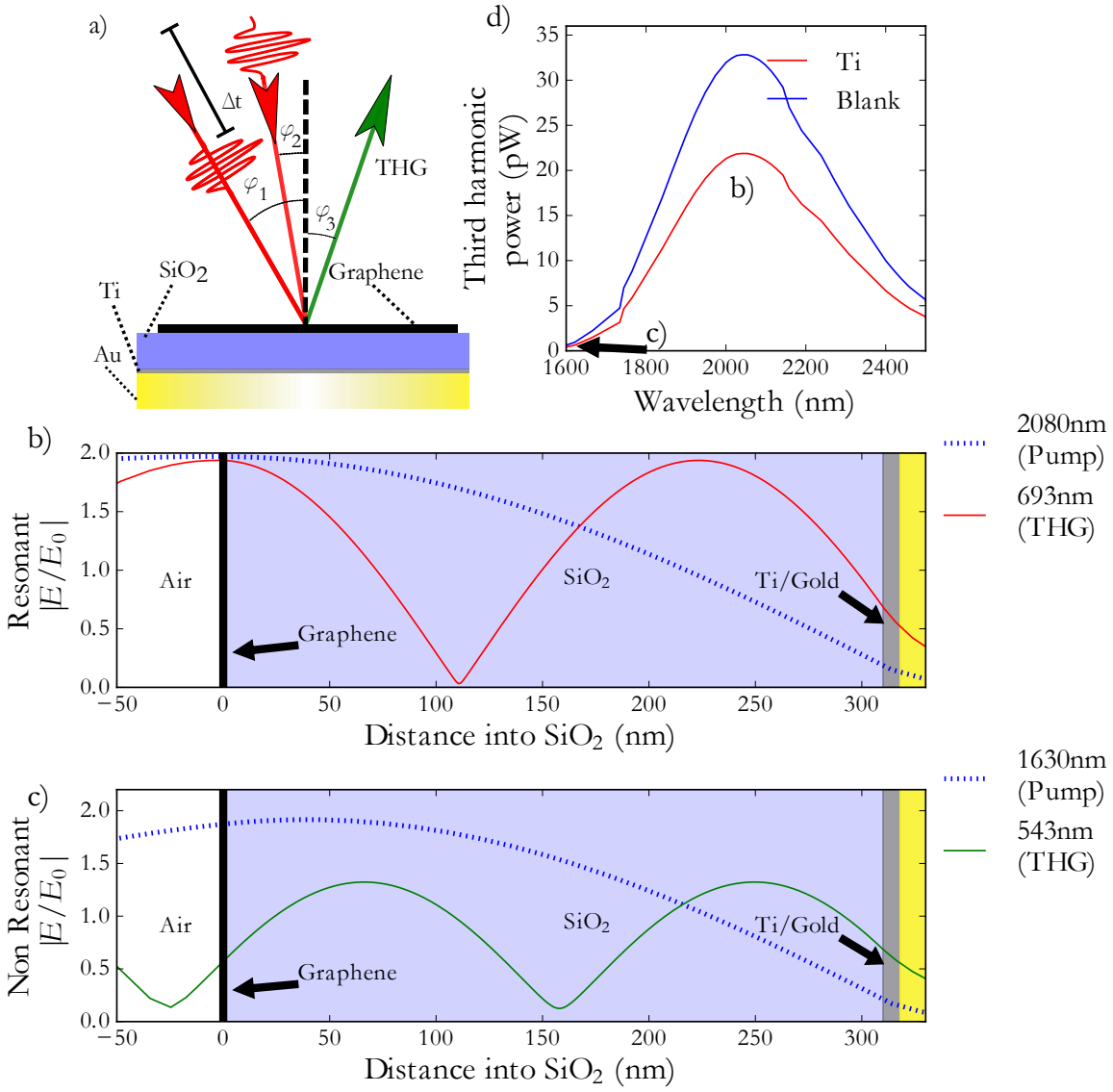

FIGURE 4.1: a) A diagram of experimental geometry and sample structure showing the two incident pulses separated by a variable delay time, Δt, the angles of incidence are; $\phi_1 = 30°$ and $\phi_2 = 8°$. The measured third harmonic signal is generated at $\phi_3 = 15°$. The thickness of the layers are; Au 150 nm, Ti 8 nm, SiO_2 309 nm. b) FDTD modelling of the electric field profile through the stack at the resonance condition. The incident wavelength is 2080 nm (blue dotted line) and the third harmonic wavelength is 693 nm (red solid line). c) FDTD modelling of the electric field profile through the sample away from the resonance condition. The incident wavelength of 1630 nm (solid green line) and a third harmonic wavelength is 543 nm (dotted blue). d) FDTD modelling prediction of third harmonic generated as a function of the incident wavelength. The wavelengths of the FDTD electric field profiles in b) and c) are labelled. A cavity with a 5 nm sticking layer (blue line) is compared to a cavity with no sticking layer (red line). There is a clear reduction in the resonant enhancement.

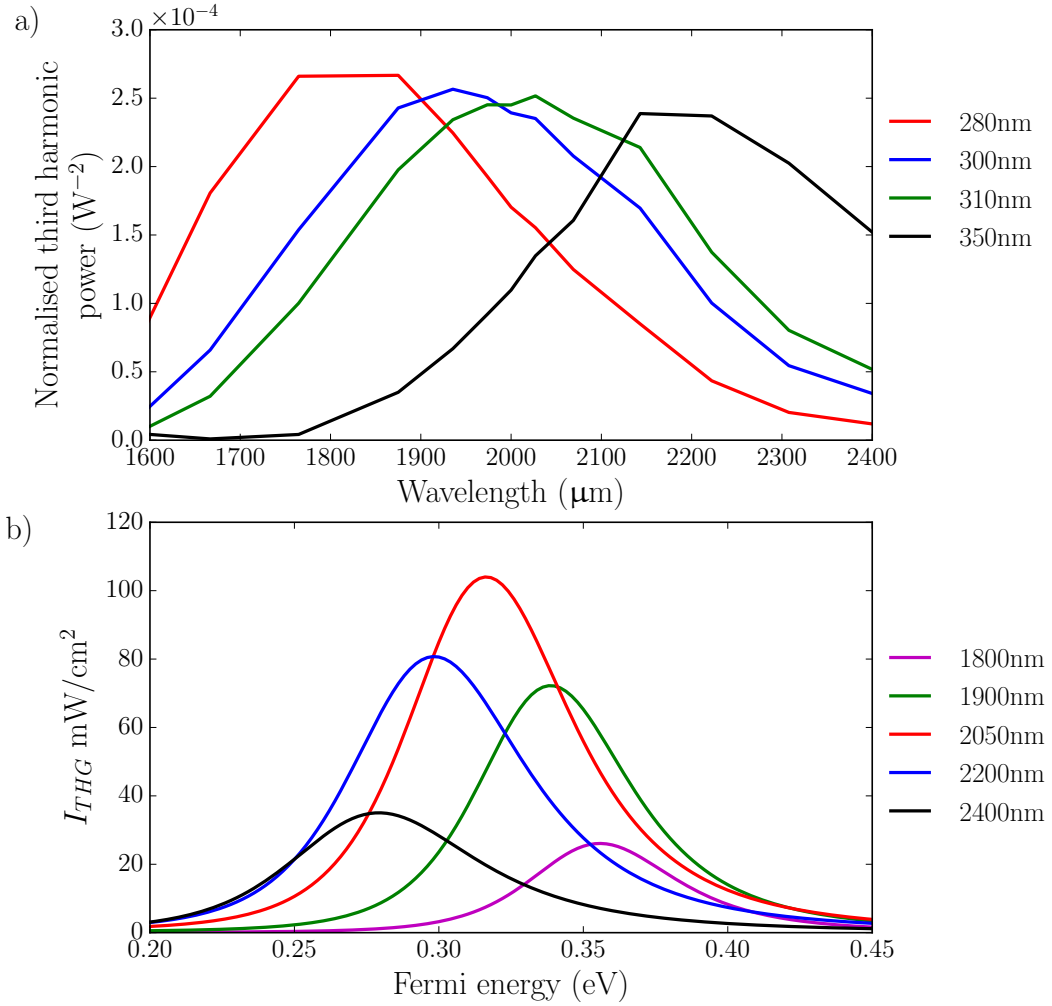

FIGURE 4.2: a) FDTD calculation for the dependence of the resonant enhancement on the thickness of the SiO_2 layer. Results are given for 280 nm(red line), 300 nm(blue line), 310 nm(green line) 350 nm(black line) showing the expected increase in the resonant frequency with increased thickness of SiO_2. b) Theoretical prediction of how the third harmonic intensity of the cavity changes a function of the Fermi level of the graphene for a selection of incident wavelengths, 2400 nm black, 2200 nm blue, 2050 nm red 1900 nm green, 1800 nm magenta, assuming a relaxation time of $\approx$ 10 fs [179]

FDTD modelling also facilitates an investigation into the parameters controlling the resonant behaviour of the cavity. Note that since the precise power of the incident beam has a large influence on the magnitude of the measured third harmonic power the "normalised third harmonic power" is plotted. This is the third harmonic power normalised to the cube of the reflected power, as measured power a thermal power meter. A central parameter to the where the resonant maximum occurs is the thickness of the SiO_2, as shown in Figure (4.2a). As the thickness is increased from 280 nm to 350 nm, the resonant frequency increases from

1800 nm to 2200 nm caused by the increasing path length within the cavity. While within the FDTD model the Fermi level of the graphene plays no role in determining the nonlinear interaction, resonant features in the third order behaviour have been predicted [324] [325] [179]. While devices, based on Bragg reflectors, with comparable enhancement factors to those predicted in Figure (4.1) and with much higher quality factors have been known about for some time for second harmonic generation [326] [327] [328]. Additionally, the enormous enhancement factors attainable with intricate ring-resonator structures have been used to produce devices with impressively low input powers [329]. In contrast to these devices the proposed layered structure could allow the Fermi level dependence of $\chi^{(3)}$to be investigated. The thickness of the SiO_2 layer has been designed with this in mind. This thickness of SiO_2 the cavity is resonant for a fundamental wavelength of ~2000 nm, corresponding to a Fermi level of ~0.3 eV. This level of doping is achievable with current FET devices [129][148]. This Fermi level dependence of $\chi^{(3)}$is modelled in Figure (4.2b). The figure shows the results of a theoretical prediction for how the third harmonic intensity of the cavity changes as a function of the Fermi level of the graphene, for a selection of incident wavelengths from 2400 nm (black), to 1800 nm (magenta). The plots are based on combining the cavity structure in Figure (4.1) with the calculations of Mikhailov [179]. A relaxation time of $\approx$ 10 fs, is used which is typical of CVD graphene [330] [218]. Figure (4.2 b) shows how a ~100 meV shift in the Fermi level of the graphene layer could completely modulate the harmonic signal generated from the cavity. As introduced in Chapter 1, this tunability can be used to created devices with fast switching speeds [111].

With the modelled parameters as a guide, a simple cavity on top of a glass microscope slide, used as a support substrate, is fabricated. A 5 nm layer of chrome is thermally evaporated onto the glass to provide an adhesive layer for the thermal evaporation of a 150 nm layer of gold. The samples are then cleaned in acetone, IPA and water and dried. Before the silicon dioxide deposition, the sample is exposed to an argon etch of 1 minute at a pressure of 30 mTorr and at 30 W RF power to remove possible contaminants. A second 5 nm titanium adhesion layer is then sputter-coated at a pressure of 2 mTorr and at 300 W DC power. Despite the reduction in the cavity performance as shown in Figure (4.1d), this sticking layer was vital for providing sufficient adhesion for the SiO_2 layer. From FDTD modelling, a titanium sticking layer was found to give the smallest reduction in the cavity enhancement. Finally, a SiO_2 layer is sputter-coated from a SiO_2 target, with a 2:1 Ar to O_2 gas ratio, at 2 mTorr and at 150 W RF power, using an AJA Orion sputterer. Using ellipsometric measurements, the thicknesses of the titanium and SiO_2 layers were confirmed to be 8 nm and 309 nm, respectively. An area,~1 cm^2, CVD graphene, is then transferred onto the sample using a PMMA assisted transfer technique as described in Chapter 2 [93][269].

4.2 Third Harmonic Measurement

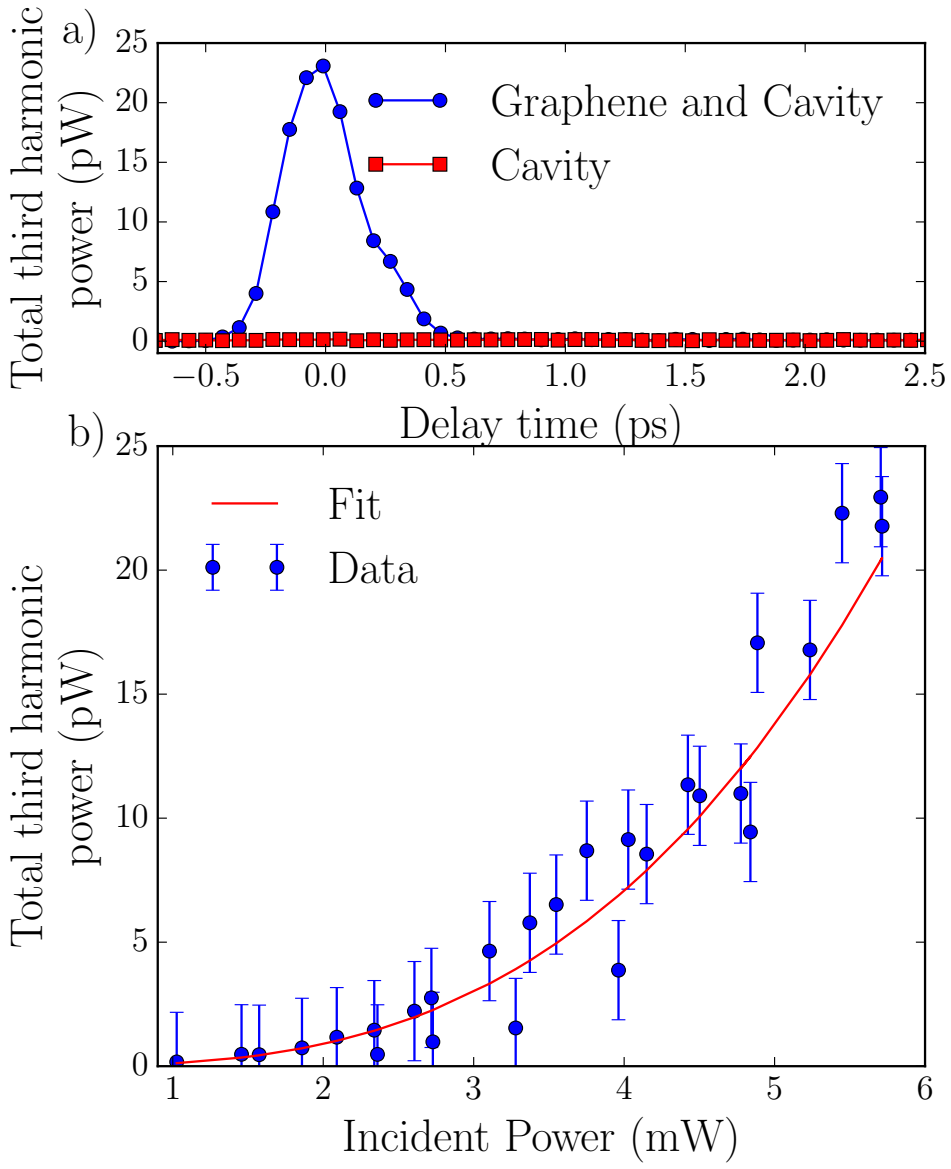

FIGURE 4.3: a) A typical time delay measurement of the total third harmonic generated, for $\lambda = 2080\,\text{nm}$, comparing an area on the sample with graphene (blue circles) to the response of just the cavity (red squares), incident power is 6.5 mW. b) Third harmonic generation as a function of the average incident power. The red line is a least-squares fit to the measured data points, found to be $P_{thg} \propto P_{inc}^3$.

To measure the third harmonic generation from this layered structure, a two-pulse correlation measurement was used, as shown in Figure (4.1a), allowing a background free characterisation of the sample. In this approach, two 1.05 kHz, 100 fs, TM polarised, laser pulses, with comparable fluences and a tunable central wavelength, in the range 1630 nm-2400 nm, are generated by an optical parametric amplifier. A thermal power meter, measuring the reflection of the incident pulse, allows for continuous monitoring of the average incident

power, typically ~6 mW. The temporal overlap of these two beams, Δt, at the sample interface is controlled by a motorised delay stage, changing the path length of one pulse and therefore the arrival time. When the beams are temporally and spatially overlapped, a third harmonic signal is expected to be generated at four different angles: 8°, 15°, 22° and 30° which allows for spatial filtering of the generated third harmonic signal.

To measure the harmonic signal, an avalanche photodiode, protected by an 800 nm short pass filter, is placed at $\phi_3 = 15°$, and connected to a lock-in amplifier. One of the incident beams is then modulated at 525 Hz via a mechanical chopper, and the voltage from the lock-in amplifier is recorded. The mechanical stage allows averaging of the recorded signal by repeatedly scanning the delay stage. The optimisation procedure outlined previously reduces the number of steps needed to be scanned, decreasing the measurement time. The sample is mounted on an xyz micrometer stage so that areas of the sample covered with graphene can be easily compared to areas free from graphene. Figure (4.3a) shows a typical measurement of third harmonic power measured as a function of the time delay between pulses for the combined graphene-cavity structure (blue circles). Note that the signal is broader than ~100 fs due to the non-collinear geometry. The measurement from the cavity alone, red squares on Figure (4.3a), confirms that the third harmonic signal originates predominantly from the graphene. The measurements comparing the third harmonic signal generated from the graphene-cavity structure to the cavity alone were repeated 8 times and on two different areas of the graphene sample and a total of three graphene samples were measured. The total third harmonic power generated is expected to be approximately four times the measured power, since there are four possible phase matching angles. For this reason, in Figure (4.3) and Figure (4.4), the total harmonic power is plotted as four times the measured value. To further investigate the origin of the signal, the total incident power is varied using a neutral density filter; the resulting third harmonic power, P_{thg}, is recorded and shown in Figure (4.3b). P_{thg} is expected to depend on the cube of the incident electric power, P_{inc}. Using a least-squares approach, the best fit to the data is $P_{thg} \propto P_{inc}^3$ (red line in Figure (4.3b)). Furthermore, the signal is also found to be highly sensitive to the angle of detection, disappearing completely as the position of the APD was moved, in steps of 0.5°, more than a degree away from the calculated value of ϕ_3, as expected for a coherent signal such as third harmonic generation.

4.3 Results from the Third Harmonic Measurement

The effect of the cavity on the third harmonic intensity generated can be investigated by simultaneously varying the wavelengths of both incident pulses from 1630 nm to 2400 nm and recording the third harmonic power on the detector and the reflected power. The results

in Figure (4.4a) show individual time-delay measurements, demonstrating the wavelength invariance of the time-delay scans. Importantly, these measurements also show the increase in third harmonic intensity as the incident wavelength increases from 1680 nm (black line) to 2100 nm (red line), approaching the resonant condition for the cavity. Figure (4.4 b) plot the maximum intensity from these individual time-delay scans (blue circle-line) with incident wavelengths in the range from 1630 nm to 2400 nm along with the FDTD prediction (red line). The transmission of the short-pass filter also influences the wavelength dependence of the third harmonic signal detected. As is shown in Figure (4.5), the filter displays fast oscillations with a gradual decrease of the transmission at shorter wavelengths and maximum transmission of 85% at longer wavelengths [331]. For these reasons, the results in Figure (4.4b), also compensate for the wavelength-dependent transmission of the 800 nm short pass filter.

Finally, Figure (4.4b) shows the measured resonant maximum occurs at longer wavelengths compared to the FDTD modelling. FDTD method, Figure (2.4), has known limitations in modelling sources with non-normal angles of incidence. Primarily, the effectiveness of the PML layers significantly decreases for angled source injection which can prevent the simulations from converging. For shallow angles of incidence, convergent simulations can be achieved by increasing the memory requirements of the simulation and increasing the thickness of the PML boundaries. Secondly, the more computationally-intensive Bloch boundary conditions, required to simulate a non-normal angled source, do not accurately simulate non-normal sources for nonlinear simulations. The angle of injection is frequency dependent and the angle quickly becomes large for the frequency range required in this thesis. These large source angles result in large reflections from the PML boundaries and prevents simulations for converging. While the non-collinear geometry, required for simultaneous power measurements, is difficult to simulate directly with the FDTD method, the increase in the effective path length inside the cavity can easily be compared to normal incidence. The increase in path length leads to the observed shift in the resonance to longer wavelengths as shown in the difference between the modelling prediction, (red line) and measurement (blue lines) in Figure (4.4b). Using Snell's law, the position of the resonance at 8° (dotted line) and 30° (dashed line) is marked on Figure (4.4b), shown relative to normal incidence (solid line). By comparing the measured harmonic signal on (2080 nm) and off (1630 nm) resonance, the enhancement can be estimated to be a factor of 117. This is in reasonable agreement with the value of 85 extracted from FDTD simulations, and with the estimates made by Savostianova and Mikhailov [196].

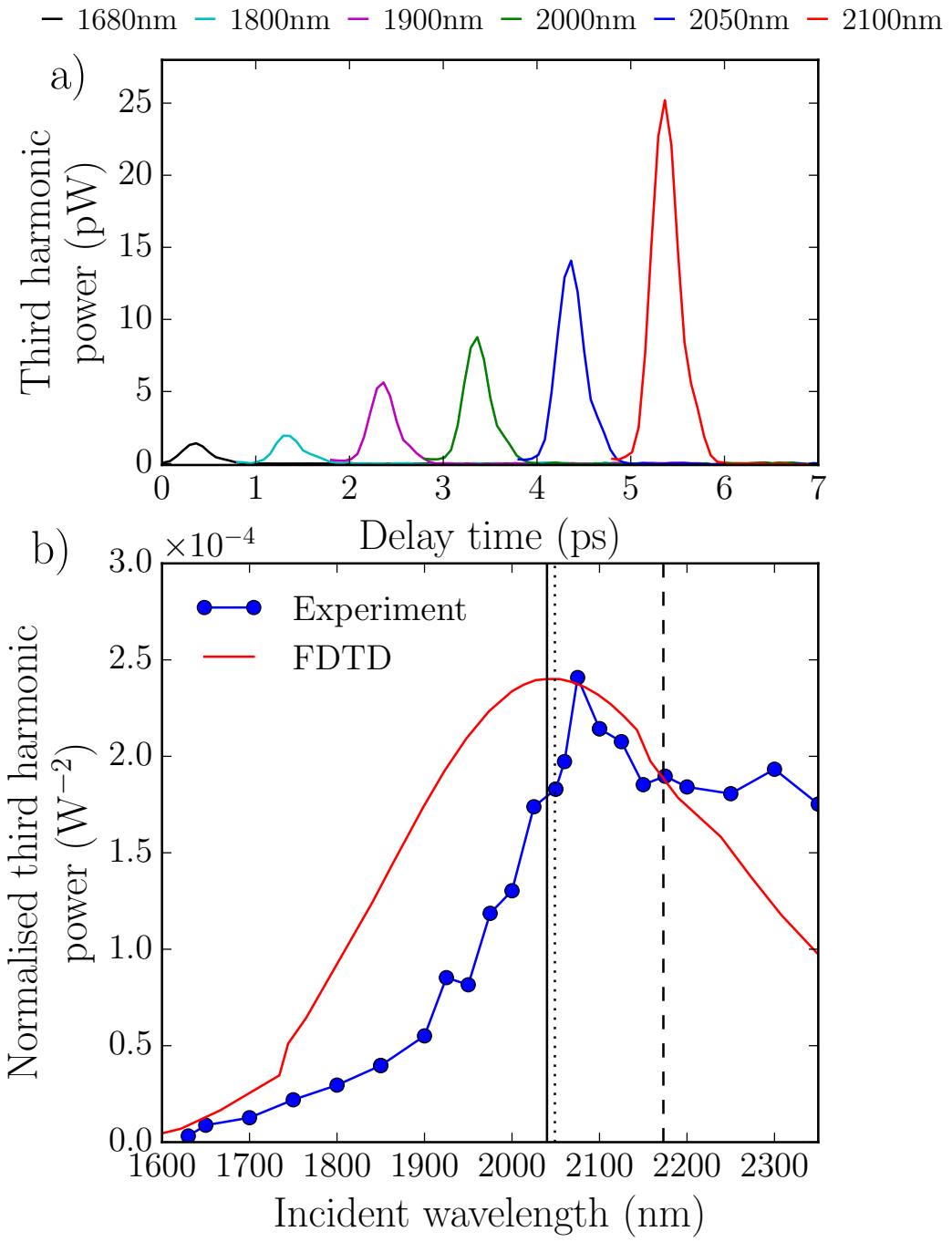

FIGURE 4.4: Time delay measurements at increasing incident wavelength. Results shown for wavelengths of 1680 nm (black line), 1800 nm (cyan line), 1900 nm (magenta line), 2000 nm (green line), 2050 nm (blue line), 2100 nm (red line). These wavelengths are offset by 1 ps for clarity. These measurements demonstrate the increase in third harmonic intensity as the incident wavelength approaches the resonant condition for the cavity. These measurements also demonstrate the wavelength invariance of the time-delay scans. b) The measured third harmonic power generated by the cavity, normalised to the time-average reflected power, as a function of the incident wavelength, comparing the FDTD modelling results from Figure (4.1d) (red line) with the measured values (blue circles), with a modelled incident power of ~4.5 mW. The shift in the position of the resonance, relative to normal incidence (solid line), are marked for incident angles of 8° (dotted line) and 30° (dashed line).

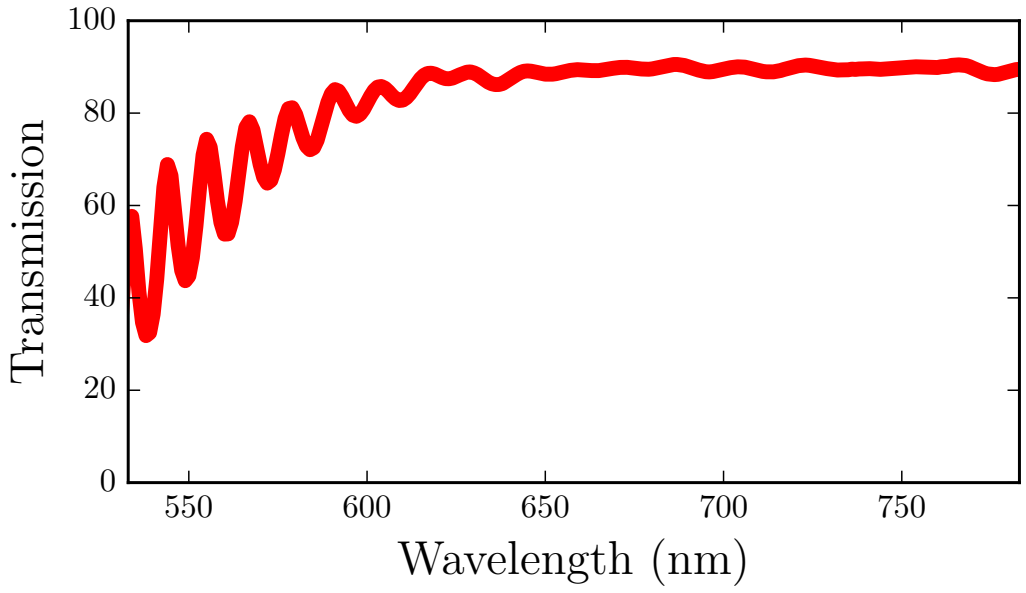

FIGURE 4.5: Wavelength dependence of the 800 nm short pass filter showing short wavelength oscillations. The plotted wavelength range is for the third harmonic generated from the experimental incident wavelength range in Figure (4.3) so is reduced by a factor of three.

To best match the absolute power measured in experiment, a bulk susceptibility in the model of $\chi^{(3)} = 4 \times 10^{-17}\,(\mathrm{m/V})^2$ was required. While the value of $\chi^{(3)}$ depends on the specific nonlinear process, with large values for $\chi^{(3)}$ being reported in fourwave mixing experiments [181], the value of $\chi^{(3)}$ reported in this thesis is comparable to the values obtained for the third harmonic generation experiments performed by Kumar et al. ($\chi^{(3)} = 4 \times 10^{-17}$,$8 \times 10^{-17}\,(\mathrm{m/V})^2$) [193] and the theoretical prediction of fourwave mixing by Zhang et al. ($\chi^{(3)} = 2 \times 10^{-17}\,(\mathrm{m/V})^2$) [194]. However it is considerably larger than the prediction for third harmonic generation by Cheng et al. ($\chi^{(3)} = 6 \times 10^{-19}\,(\mathrm{m/V})^2$)[195]. As noted by Cheng et al. themselves, this discrepancy may arise from a breakdown of the linear dispersion approximations, non-equilibrium electron dynamics or thermal effects, all of which are not treated in their perturbative model.

In summary, graphene has been shown to display a surprisingly large third order nonlinearity when placed in a planar cavity. The third harmonic signal generated from graphene is increased by a factor of 117 due to the integration with a resonant cavity. This rather large enhancement occurs as the cavity is resonant both for the fundamental field as well as the third harmonic field. By modelling this effect using the finite difference time domain approach, a value for the bulk third order susceptibility of graphene is found to be $\chi^{(3)} = 4 \times 10^{-17}\,(\mathrm{m/V})^2$.

Chapter 5

Strain Modulated Luminescence

While there is significant research interest into the intrinsic optical properties of graphene, additional interest is based on manipulating these intrinsic properties. Invariably, the wet chemical transfer method for CVD graphene introduces local variations of stain in graphene samples. Previous studies which monitored the level of strain have focused on improving fabrication techniques [96] [332]. However, strained graphene retains some useful properties. The density functional theory modelling (DFT) of Surya et al. and Yang et al. show how straining a graphene layer allows hydrogen to bind to the graphene surface more easily which is useful for hydrogen storage technology [333] [334]. Straining graphene was also predicted to create large pseudomagnetic field profiles. These otherwise unaccessible fields are required to study phenomena unique to graphene, such as the quantum Hall effect [335]. This prediction was confirmed with scanning tunnelling microscopy measurements of graphene bubbles which displayed magnetic fields of >300 Tesla [336].

Deliberately creating spatial strain profiles in graphene is an alternative method for avoiding both the degradation of the mobility introduced by etching-based nanofabrication [313] [337] and the influence of edge states [338] when producing graphene nanocircuits. The ability to design nanocircuits with a suitably designed strain profile, i.e. by using a substrate with microstructures cut into it, was investigated theoretically by Pereira and Neto [339]. Spatial strain profiles have also been investigated experimentally with micron-scale PDMS pyramids covered in CVD graphene [340]. Through monitoring the 2D peak position, as measured by Raman spectroscopy, Gill et al. have shown how the induced strain profile can be controlled by altering the aspect ratio of underlying PDMS pyramids [340]. Additionally, achieving spatial control over the functionalization of graphene is of great importance for applications where molecule specificity is greatly desired, such as future medical technology [341][342]. Graphene-based biosensors rely on detecting when a molecule of interest binds to a complementary molecule attached to the graphene surface [299][343]. Being able to design the spatial position of the bound-molecules presents an interesting avenue of research. Previous experiments by Wang et al. have demonstrated

spatial control over the chemical selectivity of graphene via patterning the supporting substrate [344]. Advantageously, strain engineering provides a chemical free route for creating custom designs in the properties of graphene without the need for etching and the time consuming nanofabrication process.

Creating complex strain patterns requires a characterisation tool to verify the level of strain created. While Raman spectroscopy is a powerful tool, producing high resolution spatial maps is time intensive and requires careful post-processing of the spectra. Fluorescence imaging provides an alternative to AFM and Raman mapping, as Shin et al. demonstrated by used the preferential binding of rhodamine molecule to identify grain boundaries in graphene [306]. Their study suggests the fluorescence imaging as a novel graphene characterisation tool. As introduced in Chapter 1, a single layer of graphene has a surprisingly large quenching effect on the luminescence intensity emitted from a fluorescent molecule. This chapter compares Raman spectroscopy to subsequent luminescence intensity from a rhodamine-pyrene molecule (RP) from two different samples, A and B. These measurements show a correlation between the spatial strain profile of the graphene and the spatial variation in luminescence intensity. A simple model of a dipole near a metallic plane is suggested as the origin of the observed correlation between the strain and luminescence intensity.

5.1 Raman Measurements

Two samples, designated A and B, were fabricated to check any observed correlations across multiple samples. These samples consist of an glass microscope slide to act as transparent support layer. A thin, $30\,\mathrm{nm}$, layer of aluminium was thermally evaporated on to the surface of the glass substrate to aid with determining the correct focal plane for the Raman and luminescence measurements and provided reference marks to aid with comparing the subsequent measurements. After throughly cleaning the sample after the thermal evaporation, an area of ~$1\,\mathrm{cm}^2$ of graphene was transfered on top. For sample A, the Raman measurements were taken from an area of graphene $1200\,\mu\mathrm{m}$ parallel to the aluminium marker and $200\,\mu\mathrm{m}$ away from the marker. For sample B, the area of graphene was sampled over a region which was $800\,\mu\mathrm{m}$ parallel to the aluminium marker and $300\,\mu\mathrm{m}$ away from the marker.

The Raman measurements of samples A and B are shown in Figure (5.1). A typical spectrum from strained graphene, shown in Figure (5.1a), has the positions of the positions of the G and 2D peak from unstrained and undoped graphene marked in vertical blue lines, demonstrating the shift in G and 2D peak position caused by strain and doping of the graphene layer. From these Raman spectra, the G and 2D peaks were fitted with a Gaussian

using a least-squares fitting routine allowing the peak positions to be extracted. The vector decomposition method presented in Chapter 2 is used to extract the Fermi level and the level strain from the Raman spectra [129]. This analysis starts by computing the shift in G and 2D peak position relative to undoped and unstrained graphene, as shown as the vertical blue lines in Figure (5.1a) and blue stars in Figure (5.1b, d). This observed shift in the position of the G and 2D peak depends on both the Fermi level and the level of strain.

Changes in strain and Fermi level give distinct contributions to the positions of the G and 2D peak. These contributions are along vectors indicated by the dashed line (strain) and solid line (Fermi level) in Figure (5.1b, d). This allows a unique vector to be formed between the position of the undoped and unstrained position (blue star) and an experimental point. Decomposing this vector into the contributions from strain and Fermi level, allows these quantities to be extracted from an experimental point. The results of this analysis are shown in Figure (5.1b, d) and the spread of points in the direction of the solid line immediately suggests the sample exhibits a large variation in the Fermi level of the graphene. This is confirmed by the vector decomposition, the variation in the Fermi level from sample A, Figure (5.1b), is $0.4\,\mathrm{eV}$ and $0.3\,\mathrm{eV}$ for sample B, Figure (5.1d). As introduced in Chapter 1 and theoretically investigated by Swathi and Sebastian [240], the Fermi level is only expected to influence the fluorescence intensity when the Fermi level is above half of the emission frequency of the fluorescent molecule. At energies greater than $2E_f$ the quenching from the graphene is reduced by Pauli blocking as supported by experiments. Conversely, these experiments observed no change in the fluorescence intensity for Fermi levels far below the emission frequency of the fluorescent molecule [245]. In this thesis, the Fermi levels extracted from Figure (5.1b, d) are far below the emission frequency of the rhodamine molecule, so the variation in Fermi level has no effect on the luminescence intensity and any changes are attributed to the strain.

These spatial strain maps can be averaged in two directions, the first to show the average strain parallel to the aluminium marker (blue triangles) and the second to show the average strain perpendicular to the aluminium marker (red circles). These average measurements are presented in Figure (5.1c, e). For both samples A and B the average strain is approximately constant parallel to the aluminium marker (blue triangles) but gradually reduces with increasing distance away from the aluminium marker (red circles). The observed spatial strain profile in the graphene sheet most likely arises due to a dragging effect during the transfer of the PMMA-graphene stack to the substrate, as shown in Figure (2.8c) Chapter 2.

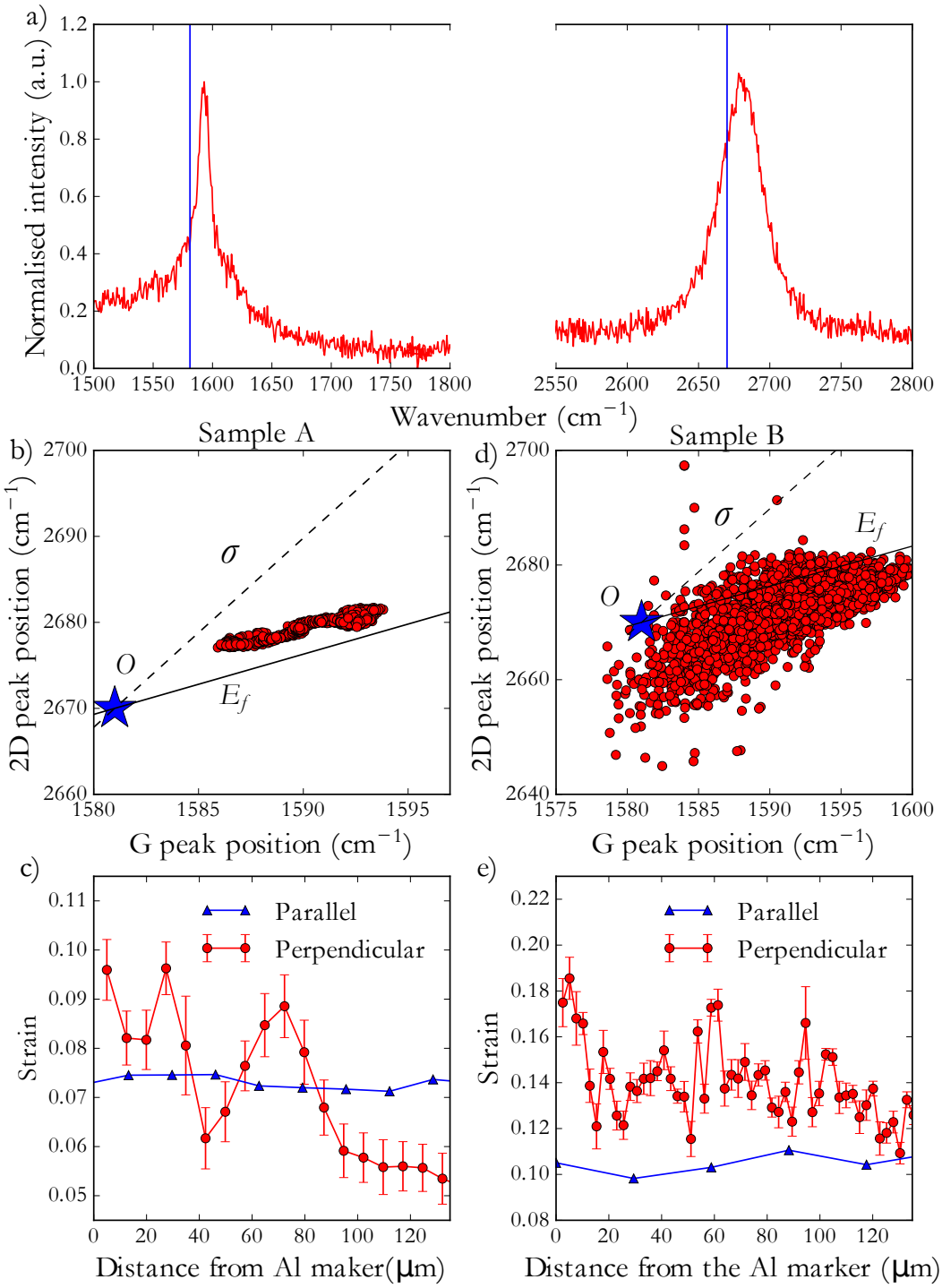

FIGURE 5.1: a) Typical Raman spectrum from strained graphene on a glass substrate. The positions of the G and 2D peak from undoped and unstrained graphene shown (vertical blue lines), note the broken x axis. b) Sample A, positions of the measured G and 2D peak with the position of undoped and unstrained graphene marked with a blue star. The contributions to the measured position due to strain, (dashed line), and Fermi level (solid line) are shown. c) Sample A, average strain, extracted from a) using the vector decomposition method outlined in Chapter 2, as a function of distance away from the aluminium marker (red circles) and along the aluminium maker (blue triangles). d) Sample B, Positions of the measured G and 2D peak with the position of undoped and unstrained graphene marked with a blue star. The contributions to the measured position due to strain, (dashed line), and Fermi level (solid line) are shown. e) Sample B, average strain, extracted from c) using the vector decomposition method outlined in Chapter 2, as a function of distance away from the aluminium marker (red circles) and along the aluminium maker (blue triangles).

5.2 Photoluminescence Measurements

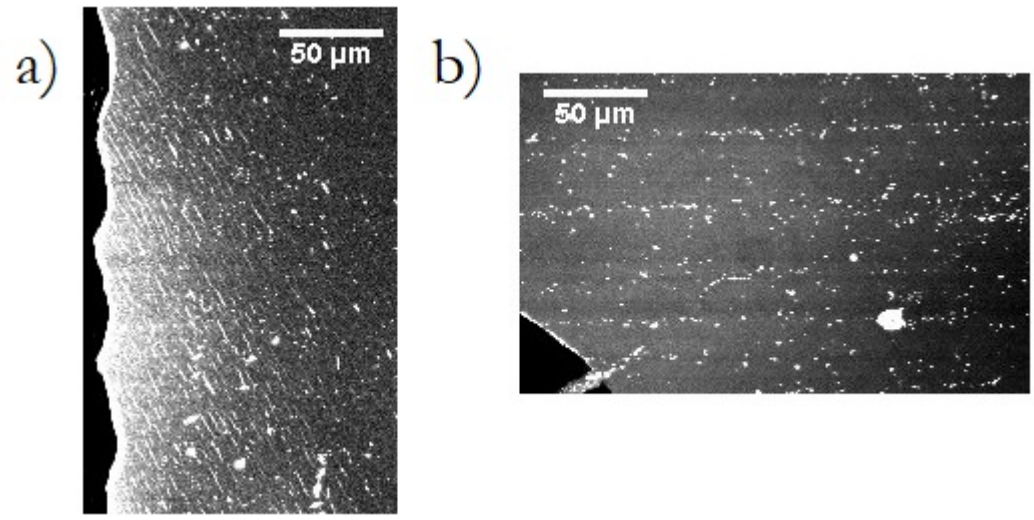

FIGURE 5.2: A) Typical luminescence images of the CVD graphene sample coated with the RP molecule from sample A shown in a) and sample B shown in b), with a scale bar of 50 µm. The edge of the aluminium marker is visible at the left hand edge of a) and the lower left corner of b). The bright lines and spots are from PMMA contamination from the graphene transfer.

Once these Raman measurements have been taken, the luminescent RP molecule is drop cast onto the graphene and the luminescence measurements are performed. The luminescence images were taken with a Leica TCS SP5 confocal microscope. The images were obtained at a 10 Hz refresh rate in air, at ambient temperatures. An excitation wavelength of 514 nm was used, to match the absorption spectrum of rhodamine [303]. Scanning mirrors allowed a 250 μm^2 area of the sample to be imaged. The emitted light is directed through an AOBS to select a wavelength range of 550 nm-680 nm to detect over. Figure (5.2) shows typical luminescence images showing the gradual decrease in luminescence intensity with increasing distance from the aluminium marker, visible in the left hand edge of the image. The very bright lines and dots are from PMMA contamination from the graphene transfer. The PMMA residue provides a spacer layer to separate the RP molecule from the surface of the graphene. The increased separation from the graphene surface reduces the quenching effect, leading to an increase in the luminescence intensity. Several luminescence images are taken over the 1200 µm region along the aluminium marker. Due to the low signal to noise ratio, the luminescence images were averaged perpendicular to the aluminium marker, then normalised to the signal at the aluminium marker. The averaged and normalised luminescence intensity is plotted in Figure (5.3). The large separation between the areas demonstrates this effect extends over a large distance.

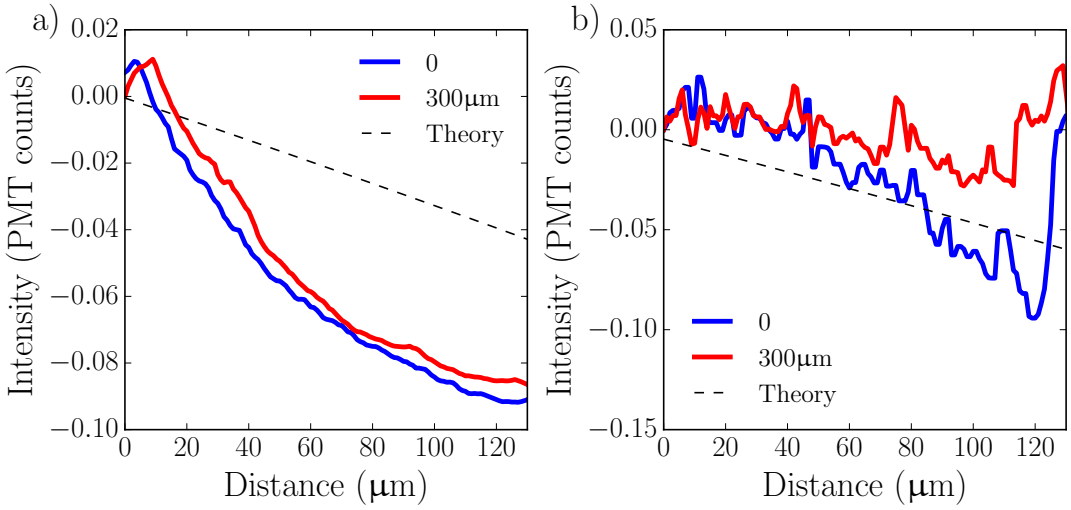

FIGURE 5.3: a) Normalised, average luminescence counts from sample A as a function of distance away from the aluminium marker. Different areas of graphene relative to a corner of the aluminium maker 0 μm (blue), 300 μm (red). b) Normalised, average luminescence intensity, as a function of distance from sample B. Areas averaged over for the red line and blue line are separated by 300 μm. The prediction for the expected reduction in luminescence, Equation (5.1), for the change in luminescence intensity from the observed strain in Figure (5.1) (dashed black line).

5.3 Model for the Fluorescence Quenching

These Raman and luminescence measurements suggest that the level of strain in a graphene sample is correlated to the luminescence intensity from the (RP) molecules on the surface of the graphene. Understanding the RP-graphene interaction in more detail will give an insight into the origins of the correlation between the strain and the luminescence intensity. The system of a molecule, described as a dipole, in close proximity to a metal surface has been heavily studied in the context of SERS Fleischmann1974[230][231][232], and reviewed in detail by Metiu [233]. This model starts by considering the electromagnetic fields incident on a molecule, the resulting polarisation and the emitted field. Bringing a molecule close to a surface can result in a variety of effects, from acting as a mirror for the emitted electromagnetic fields, or in the case of metals, coupling to electron-hole pairs to quench the luminescence emitted from the molecule [5]. The specific case of a molecule near to a layer of graphene was studied analytically by Gómez-Santos and Stauber who aimed to elucidate the mechanism that allows an atomically thin layer to be able to produce the significant quenching effect observed in several fluorescence experiments [23] [234] [235]. The dependence of the quenching effect on the separation, d, from the graphene layer that Gómez-Santos and Stauber derive is $\gamma_{quench} \propto (\lambda/d)^4$ and is valid for unusually

small separations. At these small separations the quenching effect becomes very large which supports the experimental observations [236]. The scaling of fluorescence intensity as d^{-4} was later confirmed experimentally [237] [238] with measurements of samples with increasing thicknesses of dielectric spacer layers.

Underpinning these experiments is the the model describing the quenching, relative to the vacuum decay rate, which is written as [345][245][346],

$$\frac{\Gamma}{\Gamma_0} = 1 + \frac{6\lambda_0^3}{32\pi^3}\int_0^\infty k_{||}^2 e^{-2k_{||}d}\mathrm{Im}\left(\frac{-2}{\epsilon + 1 + (4\pi\, i\sigma_g k_{||})/\omega}\right)\mathrm{d}k_{||}, \tag{5.1}$$

where λ_0 is the incident wavelength, Γ is the modified decay rate, Γ_0 is the vacuum decay rate and $k_{||}$ is the wavevector parallel to the graphene layer and σ_g is the conductivity of the graphene as described in Chapter 1. The distance between the emitter and the graphene layer, d, is set to $4\,\mathrm{nm}$, the radius of the rhodamine molecule [306]. As expected, Equation (5.1) is dependent on the conductivity of the graphene layer, which is directly related to the level of strain in the graphene. The work of Tielrooij shows that this local model for the conductivity of graphene is sufficient [245]. The strain-modified conductivity is inserted into Equation (5.1) to give a frequency-dependent prediction for how the luminescence intensity is modified by the strain the graphene layer. From tight-binding calculations, the strain is known to affect the conductivity of graphene as the following [347],

$$\sigma_{strain} = \sigma_g(1 - b_0(1+\nu)\epsilon), \tag{5.2}$$

where b_0 governs how quickly the intersite hopping energy changes with distance [348], with a value of ~4, based on tight binding predictions as is consistent with literature measurements [349] [347] [70][350], Poisson's ratio $\nu = 0.16$, based on measurements from bulk graphite [351]. This strain-induced change to the conductivity of graphene has been observed by Ni et al. [352]. Using the Raman measurements shown in FIG[a, c]Fig:Strain_8 for ϵ in Equation (5.2) gives an estimate on how the conductivity of graphene σ_g, given by Equation (1.8) in Chapter 1 [322], is affected by the observed compressive strain.

The prediction for how the fluorescence intensity varies for the experimental level of strain is shown in black dashed lines on Figure (5.3). Comparing these predictions for the fluorescence intensity to the measured fluorescence intensity shows that the prediction gives approximate agreement to the observed reduction in fluorescence intensity with reduced strain. This model is also supported by the observation that sample B displayed a higher level of strain which resulted in a larger maximum luminescence intensity.

In conclusion, CVD graphene was mapped using Raman spectroscopy and the spatial

strain profile extracted with a vector-decomposition method. The graphene was subsequently coated with a rhodamine-pyrene molecule and the spatial luminescence intensity recorded. The spatial behaviour of the luminescence measurements was seen to correlate with the spatial variation in strain. The expected fluorescence intensity was modelled with a simple dipole model near a graphene sheet and highlights how this correlation arises. The correlation between the level of strain in graphene and the fluorescence intensity has possible applications in assessing designer strain profiles in graphene. A removable molecule with strain-sensitive fluorescence properties could be used to rapidly asses the quality of an engineered spatial strain profile in graphene. Designing spatial strain profiles in graphene has applications for creating electronic circuits or for investing the behaviour of pseudo-magnetic fields [336].

Chapter 6

Conclusions and Future Work

6.1 Conclusions

In this thesis, methods for manipulating the interaction between light and a graphene layer have been presented. These interactions exist across a broad frequency spectrum, from the infrared into the visible, which highlights the wide range of technologies which graphene could be applied to.

Starting with the infrared regime, Chapter 3 investigated a graphene layer with a periodically modulated conductivity, using a bespoke modal-matching analytical model paired with FDTD modelling. The conductivity profile considered was an array of alternating high and low conductivity regions as an alternative to the widespread isolated ribbon structures. Both regions in the structure were shown to support resonances and the total response of this periodic system arises from the hybridisation between these multipolar resonances. Extending this model to two layers demonstrates that only symmetric resonances can be supported due to the small, compared to the incident wavelength, interlayer separation. As expected, the frequency of the resonance is dependent on the geometry of the conductivity region. By carefully tuning the geometry and the Fermi level of the spatial conductivity profile, an increase, approaching 50%, can be achieved in the resonant absorption. This condition occurs when both regions of the conductivity profile are made dipole resonant.

Bridging the infrared and optical regimes, Chapter 4 presented measurements of the third harmonic generation from graphene integrated with a cavity structure. A two-pulse correlation measurement was utilised to measure the third harmonic generated from the graphene-integrated cavity structure. The incident wavelength was varied from $1600\,\mathrm{nm}$ to $2400\,\mathrm{nm}$ to show an 117-fold enhancement in third harmonic generated for resonant as compared to non-resonant conditions. FDTD modelling elucidates that this large enhancement occurs as the cavity is resonant for both the fundamental field as well as the third harmonic field. The FDTD modelling also allows for a bulk third order susceptibility

of graphene to be determined, with $\chi^{(3)} = 4 \times 10^{-17}\,(\mathrm{m/V})^2$. Additionally, the theoretically predicted Fermi level dependence of $\chi^{(3)}$ is incorporated with these FDTD models to show how modest changes in Fermi level could produce significant switching of the third harmonic generated from the graphene-integrated structure.

Continuing into the optical regime, Chapter 5 presents an investigation into CVD grown graphene, which was mapped using Raman spectroscopy and the spatial strain profile extracted with a vector-decomposition method. The graphene was subsequently coated with a rhodamine-pyrene molecule to take luminescence intensity measurements. The spatial behaviour of the luminescence measurements correlated with the spatial variation in strain. The expected fluorescence quenching was modelled with a simple dipole model near a graphene sheet and highlights how this correlation arises. The correlation between the level of strain in graphene and the fluorescence quenching intensity has possible applications in assessing designer strain profiles in graphene for creating graphene-based electronics.

6.2 Future work

The proposed conductivity profile structures have dimensions that are within technological limits of electron beam lithography and require achievable Fermi levels. As a result, these designs could be fabricated from a continuous graphene sheet which would remove the need for etching of the graphene. Since modulation depths of the resonances supported are comparable in magnitude to isolated nanostructures [321], these modulated structures may be a promising route to eliminating losses [313]. Beyond the suggested fabrication methods of combining electron beam lithography with an ion-gel top gate, the photomodification behaviour of picosecond pulses provides a potential avenue for future investigation [130]. These optical pulses provide a contact-free method for creating custom patterns in a layer of graphene. Additionally, these spatial conductivity profile of graphene has been demonstrated as a method of controlling the propagation of plasmons in graphene [353]. The ability to spatially design the propagation behaviour of plasmons in graphene is a step towards the vision of Vakil and Engheta [160][159] of creating ultra-thin optical components, such as lenses.

As mentioned in Chapter 4, the cavity structure provides a route for further study into the role of the Fermi level on the third harmonic generation. The $300\,\mathrm{nm}$ thickness of the silicon dioxide layer was designed from this perspective. By adding electrical contacts, the cavity structure could act as FET device, similar to traditional silicon dioxide FET devices. Graphene-based FET devices can create a sizable shift in the Fermi level of graphene [107]. The enhancement in the third harmonic generation created by the stacked structure, combined with the FET geometry would facilitate an experimental investigation into

the Fermi level dependence of the nonlinear susceptibility of graphene and the predicted resonances in third order susceptibility of graphene [324] [325]. An important parameter in determining the level of doping that can be achieved through in FET geometry is the breakdown voltage of the silicon dioxide which is untested for the samples presented in this thesis. From a broader perspective, the atomically thin nature of graphene relaxes the otherwise stringent phase-matching conditions required for other nonlinear materials such as barium borate (BBO) and lithium triborate (LBO) [354][355]. As a result, graphene has already been integrated into an ultrafast fibre laser [356][187].

Finally, medical biosensing applications are based on seeding a graphene-based detector with a receptor that exclusively binds with a specific target molecule. This technique has recently been observed to bring large improvements to the sensitivity of the detection by Geo et al [357]. An interesting avenue for further investigation is using the strain-modulated luminescence effect for determining the level of active control over the position of a molecule on the surface of graphene. This external control could be achieved either with spatially controlled strain profiles or a modified surface diffusion [358], or another external stimulus.

Bibliography

[1] B. Huang, B. Hazen, and X. Zhuang, "Breaking the Diffraction Barrier: Super-Resolution Imaging of Cells", *Cell*, vol. 143, no. 7, pp. 1047–1058, 2010.

[2] W. H. Wollaston, "A Method of Examining Refractive and Dispersive Powers, by Prismatic Reflection", *Philosophical Transactions of the Royal Society of London*, vol. 92, no. January, pp. 365–380, 1802.

[3] B. Smith, *Fundamentals of Fourier transform infrared spectroscopy*, Second. CRC Press, 1996, ISBN: 9781420069297.

[4] R. Stulen and D. Sweeney, "Extreme ultraviolet lithography", *IEEE Journal of Quantum Electronics*, vol. 35, no. 5, pp. 694–699, 1999.

[5] L. Novotny and B. Hecht, *Principles of Nano-Optics*. Cambridge University Press, 2006, ISBN: 9781107005464.

[6] B. Jopson and A. Gnauck, "Dispersion Compensation for Optical Fiber Systems", *IEEE Cominications Magazine*, vol. 33, no. 6, pp. 96–102, 1995.

[7] Y. A. Vlasov, X.-Z. Bo, J. C. Sturm, and D. J. Norris, "On-chip natural assembly of silicon photonic bandgap crystals", *Nature*, vol. 414, no. November, pp. 289–293, 2001.

[8] I. W. Jung, S. B. Mallick, and O. Solgaard, "High-reflectivity Broadband Photonic Crystal Mirror MEMS With Low Dependence on Incident Angle and Polarization", *IEEE Journal of Micromechanical systems*, vol. 18, no. 4, pp. 924–932, 2009.

[9] T. D. Happ, M. Kamp, F. Klopf, J. P. Reithmaier, and A. Forchel, "Two-dimensional photonic crystal laser mirrors", *Semiconductor Science and Technology*, vol. 16, no. 4, pp. 227–232, 2001.

[10] S. Hu and S. M. Weiss, "Design of Photonic Crystal Cavities for Extreme Light Concentration", *ACS Photonics*, vol. 3, no. 9, pp. 1647–1653, 2016.

[11] E. Moreno, D. Erni, and C. Hafner, "Modeling of discontinuities in photonic crystal waveguides with the multiple multipole method", *Physical Review E*, vol. 66, no. 3, pp. 1–12, 2002.

[12] J. Joannopoulos, P. Villeneuve, and S. Fan, "Photonic crystals: putting a new twist on light", *Nature*, vol. 386, no. March, pp. 143–149, 1997.

[13] S. Fan, S. G. Johnson, J. D. Joannopoulos, C. Manolatou, and H. A. Haus, "Waveguide branches in photonic crystals", *Journal of the Optical Society of America B*, vol. 18, no. 2, pp. 162–165, 2001.

[14] A. Mekis, J. Chen, I. Kurland, S. Fan, P. Villeneuve, and J. Joannopoulos, "High Transmission through Sharp Bends in Photonic Crystal Waveguides", *Physical Review Letters*, vol. 77, no. 18, pp. 3787–3790, 1996.

[15] T. Søndergaard and K. H. Dridi, "Energy flow in photonic crystal waveguides", *Physical Review B*, vol. 61, no. 23, pp. 15 688–15 696, 2000.

[16] B.-S. Song, S. Noda, T. Asano, and Y. Akahane, "Ultra-high-Q photonic double-heterostructure nanocavity", *Nature Materials*, vol. 4, no. 3, pp. 207–210, 2005.

[17] D. Conteduca, C. Reardon, M. G. Scullion, F. Dell'Olio, M. N. Armenise, T. F. Krauss, and C. Ciminelli, "Ultra-high Q/V hybrid cavity for strong light-matter interaction", *APL Photonics*, vol. 2, no. 8, pp. 086 101–1, 2017.

[18] M. J. Burek, Y. Chu, M. S. Z. Liddy, P. Patel, J. Rochman, S. Meesala, W. Hong, Q. Quan, M. D. Lukin, and M. Lončar, "High quality-factor optical nanocavities in bulk single-crystal diamond", *Nature Communications*, vol. 5, no. May, pp. 5718–7, 2014.

[19] A.-P. Hynninen, J. H. J. Thijssen, E. C. M. Vermolen, M. Dijkstra, and A. van Blaaderen, "Self-assembly route for photonic crystals with a bandgap in the visible region.", *Nature Materials*, vol. 6, no. March, pp. 202–205, 2007.

[20] A. B. Khanikaev, S. H. Mousavi, W.-k. Tse, M. Kargarian, A. H. Macdonald, and G. Shvets, "Photonic topological insulators", *Nature Materials*, vol. 12, no. March, pp. 233–239, 2013.

[21] J. B. Pendry, "Controlling Electromagnetic Fields", *Science*, vol. 312, no. 5781, pp. 1780–1782, 2006.

[22] U. Leonhardt, "Optical Conformal Mapping", *Science*, vol. 312, no. 5781, pp. 1777–1780, 2006.

[23] Z. Chen, S. Berciaud, C. Nuckolls, T. F. Heinz, and L. E. Brus, "Energy transfer from individual semiconductor nanocrystals to graphene", *ACS Nano*, vol. 4, no. 5, pp. 2964–2968, 2010.

[24] J. Gomez-Diaz and A. Alu, "Flatland Optics with Hyperbolic Metasurfaces", *ACS Photonics*, vol. 3, no. 12, pp. 2211–2224, 2016.

[25] V. C. Nguyen, L. Chen, and K. Halterman, "Total transmission and total reflection by zero index metamaterials with defects", *Physical Review Letters*, vol. 105, no. 23, pp. 1–5, 2010.

[26] H. Raether, *Surface Plasmons on Smooth and Rough Surfaces and on Gratings*. Springer Berlin Heidelberg, 1988, ISBN: 978-3-540-17363-2.

[27] E. Hao and G. C. Schatz, "Electromagnetic fields around silver nanoparticles and dimers", *Journal of Chemical Physics*, vol. 120, no. 1, pp. 357–366, 2004.

[28] J. R. Hook and H. E. Hall, *Solid state physics*, Second. John Wiley & Sons, 1991, ISBN: 9780471928058.

[29] A. J. Haes, C. L. Haynes, A. D. Mcfarland, and G. C. Schatz, "Plasmonic Materials for Surface-Enhanced Sensing and Spectroscopy", *MRS BULLETIN*, vol. 30, no. May 2005, pp. 368–375, 2017.

[30] R. M. Ma, R. F. Oulton, V. J. Sorger, and X. Zhang, "Plasmon lasers: Coherent light source at molecular scales", *Laser and Photonics Reviews*, vol. 7, no. 1, pp. 1–21, 2013.

[31] W. L. Barnes, "Surface plasmon–polariton length scales: A route to sub-wavelength optics", *Journal of Optics A: Pure and Applied Optics*, vol. 8, no. 4, S87, 2006.

[32] P. Berini, "Long-range surface plasmon-polariton waveguides in silica", *Journal of Applied Physics*, vol. 102, no. 5, pp. 484–588, 2007.

[33] P. Berini, A. Olivieri, and C. Chen, "Thin Au surface plasmon waveguide Schottky detectors on p-Si", *Nanotechnology*, vol. 23, no. 44, pp. 444 011–9, 2012.

[34] T. J. Davis, D. E. Gómez, and A. Roberts, "Plasmonic circuits for manipulating optical information", *Nanophotonics*, vol. 6, no. 3, pp. 543–559, 2016.

[35] V. J. Sorger, R. F. Oulton, R.-M. Ma, and X. Zhang, "Toward integrated plasmonic circuits", *MRS Bulletin*, vol. 37, no. 08, pp. 728–738, 2012.

[36] E. Kretschmann and H. Raether, "Radiative Decay of Non Radiative Surface Plasmons Excited by Light", *Zeitschrift für Naturforschung*, vol. 23, no. 12, pp. 2135–2136, 1968.

[37] A. Otto, "Excitation of nonradiative surface plasma waves in silver by the method of frustrated total reflection", *Zeitschrift für Physik*, vol. 216, no. 4, pp. 398–410, 1968.

[38] A. V. Kabashin, P. Evans, S. Pastkovsky, W. Hendren, G. A. Wurtz, R. Atkinson, R. Pollard, V. A. Podolskiy, and A. V. Zayats, "Plasmonic nanorod metamaterials for biosensing", *Nature Materials*, vol. 8, no. 11, pp. 867–871, 2009.

[39] A. G. Brolo, "Plasmonics for future biosensors", *Nature Photonics*, vol. 6, no. 11, pp. 709–713, 2012.

[40] A. D. Humphrey and W. L. Barnes, "Plasmonic surface lattice resonances on arrays of different lattice symmetry", *Physical Review B*, vol. 90, no. 7, pp. 1–8, 2014.

[41] K. L. Kelly, E. Coronado, L. L. Zhao, and G. C. Schatz, "The Optical Properties of Metal Nanoparticles: The Influence of Size, Shape, and Dielectric Environment", *The Journal of Physical Chemistry B*, vol. 107, no. 3, pp. 668–677, 2003.

[42] K. S. Lee and M. A. El-Sayed, "Gold and silver nanoparticles in sensing and imaging: Sensitivity of plasmon response to size, shape, and metal composition", *Journal of Physical Chemistry B*, vol. 110, no. 39, pp. 19 220–19 225, 2006.

[43] J. N. Anker, W. P. Hall, O. Lyandres, N. C. Shah, J. Zhao, and R. P. V. Duyne, "Biosensing with plasmic nanostructure", *Nature Materials*, vol. 7, no. June, pp. 8–10, 2008.

[44] N. I. Zheludev, "A roadmap for metamaterials", *Optics and Photonics News*, vol. 22, no. 3, pp. 30–35, 2011.

[45] M. L. Weber and K. A. Willets, "Nanoscale studies of plasmonic hot spots using super-resolution optical imaging", *MRS Bulletin*, vol. 37, no. 8, pp. 745–751, 2012.

[46] W. L. Barnes, A. Dereux, and T. W. Ebbesen, "Surface plasmon subwavelength optics", *Nature*, vol. 424, no. 6950, pp. 824–830, 2003.

[47] H. A. Atwater, "The Promise of Plasmonics", *Scientific American*, vol. 296, no. 4, pp. 56–62, 2007.

[48] T. W. Ebbesen, C. Genet, and S. I. Bozhevolnyi, "Surface-plasmon circuitry", *Physics Today*, vol. 61, no. 5, pp. 44–50, 2008.

[49] E. Ozbay, "Plasmonics : Merging Photonics and Electronics at Nanoscale Dimensions", *Science*, vol. 189, no. 2006, pp. 189–194, 2012.

[50] C. Novo, A. M. Funston, and P. Mulvaney, "Direct observation of chemical reactions on single gold nanocrystals using surface plasmon spectroscopy", *Nature Nanotechnology*, vol. 3, no. 10, pp. 598–602, 2008.

[51] D. Pacifici, H. J. Lezec, and H. A. Atwater, "All-optical modulation by plasmonic excitation of CdSe quantum dots", *Nature Photonics*, vol. 1, no. 7, pp. 402–406, 2007.

[52] A. N. Grigorenko, N. W. Roberts, M. R. Dickinson, and Y. Zhang, "Nanometric optical tweezers based on nanostructured substrates", *Nature Photonics*, vol. 2, no. 6, pp. 365–370, 2008.

[53] J. A. Dionne and H. A. Atwater, "Plasmonics: Metal-worthy methods and materials in nanophotonics", *MRS Bulletin*, vol. 37, no. 08, pp. 717–724, 2012.

[54] A. Castellanos-Gomez, "Why all the fuss about 2D semiconductors?", *Nature Photonics*, vol. 10, no. 4, pp. 202–204, 2016.

[55] Y. Wang, T. Li, and S. Zhu, "Graphene-based plasmonic modulator on a groove-structured metasurface", *Optics Letters*, vol. 42, no. 12, pp. 2247–2250, 2017.

[56] H. A. Atwater and A. Polman, "Plasmonics for improved photovoltaic devices.", *Nature Materials*, vol. 9, no. 3, pp. 205–13, Mar. 2010.

[57] K. S. Novoselov, A. K. Geim, S. Morozov, D. Jiang, Y. Zhang, S. Dubonos, I. Grigorieva, and A. Firsov, "Electric field effect in atomically thin carbon films", *Science*, vol. 306, no. 5696, pp. 666–669, Oct. 2004.

[58] K. S. Novoselov, Z Jiang, Y. Zhang, S. Morozov, H. Stormer, U. Zeitler, J. Maan, G. Boebinger, P. Kim, and A. Geim, "Room-temperature quantum Hall effect in graphene", *Science*, vol. 315, no. 5817, pp. 1379–1379, 2007.

[59] P. M. Ostrovsky, I. V. Gornyi, and A. D. Mirlin, "Theory of anomalous quantum Hall effects in graphene", *Physical Review B*, vol. 77, no. 19, pp. 195 430–13, 2008.

[60] C. Lee, X. Wei, J. W. Kysar, and J. Hone, "Measurement of the Elastic Properties and Intrinsic Strength of Monolayer Graphene", *Science*, vol. 321, no. July, pp. 385–388, 2008.

[61] J.-W. Jiang, J.-S. Wang, and B. Li, "Young's modulus of graphene: A molecular dynamics study", *Physical Review B*, vol. 80, no. 11, pp. 1 134 051–6, 2009.

[62] N. Savvides and T. J. Bell, "Microhardness and Young's modulus of diamond and diamondlike carbon films", *Journal of Applied Physics*, vol. 72, no. 7, pp. 2791–2796, 1992.

[63] D. Armstrong, A. J. Wilkinson, and S. G. Roberts, "Measuring anisotropy in Young's modulus of copper using microcantilever testing", *Journal of Materials Research*, vol. 24, no. 11, pp. 3268–3276, 2009.

[64] C. Chen, S. Rosenblatt, K. I. Bolotin, W. Kalb, P. Kim, I. Kymissis, H. L. Stormer, T. F. Heinz, and J. Hone, "Performance of monolayer graphene nanomechanical resonators with electrical readout.", *Nature Nanotechnology*, vol. 4, no. 12, pp. 861–867, 2009.

[65] J. S. Bunch, A. M. van der Zande, S. S. Verbridge, I. W. Frank, D. M. Tanenbaum, J. M. Parpia, H. G. Craighead, and P. L. McEuen, "Electromechanical Resonators from Graphene Sheets", *Science*, vol. 315, no. January, pp. 490–493, 2007.

[66] A. A. Balandin, S. Ghosh, W. Bao, I. Calizo, D. Teweldebrhan, F. Miao, and C. N. Lau, "Superior thermal conductivity of single-layer graphene", *Nano Letters*, vol. 8, no. 3, pp. 902–907, 2008.

[67] D. R. Lide, *CRC Handbook of Chemistry and Physics*, Eighty four. CRC Press, 2003, ISBN: 9780849304842.

[68] M. I. Katsnelson, *Graphene: Carbon in Two Dimensions*. Cambridge University Press, 2012, ISBN: 9780521195409.

[69] M. H. Gass, U. Bangert, A. L. Bleloch, P. Wang, R. R. Nair, and A. K. Geim, "Free-standing graphene at atomic resolution", *Nature Nanotechnology*, vol. 3, no. 11, pp. 676–681, 2008.

[70] A. C. Neto, F. Guinea, N. Peres, K. S. Novoselov, and A. K. Geim, "The electronic properties of graphene", *Reviews of Modern Physics*, vol. 81, no. 1, pp. 109–64, 2009.

[71] N. M. R. Peres, "Colloquium: The transport properties of graphene: An introduction", *Reviews of Modern Physics*, vol. 82, no. 4, pp. 2673–2700, Jul. 2010.

[72] P. R. Wallace, "The Band Theory of Graphite", *Physical Review*, vol. 71, no. 9, pp. 622–634, 1947.

[73] M. H. Lee, H. C. Chung, J. M. Lu, C. P. Chang, and M. F. Lin, "Electronic and optical properties in graphane", *Mesoscale and Nanoscale Physics*, vol. 95, no. 24, pp. 1–23, 2014.

[74] S. Reich, J. Maultzsch, C. Thomsen, and P. Ordejon, "Tight-binding description of graphene", *Physical Review B*, vol. 66, no. 3, pp. 035 412–5, 2002.

[75] D. Abergel, V. Apalkov, J. Berashevich, K. Ziegler, and T. Chakraborty, "Properties of graphene: A theoretical perspective", *Advances in Physics*, vol. 59, no. 4, pp. 261–482, 2010.

[76] M. S. A. Bhuyan, M. N. Uddin, M. M. Islam, F. A. Bipasha, and S. S. Hossain, "Synthesis of graphene", *International Nano Letters*, vol. 6, no. 2, pp. 65–83, 2016.

[77] F. Tuinstra and J. L. Koenig, "Raman Spectrum of Graphite", *The Journal of Chemical Physics*, vol. 53, no. 3, pp. 1126–1130, 1970.

[78] K. I. Bolotin, K. J. Sikes, Z. Jiang, M. Klima, G. Fudenberg, J. Hone, P. Kim, and H. L. Stormer, "Ultrahigh electron mobility in suspended graphene", *Solid State Communications*, vol. 146, no. 9, pp. 351–355, 2008.

[79] X. Cui, C. Zhang, R. Hao, and Y. Hou, "Liquid-phase exfoliation, functionalization and applications of graphene", *Nanoscale*, vol. 3, no. 5, pp. 2118–2126, 2011.

[80] N. Behabtu, J. R. Lomeda, M. J. Green, A. L. Higginbotham, A. Sinitskii, D. V. Kosynkin, D. Tsentalovich, A. N. G. Parra-Vasquez, J. Schmidt, E. Kesselman, Y. Cohen, Y. Talmon, J. M. Tour, and M. Pasquali, "Spontaneous high-concentration dispersions and liquid crystals of graphene.", *Nature Nanotechnology*, vol. 5, no. 6, pp. 406–411, 2010.

[81] L. Jiao, L. Zhang, X. Wang, G. Diankov, and H. Dai, "Narrow graphene nanoribbons from carbon nanotubes", *Nature*, vol. 458, no. 7240, pp. 877–880, 2009.

[82] D. V. Kosynkin, A. L. Higginbotham, A. Sinitskii, J. R. Lomeda, A. Dimiev, B. K. Price, and J. M. Tour, "Longitudinal unzipping of carbon nanotubes to form graphene nanoribbons.", *Nature*, vol. 458, no. 7240, pp. 872–876, 2009.

[83] P. Sutter, "Epitaxial graphene: How silicon leaves the scene.", *Nature Materials*, vol. 8, no. 3, pp. 171–172, 2009.

[84] A. J. Van Bommel, J. E. Crombeen, and A. Van Tooren, "LEED and Auger electron observations of the SiC(0001) surface", *Surface Science*, vol. 48, no. 2, pp. 463–472, 1975.

[85] W. A. Heer, C. Berger, M. Ruan, M. Sprinkle, X. Li, Y. Hu, B. Zhang, J. Hankinson, and E. Conrad, "Large area and structured epitaxial graphene produced by confinement controlled sublimation of silicon carbide", *Proceedings of the National Academy of Sciences of the United States of America*, vol. 108, no. 41, pp. 16 900–16 905, 2011.

[86] E. Rollings, G. H. Gweon, S. Y. Zhou, B. S. Mun, J. L. McChesney, B. S. Hussain, A. V. Fedorov, P. N. First, W. A. de Heer, and A. Lanzara, "Synthesis and characterization of atomically thin graphite films on a silicon carbide substrate", *Journal of Physics and Chemistry of Solids*, vol. 67, no. 9, pp. 2172–2177, 2006.

[87] C. Berger, Z. Song, T. Li, X. Li, A. Y. Ogbazghi, R. Feng, Z. Dai, A. N. Marchenkov, E. H. Conrad, P. N. First, and W. A. D. Heer, "Ultrathin Epitaxial Graphite : 2D Electron Gas Properties and a Route Toward Graphene-based Nanoelectronics", *Journal of Physical Chemistry B*, vol. 108, no. 52, pp. 19 912–19 916, 2004.

[88] A. V. Zaretski and D. J. Lipomi, "Processes for non-destructive transfer of graphene: widening the bottleneck for industrial scale production", *Nanoscale*, vol. 7, no. 22, pp. 9963–9969, 2015.

[89] D. Wei, Y. Liu, Y. Wang, H. Zhang, L. Huang, and G. Yu, "Synthesis of N-Doped Graphene by Chemical Vapor Deposition and its Electrical Properties", *Nano Letters*, vol. 9, no. 5, pp. 1752–1758, 2009.

[90] K. S. Kim, Y. Zhao, H. Jang, S. Y. Lee, J. M. Kim, K. S. Kim, J.-H. Ahn, P. Kim, J.-Y. Choi, and B. H. Hong, "Large-scale pattern growth of graphene films for stretchable transparent electrodes.", *Nature*, vol. 457, no. 7230, pp. 706–710, 2009.

[91] S. Y. Kwon, C. V. Ciobanu, V. Petrova, V. B. Shenoy, J. Bareño, V. Gambin, I. Petrov, and S. Kodambaka, "Growth of semiconducting graphene on palladium", *Nano Letters*, vol. 9, no. 12, pp. 3985–3990, 2009.

[92] S. Hofmann, P. Braeuninger-Weimer, and R. S. Weatherup, "CVD-enabled graphene manufacture and technology", *Journal of Physical Chemistry Letters*, vol. 6, no. 14, pp. 2714–2721, 2015.

[93] X. Li, W. Cai, J. An, S. Kim, J. Nah, D. Yang, R. Piner, A. Velamakanni, I. Jung, E. Tutuc, S. K. Banerjee, L. Colombo, and R. S. Ruoff, "Large-Area Synthesis of High-Quality and Uniform Graphene Films on Copper Foils", *Science*, vol. 324, no. 5932, pp. 1312–1314, 2009.

[94] X. Li, W. Cai, L. Colombo, and R. S. Ruoff, "Evolution of Graphene Growth on Ni and Cu by Carbon Isotope Labeling", *Nano Letters*, vol. 12, no. 1, pp. 4268–72, 2009.

[95] X. Li, C. W. Magnuson, A. Venugopal, J. An, J. W. Suk, B. Han, M. Borysiak, W. Cai, A. Velamakanni, Y. Zhu, L. Fu, E. M. Vogel, E. Voelkl, L. Colombo, and R. S. Ruoff, "Graphene films with large domain size by a two-step chemical vapor deposition process", *Nano Letters*, vol. 10, no. 11, pp. 4328–4334, 2010.

[96] J. W. Suk, A. Kitt, M. Carl. W., H. Yufeng, A. Samir, A. Jinho, S. Anna K., G. Bennett B., and R. Rodney S., "Transfer of CVD-Grown Monolayer Graphene Transfer of CVD-Grown Monolayer Graphene onto Arbitrary Substrates", *ACS Nano*, vol. 9, no. 5, pp. 6916–6924, 2011.

[97] X. Li, Y. Zhu, W. Cai, M. Borysiak, B. Han, D. Chen, R. D. Piner, L. Colombo, and R. S. Ruoff, "Transfer of large-area graphene films for high-performance transparent conductive electrodes.", *Nano Letters*, vol. 9, no. 12, pp. 4359–4363, Dec. 2009.

[98] L. Banszerus, M. Schmitz, S. Engels, J. Dauber, M. Oellers, F. Haupt, K. Watanabe, T. Taniguchi, B. Beschoten, and C. Stampfer, "Ultrahigh-mobility graphene devices from chemical vapor deposition on reusable copper", *Science Advances*, vol. 1, no. 6, pp. 1–6, 2015.

[99] F. Wang, Y. Zhang, C. Tian, C. Girit, A. Zettl, M. Crommie, and Y. R. Shen, "Gate-Variable Optical Transitions in Graphene", *Science*, vol. 320, no. 5873, pp. 206–209, 2008.

[100] Z. Li, E. A. Henriksen, Z. Jiang, Z. Hao, M. C. Martin, P. Kim, H. Stormer, and D. N. Basov, "Dirac charge dynamics in graphene by infrared spectroscopy", *Nature Physics*, vol. 4, no. 7, pp. 532–535, 2008.

[101] P. Lorrain, D. Corson, and F. Lorrain, *Electromagnetic fields and waves*, Third. New York, NY: W. H. Freeman and Company, 1988, ISBN: 9780716703310.

[102] W. Williams, *Nuclear and Particle Physics*, Second. Oxford University Press, 1991, ISBN: 0198520468.

[103] R. R. Nair, P Blake, A. N. Grigorenko, K. S. Novoselov, T. J. Booth, T. Stauber, N. M. R. Peres, and A. K. Geim, "Fine structure constant defines visual transparency of graphene.", *Science*, vol. 320, no. 5881, p. 1308, Jun. 2008.

[104] F. Xia, T. Mueller, Y.-m. Lin, A. Valdes-Garcia, and P. Avouris, "Ultrafast graphene photodetector", *Nature Nanotechnology*, vol. 4, no. 12, pp. 839–840, 2009.

[105] F. Bonaccorso, Z. Sun, T. Hasan, and A. Ferrari, "Graphene photonics and optoelectronics", *Nature Photonics*, vol. 4, no. 9, pp. 611–622, Aug. 2010.

[106] R. W. Keyes, "Physical limits of silicon transistors and circuits", *Reports on Progress in Physics*, vol. 68, no. 12, pp. 2701–2746, 2005.

[107] A. K. Geim and K. S. Novoselov, "The rise of graphene", *Nature Materials*, vol. 6, no. 3, pp. 183–191, Mar. 2007.

[108] D. S. Jessop, S. J. Kindness, L. Xiao, P. Braeuninger-Weimer, H. Lin, Y. Ren, C. X. Ren, S. Hofmann, J. A. Zeitler, H. E. Beere, D. A. Ritchie, and R. Degl'Innocenti, "Graphene based plasmonic terahertz amplitude modulator operating above 100 MHz", *Applied Physics Letters*, vol. 108, no. 17, pp. 171 101–5, 2016.

[109] G. Liang, X. Hu, X. Yu, Y. Shen, L. H. Li, A. G. Davies, E. H. Linfield, H. K. Liang, Y. Zhang, S. F. Yu, and Q. J. Wang, "Integrated Terahertz Graphene Modulator with 100% Modulation Depth", *ACS Photonics*, vol. 2, no. 11, pp. 1559–1566, 2015.

[110] W. Gao, J. Shu, K. Reichel, D. V. Nickel, X. He, G. Shi, R. Vajtai, P. M. Ajayan, J. Kono, D. M. Mittleman, and Q. Xu, "High-contrast terahertz wave modulation by gated graphene enhanced by extraordinary transmission through ring apertures", *Nano Letters*, vol. 14, no. 3, pp. 1242–1248, 2014.

[111] S. Koenig, D. Lopez-Diaz, J. Antes, F. Boes, R. Henneberger, A. Leuther, A. Tessmann, R. Schmogrow, D. Hillerkuss, R. Palmer, T. Zwick, C. Koos, W. Freude, O. Ambacher, J. Leuthold, and I. Kallfass, "Wireless sub-THz communication system with high data rate", *Nature Photonics*, vol. 7, no. 12, pp. 977–981, 2013.

[112] A. C. Ferrari, J. C. Meyer, V. Scardaci, C. Casiraghi, M. Lazzeri, F. Mauri, S. Piscanec, D. Jiang, K. S. Novoselov, S. Roth, and A. K. Geim, "Raman Spectrum of Graphene and Graphene Layers", *Physical Review Letters*, vol. 97, no. 18, pp. 187 401–4, Oct. 2006.

[113] N. W. Ashcroft and N. D. Mermin, *Solid State Physics*. Brooks/Cole, 1976, ISBN: 9780030839931.

[114] G. W. Hanson, "Dyadic Greens functions and guided surface waves for a surface conductivity model of graphene", *Journal of Applied Physics*, vol. 103, no. 6, pp. 064 302–064 319, 2008.

[115] G. W. Hanson, "Quasi-transverse electromagnetic modes supported by a graphene parallel-plate waveguide", *Journal of Applied Physics*, vol. 104, no. 8, pp. 084 314–084 314, 2008.

[116] X. Luo, T. Qiu, W. Lu, and Z. Ni, "Plasmons in graphene: Recent progress and applications", *Materials Science and Engineering: R: Reports*, vol. 74, no. 11, 2013.

[117] V. P. Gusynin, S. G. Sharapov, and J. P. Carbotte, "On the universal ac optical background in graphene", *New Journal of Physics*, vol. 11, no. 9, pp. 095 013–095 019, 2009.

[118] T. Stauber, N. M. R. Peres, and A. K. Geim, "The optical conductivity of graphene in the visible region of the spectrum", *Physical Review B*, vol. 78, no. 8, pp. 085 432–9, Mar. 2008.

[119] S. D. Sarma, S. Adam, E. Hwang, and E. Rossi, "Electronic transport in two dimensional graphene", *Reviews of Modern Physics*, vol. 83, no. 2, pp. 407–475, 2011.

[120] G. Paulo Andre Dias and N. M. Peres, *An Introduction to Graphene Plasmonics*, First. World Scientific, 2016, ISBN: 978-981-4749-98-5.

[121] L. A. Falkovsky, "Optical properties of graphene", *Journal of Physics: Conference Series*, vol. 129, no. 1, pp. 1–7, Oct. 2008.

[122] H. S. Song, S. L. Li, H. Miyazaki, S. Sato, K. Hayashi, A. Yamada, N. Yokoyama, and K. Tsukagoshi, "Origin of the relatively low transport mobility of graphene grown through chemical vapor deposition.", *Scientific Reports*, vol. 27, no. 337, pp. 1–5, 2012.

[123] L. A. Falkovsky and A. A. Varlamov, "Space-time dispersion of graphene conductivity", *The European Physical Journal B*, vol. 56, no. 4, pp. 281–284, Jun. 2007.

[124] L. A. Falkovsky and S. Pershoguba, "Optical far-infrared properties of a graphene monolayer and multilayer", *Physical Review B*, vol. 76, no. 15, pp. 153 410–4, Oct. 2007.

[125] N. M. R. Peres, J. M. B. Lopes Dos Santos, and T. Stauber, "Phenomenological study of the electronic transport coefficients of graphene", *Physical Review B*, vol. 76, no. 7, pp. 073 412–6, 2007.

[126] T. Stauber, N. M. Peres, and F. Guinea, "Electronic transport in graphene: A semiclassical approach including midgap states", *Physical Review B*, vol. 76, no. 20, pp. 205 423–33, 2007.

[127] J. Horng, C.-F. Chen, B. Geng, C. Girit, Y. Zhang, Z. Hao, H. A. Bechtel, M. Martin, A. Zettl, M. F. Crommie, and Y. Shen, "Drude conductivity of Dirac fermions in graphene", *Physical Review B*, vol. 83, no. 16, pp. 165 113–5, 2011.

[128] W. Gao, G. Shi, Z. Jin, J. Shu, Q. Zhang, R. Vajtai, P. M. Ajayan, J. Kono, and Q. Xu, "Excitation and active control of propagating surface plasmon polaritons in graphene.", *Nano Letters*, vol. 13, no. 8, pp. 3698–702, Aug. 2013.

[129] J. E. Lee, G. Ahn, J. Shim, Y. S. Lee, and S. Ryu, "Optical separation of mechanical strain from charge doping in graphene", *Nature Communications*, vol. 3, no. May, pp. 1024–1031, 2012.

[130] E. Alexeev, J. Moger, and E. Hendry, "Photo-induced doping and strain in exfoliated graphene", *Applied Physics Letters*, vol. 103, no. 15, pp. 151 907–151 910, 2013.

[131] M. Jablan, H. Buljan, and M. Soljačić, "Plasmonics in graphene at infrared frequencies", *Physical Review B*, vol. 80, no. 24, pp. 245 435–7, Dec. 2009.

[132] X. Zhang and J. Xu, *Introduction to THz Wave Photonics*. Springer, 2010, ISBN: 978 1441909787.

[133] M. Tonouchi, "Cutting-edge terahertz technology", *Nature Photonics*, vol. 1, no. 2, pp. 97–105, 2007.

[134] D. E. Aznakayeva, F. J. Rodriguez, O. P. Marshall, and A. N. Grigorenko, "Graphene light modulators working at near-infrared wavelengths", *Optics Express*, vol. 25, no. 9, pp. 10 255–10 260, 2017.

[135] D. C. Fernandez, R. Bhargava, S. M. Hewitt, and I. W. Levin, "Infrared spectroscopic imaging for histopathologic recognition.", *Nature Biotechnology*, vol. 23, no. 4, pp. 469–474, 2005.

[136] C. Bauer, P. Geiser, J. Burgmeier, G. Holl, and W. Schade, "Pulsed laser surface fragmentation and mid-infrared laser spectroscopy for remote detection of explosives", *Applied Physics B*, vol. 85, no. 2, pp. 251–256, 2006.

[137] D. B. Farmer, D. Rodrigo, T. Low, and P. Avouris, "Plasmon–Plasmon Hybridization and Bandwidth Enhancement in Nanostructured Graphene", *Nano Letters*, vol. 15, no. 4, pp. 2582–2587, 2015.

[138] S. A. Carr, M. J. Huddleston, and R. S. Annan, "Selective Detection and Sequencing of Phosphopeptides at the Femtomole Level by Mass Spectrometry 1", *Analytical Biochemistry*, vol. 239, no. 2, pp. 180–192, 1996.

[139] T. Nishijima, M. Koshioka, and H. Yamazaki, "A highly-sensitive rice seedling bioassay for the detection of femtomole quantities of 3β-hydroxylated gibberellins", *Plant Growth Regulation*, vol. 13, no. 3, pp. 241–247, 1993.

[140] D. Rodrigo, O. Limaj, D. Janner, D. Etezadi, F. J. Garcia de Abajo, V. Pruneri, and H. Altug, "Mid-infrared plasmonic biosensing with graphene", *Science*, vol. 349, no. 6244, pp. 165–168, 2015.

[141] Y. Li, H. Yan, D. B. Farmer, X. Meng, W. Zhu, R. M. Osgood, T. F. Heinz, and P. Avouris, "Graphene plasmon enhanced vibrational sensing of surface-adsorbed layers", *Nano Letters*, vol. 14, no. 3, p. 1573, 2014.

[142] J. Chen, M. Badioli, P. Alonso-González, S. Thongrattanasiri, F. Huth, J. Osmond, M. Spasenovi, A. Centeno, P. Godignon, A. Zurutuza, N. Camara, J. G. De, R. Hillenbrand, and F. Koppens, "Optical nano-imaging of gate-tuneable graphene plasmons", *Nature*, vol. 487, no. 7405, pp. 77–81, 2012.

[143] Z. Fei, A. S. Rodin, G. O Andreev, W. Bao, A. S. McLeod, M. Wagner, L. M. Zhang, Z. Zhao, M. Thiemens, G. Dominguez, M. M. Fogler, A. H. Castro Neto, C. N. Lau, F. Keilmann, and D. N. Basov, "Gate-tuning of graphene plasmons revealed by infrared nano-imaging.", *Nature*, vol. 487, no. 7405, pp. 82–85, Jul. 2012.

[144] H. Buljan, M. Jablan, and M. Soljačić, "Damping of plasmons in graphene", *Nature Photonics*, vol. 7, no. May, pp. 1–3, 2013.

[145] H. Yan, T. Low, W. Zhu, Y. Wu, M. Freitag, X. Li, F. Guinea, P. Avouris, and F. Xia, "Damping pathways of mid-infrared plasmons in graphene nanostructures", *Nature Photonics*, vol. 7, no. 5, pp. 394–399, Apr. 2013.

[146] M. Gullans, D. E. Chang, F. H. L. Koppens, F. J. G. de Abajo, and M. D. Lukin, "Single-photon nonlinear optics with graphene plasmons", *Physical Review Letters*, vol. 111, no. 24, pp. 247 401–5, Sep. 2013.

[147] A. Principi, G. Vignale, M. Carrega, and M. Polini, "Intrinsic lifetime of Dirac plasmons in graphene", *Physical Review B*, vol. 88, no. 19, pp. 195 405–15, 2013.

[148] L. Ju, B. Geng, J. Horng, C. Girit, M. Martin, Z. Hao, H. Bechtel, X. Liang, A. Zettl, Y. Shen, and F. Wang, "Graphene plasmonics for tunable terahertz metamaterials", *Nature Nanotechnology*, vol. 6, no. 10, pp. 630–634, Oct. 2011.

[149] S. Thongrattanasiri, F. H. L. Koppens, and F. J. G. de Abajo, "Total light absorption in graphene", *Physical Review Letters*, vol. 108, no. 4, pp. 047 401–5, Jun. 2011.

[150] S. Thongrattanasiri, F. H. L. Koppens, and F. J. García de Abajo, "Complete Optical Absorption in Periodically Patterned Graphene", *Physical Review Letters*, vol. 108, no. 4, pp. 047 401–10, Jan. 2012.

[151] F. Ramirez, B. Liu, and S. Shen, "Extreme blueshift of surface plasmon resonance frequency in graphene nanodisk stacks", *Journal of Quantitative Spectroscopy and Radiative Transfer*, vol. 158, no. June, pp. 27–35, 2015.

[152] A. Y. Nikitin, F. Guinea, and L. Martin-Moreno, "Resonant plasmonic effects in periodic graphene antidot arrays", *Applied Physics Letters*, vol. 101, no. 15, pp. 151 119–4, 2012.

[153] W. Zhu, I. D. Rukhlenko, and M. Premaratne, "Graphene metamaterial for optical reflection modulation", *Applied Physics Letters*, vol. 102, no. 24, 2013.

[154] Y. Cui and C. Zeng, "Efficient modulation of orthogonally polarized infrared light using graphene metamaterials", *Journal of Applied Physics*, vol. 121, no. 14, pp. 143 102–6, 2017.

[155] H. Yan, F. Xia, Z. Li, and P. Avouris, "Plasmonics of coupled graphene microstructures", *New Journal of Physics*, vol. 14, no. 12, pp. 125 001–20, Dec. 2012.

[156] R. Alaee, M. Farhat, C. Rockstuhl, and F. Lederer, "A perfect absorber made of a graphene micro-ribbon metamaterial.", *Optics Express*, vol. 20, no. 27, pp. 28 017–24, 2012.

[157] I.-T. Lin and J.-M. Liu, "Enhanced graphene plasmon waveguiding in a layered graphene -metal structure", *Applied Physics Letters*, vol. 105, no. 1, pp. 011 604–5, Jul. 2014.

[158] P.-Y. Chen and A. Alu, "Atomically Thin Surface Cloak Using Graphene Monolayers", *ACS Nano*, vol. 5, no. 7, pp. 5855–5863, 2011.

[159] A. Vakil and N. Engheta, "Transformation optics using graphene", *Science*, vol. 332, no. 6035, pp. 1291–1294, 2011.

[160] A. Vakil, "Fourier Optics on Graphene Fourier Optics on Graphene", *Physical Review B*, vol. 85, no. February, 2012.

[161] X. Wu and X. Guo, "Terahertz electromagnetic fences on a graphene surface plasmon polariton platform", *Scientific Reports*, vol. 7, no. 1, pp. 2899–10, 2017.

[162] S. AbdollahRamezani, K. Arik, S. Farajollahi, A. Khavasi, and Z. Kavehvash, "Beam manipulating by gate-tunable graphene- based metasurfaces", *Optics Letters*, vol. 40, no. 22, pp. 5383–5386, 2015.

[163] E. Lim, M. Fejer, R. Byer, and W. Kozlovsky, "Blue light generation by frequency doubling in periodically poled lithium niobate channel waveguide", *Electronics Letters*, vol. 25, no. 11, pp. 731–732, 1989.

[164] G. New, *Introduction to Nonlinear Optics*. Cambridge University Press, 2011, ISBN: 9780521877015.

[165] R. A. Fisher, P. L. Kelley, and T. K. Gustafson, "Subpicosecond pulse generation using the optical Kerr effect", *Applied Physics Letters*, vol. 14, no. 4, pp. 140–143, 1969.

[166] R. R. Alfano and S. L. Shapiro, "Observation of self-phase modulation and small-scale filaments in crystals and glasses", *Physical Review Letters*, vol. 24, no. 11, pp. 592–594, 1970.

[167] J. Kerr, "A new relation between electricity and light: Dielectrified media birefringent", *Philosophical Magazine Series 4*, vol. 50, no. 333, pp. 337–348, 1875.

[168] P. A. Franken, A. E. Hill, C. W. Peters, and G. Weinreich, "Generation of optical harmonics", *Physical Review Letters*, vol. 7, no. 4, pp. 118–119, 1961.

[169] Robert Boyd; *Nonlinear Optics*, Third. Taylor & Francis, 1992, ISBN: 978-8-57-811079-6.

[170] P. A. Franken and J. F. Ward, "Optical harmonics and nonlinear phenomena", *Reviews of Modern Physics*, vol. 35, no. 1, pp. 23–39, 1963.

[171] H. J. Bakker, P. C. Planken, L. Kuipers, and A Lagendijk, "Phase modulation in second-order nonlinear-optical processes", *Physical Review A*, vol. 42, no. 7, pp. 4085–4101, 1990.

[172] X. Liu, L. Qian, and F. Wise, "Generation of Optical Spatiotemporal Solitons", *Physical Review Letters*, vol. 82, no. 23, pp. 4631–4634, 1999.

[173] P. F. Curley, A. I. Ferguson, J. G. White, and W. B. Amos, "Application of a femtosecond self-sustaining mode-locked Ti:sapphire laser to the field of laser scanning confocal microscopy", *Optical and Quantum Electronics*, vol. 24, no. 8, pp. 851–859, 1992.

[174] P. J. Campagnola, M. D. Wei, A Lewis, and L. M. Loew, "High-resolution nonlinear optical imaging of live cells by second harmonic generation.", *Biophysical Journal*, vol. 77, no. 6, pp. 3341–9, 1999.

[175] R. Baumgartner and R. Byer, "Optical parametric amplification", *Quantum Electronics, IEEE Journal of*, vol. 15, no. 6, pp. 432–444, 1979.

[176] R. Lytel, S. M. Mossman, and M. G. Kuzyk, "General solution to nonlinear optical quantum graphs using Dalgarno-Lewis summation techniques", *Journal of the Optical Society of America B*, vol. 33, no. 12, E14, 2016.

[177] J. Perez-Moreno, S. Shafei, and M. G. Kuzyk, "Applying universal scaling laws to identify the best molecular design paradigms for second-order nonlinear optics", *Journal of the Optical Society of America B*, vol. 33, no. 12, E45, 2016.

[178] P. D. Maker, R. W. Terhune, M. Nisenoff, and C. M. Savage, "Effects of Dispersion and Focusing on the Production of Optical Harmonics", *Physical Review B*, vol. 8, no. 1, pp. 21–22, 1962.

[179] S. A. Mikhailov, "Quantum theory of third-harmonic generation in graphene", *Physical Review B*, vol. 90, no. 24, pp. 241 301–4, 2014.

[180] S. A. Mikhailov, "Quantum theory of the third-order nonlinear electrodynamic effects of graphene", *Physical Review B*, vol. 93, no. 8, pp. 1–29, 2016.

[181] E. Hendry, P. Hale, J. Moger, A. Savchenko, and S. Mikhailov, "Coherent nonlinear optical response of graphene", *Physical Review Letters*, vol. 105, no. 9, pp. 097 401–4, 2010.

[182] Z. Liu, Y. Wang, X. Zhang, Y. Xu, Y. Chen, and J. Tian, "Nonlinear optical properties of graphene oxide in nanosecond and picosecond regimes", *Applied Physics Letters*, vol. 94, no. 2, pp. 1–4, 2009.

[183] T. Gu, N. Petrone, J. F. McMillan, A. van der Zande, M. Yu, G.-Q. Lo, D.-L. Kwong, J. Hone, and C. W. Wong, "Regenerative oscillation and four-wave mixing in graphene optoelectronics", *Nature Photonics*, vol. 6, no. 8, pp. 554–559, 2012.

[184] A. J. DeMaria, D. A. Stetser, and H. Heynau, "Self Mode-Locking of Lasers With Saturable Absorbers", *Applied Physics Letters*, vol. 8, no. 7, pp. 174–176, 1966.

[185] C. P. Christensen, W. Braverman, W. H. Steier, and C. Wittig, "Active mode locking of the XeF laser", *Applied Physics Letters*, vol. 29, no. 7, pp. 424–5, 1976.

[186] U. Keller, K. J. Weingarten, F. X. Kärtner, D. Kopf, B. Braun, I. D. Jung, R. Fluck, C. Hönninger, N. Matuschek, and J. Aus Der Au, "Semiconductor saturable absorber mirrors (SESAM's) for femtosecond to nanosecond pulse generation in solid-state lasers", *IEEE Journal on Selected Topics in Quantum Electronics*, vol. 2, no. 3, pp. 435–451, 1996.

[187] Z. P. Sun, T. Hasan, F. Torrisi, D. Popa, G. Privitera, F. Q. Wang, F. Bonaccorso, D. M. Basko, and A. C. Ferrari, "Graphene Mode-Locked Ultrafast Laser", *ACS Nano*, vol. 4, no. 2, pp. 803–810, 2010.

[188] H. Zhang, D. Y. Tang, L. M. Zhao, Q. L. Bao, and K. P. Loh, "Large energy mode locking of an erbium-doped fiber laser with an atomic layer graphene", *Advanced Functional Materials*, vol. 17, no. 20, pp. 17 630–5, 2009.

[189] G. Q. Xie, J. Ma, P. Lv, W. L. Gao, P. Yuan, L. J. Qian, H. H. Yu, H. J. Zhang, J. Y. Wang, and D. Y. Tang, "Graphene saturable absorber for Q-switching and mode locking at 2 μm wavelength", *Optical Materials Express*, vol. 2, no. 6, pp. 878–883, 2012.

[190] H. Zhang, D. Tang, R. J. Knize, L. Zhao, Q. Bao, and K. P. Loh, "Graphene mode locked, wavelength-tunable, dissipative soliton fiber laser", *Applied Physics Letters*, vol. 96, no. 11, pp. 111 112–3, 2010.

[191] R. Hellwarth, "Third Order Optical Susceptibilities of Liquids and Solids.", *Progress in Quantum Electronics*, vol. 5, p. 1, 1977.

[192] S. A. Mikhailov, "Non-linear electromagnetic response of graphene", *Europhysics Letters*, vol. 79, no. 2, p. 27 002, Jul. 2007.

[193] R. Kumar, A. Sharma, M. Bhatnagar, B. Mehta, and S. Rath, "Antireflection properties of graphene layers on planar and textured silicon surfaces", *Nanotechnology*, vol. 24, no. 16, pp. 165 402–8, 2013.

[194] Z. Zhang and P. L. Voss, "Full-band quantum-dynamical theory of saturation and four-wave mixing in graphene", *Optics Letters*, vol. 36, no. 23, pp. 4569–4571, 2011.

[195] J. L. Cheng, N. Vermeulen, and J. E. Sipe, "Third order optical nonlinearity of graphene", *New Journal of Physics*, vol. 16, no. 5, pp. 053 014–16, 2014.

[196] N. A. Savostianova and S. A. Mikhailov, "Giant enhancement of the third harmonic in graphene integrated in a layered structure", *Applied Physics Letters*, vol. 107, no. 18, pp. 181 104–4, 2015.

[197] T. J. Constant, S. M. Hornett, D. E. Chang, and E. Hendry, "All-optical generation of surface plasmons in graphene", *Nature Physics*, vol. 12, no. 2, pp. 124–127, 2015.

[198] M. Muyskens, "The Fluorescence of Lignum nephriticum: A Flash Back to the Past and a Simple Demonstration of Natural Substance Fluorescence", *Journal of Chemical Education*, vol. 83, no. 5, pp. 765–768, 2006.

[199] D. Stoner-Ma, A. A. Jaye, P. Matousek, M. Towrie, S. R. Meech, and P. J. Tonge, "Observation of excited-state proton transfer in green fluorescent protein using ultrafast vibrational spectroscopy", *Journal of the American Chemical Society*, vol. 127, no. 9, pp. 2864–2865, 2005.

[200] J. W. Lichtman and J.-A. Conchello, "Fluorescence microscopy", *Nature Methods*, vol. 2, no. 12, pp. 910–919, 2005.

[201] S. J. Strickler and R. A. Berg, "Relationship between Absorption Intensity and Fluorescence Lifetime of Molecules", *The Journal of Chemical Physics*, vol. 37, no. 4, pp. 814–822, 1962.

[202] Z. W. Mikrosk, "The use of a vertical illuminator with interchangeable dichroic mirrors for fluorescence microscopy with incident light.", *Ploem, J. S.*, vol. 68, no. 3, pp. 129–142, 1967.

[203] J. E. Hobbie, R. J. Daley, and S. Jasper, "Use of nuclepore filter counting bacteria by fluoroscence microscopy", *Applied and Environmental Microbiology*, vol. 33, no. May, pp. 1225–1228, 1977.

[204] J. B. Pawley and B. R. Masters, *Handbook of Biological Confocal Microscopy*, Third, J. Pawley, Ed. Springer US, 2006, ISBN: 9780387455242.

[205] C. Vorndran, A. Minta, and M. Poenie, "New fluorescent calcium indicators designed for cytosolic retention or measuring calcium near membranes.", *Biophysical Journal*, vol. 69, no. 5, pp. 2112–24, 1995.

[206] M. Chalfie, Y. Tu, G. Euskirchen, W. Ward, and D. Prasher, "Green fluorescent protein as a marker for gene expression", *Science*, vol. 263, no. 5148, pp. 802–805, 1994.

[207] S. Paddock, "Over the rainbow: 25 Years of confocal imaging", *BioTechniques*, vol. 44, no. 5, pp. 643–648, 2008.

[208] W. Denk, J. H. Strickler, and W. W. Webb, "Two-Photon Laser Scanning Fluorescence Microscopy", *Science*, vol. 248, no. 4951, pp. 73–76, 1990.

[209] S. M. Mansfield and G. S. Kino, "Solid immersion microscope", *Applied Physics Letters*, vol. 57, no. 24, pp. 2615–2616, 1990.

[210] J.-X. Cheng, Y. K. Jia, G. Zheng, and X. S. Xie, "Laser-Scanning Coherent Anti-Stokes Raman Scattering Microscopy and Applications to Cell Biology", *Biophysical Journal*, vol. 83, no. 1, pp. 502–509, 2002.

[211] M. Yuratich and D. Hanna, "Coherent anti-Stokes Raman spectroscopy (CARS)", vol. 33, no. 3, pp. 671–682, 1977.

[212] R. J. Stöhr, R. Kolesov, J. Pflaum, and J. Wrachtrup, "Fluorescence of laser-created electron-hole plasma in graphene", *Physical Review B*, vol. 82, no. 12, pp. 121 408–4, 2010.

[213] P. Y. Yu and M. Cardona, *Fundamentals of semiconductors*, Fourth. Springer, 2010, ISBN: 9783642007101.

[214] N. Wada, S. Yoshimi, S. Sakai, C. L. Shao, and M. Fukui, "Stable Operation of AlGaAs / GaAs Light-Emitting Diodes Fabricated on Si Substrate", *Journal of Applied Physics*, vol. 31, no. 2A, pp. 78–81, 1991.

[215] G. W. 'T Hooft, W. A.J. A. Van Der Poel, L. W. Molenkamp, and C. T. Foxon, "Near-band-gap luminescence from a GaAs-AlGaAs interface", *Applied Physics Letters*, vol. 50, no. 19, pp. 1388–1390, 1987.

[216] D. Olego and M. Cardona, "Photoluminescence in heavily doped GaAs. I. Temperature and hole-concentration dependence", *Physical Review B*, vol. 22, no. 2, pp. 886–893, 1980.

[217] J. Liqiang, Q. Yichun, W. Baiqi, L. Shudan, J. Baojiang, Y. Libin, F. Wei, F. Honggang, and S. Jiazhong, "Review of photoluminescence performance of nano-sized semiconductor materials and its relationships with photocatalytic activity", *Solar Energy Materials and Solar Cells*, vol. 90, no. 12, pp. 1773–1787, 2006.

[218] K. F. Mak, L. Ju, F. Wang, and T. F. Heinz, "Optical spectroscopy of graphene: From the far infrared to the ultraviolet", *Solid State Communications*, vol. 152, no. 15, pp. 1341–1349, Aug. 2012.

[219] E. H. Hwang, B. Y.-K. Hu, and S. D. Sarma, "Inelastic carrier lifetime in graphene", *Physical Review B*, vol. 76, no. 11, pp. 115 434–6, 2007.

[220] W. Tse, E. Hwang, and S. D. Sarma, "Ballistic hot electron transport in graphene", *Applied Physics Letters*, vol. 023128, no. 2, pp. 2–5, 2008.

[221] C. H. Lui, K. F. Mak, J. Shan, and T. F. Heinz, "Ultrafast photoluminescence from graphene", *Physical Review Letters*, vol. 105, no. 12, pp. 1–4, 2010.

[222] D. Brida, A. Tomadin, C. Manzoni, Y. J. Kim, A. Lombardo, S. Milana, R. R. Nair, K. S. Novoselov, A. C. Ferrari, G. Cerullo, and M. Polini, "Ultrafast collinear scattering and carrier multiplication in graphene", *Nature Communications*, vol. 4, no. May, pp. 1–9, 2013.

[223] E. Purcell, H. Torrey, and R. Pound, "Resonance Absorption by Nuclear Magnetic Moments in a Solid", *Physical Review*, vol. 69, no. 1-2, pp. 37–38, 1946.

[224] D. Kleppner, "Inhibited spontaneous emission", *Physical Review Letters*, vol. 47, no. 4, pp. 233–236, 1981.

[225] P. Goy, J. M. Raimond, M. Gross, and S. Haroche, "Observation of cavity-enhanced single-atom spontaneous emission", *Physical Review Letters*, vol. 50, no. 24, pp. 1903–1906, 1983.

[226] L. Stryer, "Fluorescence Energy Transfer as a Spectroscopic Ruler", *Annual Review of Biochemistry*, vol. 47, no. 1, pp. 819–846, 1978.

[227] E. Dulkeith, A. C. Morteani, T. Niedereichholz, T. A. Klar, J. Feldmann, S. A. Levi, F. C.J. M. van Veggel, D. N. Reinhoudt, M. Möller, and D. I. Gittins, "Fluorescence quenching of dye molecules near gold nanoparticles: radiative and nonradiative effects.", *Physical Review Letters*, vol. 89, no. 20, pp. 203 002–4, 2002.

[228] P. Andrew and W. L. Barnes, "Förster Energy Transfer in an Optical Microcavity", *Science*, vol. 290, no. 5492, pp. 785–788, 2000.

[229] M. Fleischmann, P. Hendra, and A. McQuillan, "Raman spectra of pyridine adsorbed a silver electrode", *Chemical Physics Letters*, vol. 26, no. 2, pp. 163–166, 1974.

[230] K. Kneipp, Y. Wang, H. Kneipp, L. T. Perelman, and I. Itzkan, "Single molecule detection using surface-enhanced Raman scattering (SERS)", *Physical Review Letters*, vol. 78, no. 9, pp. 1667–1670, 1997.

[231] S. Nie and S. Emory, "Probing Single Molecules and Single Nanoparticles by Surface-Enhanced Raman Scattering", *Science*, vol. 275, no. February, pp. 1102–1106, 1997.

[232] A. Otto, I. Mrozek, H. Grabhorn, and W. Akemann, "Surface-enhanced Raman scattering", *Journal of Physics: Condensed Matter*, vol. 4, no. 5, pp. 1143–1212, 1992.

[233] H. Metiu, "Surface enhanced spectroscopy", *Progress in Surface Science*, vol. 17, no. 3, pp. 153–320, 1984.

[234] J. Kim, L. J. Cote, F. Kim, and J. Huang, "Visualizing graphene based sheets by fluorescence quenching microscopy", *Journal of the American Chemical Society*, vol. 132, no. 1, pp. 260–267, 2010.

[235] E. Treossi, M. Melucci, A. Liscio, M. Gazzano, P. Samorì, and V. Palermo, "High-contrast visualization of graphene oxide on dye-sensitized glass, quartz, and silicon by fluorescence quenching", *Journal of the American Chemical Society*, vol. 131, no. 43, pp. 15 576–15 577, 2009.

[236] G. Gómez-Santos and T. Stauber, "Fluorescence quenching in graphene: A fundamental ruler and evidence for transverse plasmons", *Physical Review B*, vol. 84, no. 16, pp. 165 438–6, 2011.

[237] L. Gaudreau, K. J. Kielrooij, G. E.D. K. Prawiroatmodjo, J. Osmond, F. J. G. de Abajo, and F. H. L. Koppens, "Universal Distance-Scaling of Non-radiative Energy Transfer to Graphene", *Nano Letters*, vol. 13, no. 5, pp. 2030–3035, 2013.

[238] F. Federspiel, G. Froehlicher, M. Nasilowski, S. Pedetti, A. Mahmood, B. Doudin, S. Park, J. O. Lee, D. Halley, B. Dubertret, P. Gilliot, and S. Berciaud, "Distance dependence of the energy transfer rate from a single semiconductor nanostructure to graphene", *Nano Letters*, vol. 15, no. 2, pp. 1252–1258, 2015.

[239] A. Kasry, A. A. Ardakani, G. S. Tulevski, B. Menges, M. Copel, and L. Vyklicky, "Highly efficient fluorescence quenching with graphene", *Journal of Physical Chemistry C*, vol. 116, no. 4, pp. 2858–2862, 2012.

[240] R. S. Swathi and K. L. Sebastian, "Resonance energy transfer from a dye molecule to graphene", *Journal of Chemical Physics*, vol. 129, no. 5, pp. 054 703–9, 2008.

[241] R. S. Swathi and K. L. Sebastian, "Long range resonance energy transfer from a dye molecule to graphene has $(\mathrm{distance})^{-4}$ dependence", *Journal of Chemical Physics*, vol. 130, no. 8, pp. 086 101–3, 2009.

[242] A. Reserbat-Plantey, K. G. Schädler, L. Gaudreau, G. Navickaite, J. Güttinger, D. Chang, C. Toninelli, A. Bachtold, and F. H. L. Koppens, "Electromechanical control of nitrogen-vacancy defect emission using graphene NEMS", *Nature Communications*, vol. 7, no. January, pp. 10 218–6, 2016.

[243] H. Gonçalves, C. Bernardo, C. Moura, R. A. S. Ferreira, P. S. André, T. Stauber, M. Belsley, and P. Schellenberg, "Long range energy transfer in graphene hybrid structures", *Journal of Physics D*, vol. 49, no. 31, pp. 315 102–6, 2016.

[244] A. Raja, A. Montoya-Castillo, J. Zultak, X. X. Zhang, Z. Ye, C. Roquelet, D. A. Chenet, A. M. Van Der Zande, P. Huang, S. Jockusch, J. Hone, D. R. Reichman, L. E. Brus, and T. F. Heinz, "Energy Transfer from Quantum Dots to Graphene and MoS_2 : The Role of Absorption and Screening in Two-Dimensional Materials", *Nano Letters*, vol. 16, no. 4, pp. 2328–2333, 2016.

[245] K. J. Tielrooij, L. Orona, A. Ferrier, M. Badioli, G. Navickaite, S. Coop, S. Nanot, B. Kalinic, T. Cesca, L. Gaudreau, Q. Ma, A. Centeno, A. Pesquera, A. Zurutuza, H. de Riedmatten, P. Goldner, F. J. García de Abajo, P. Jarillo-Herrero, and F. H. L. Koppens, "Electrical control of optical emitter relaxation pathways enabled by graphene", *Nature Physics*, vol. 11, no. 3, pp. 281–287, 2015.

[246] J. Lee, M. J. Panzer, Y. He, T. P. Lodge, and C. D. Frisbie, "Ion gel gated polymer thin-film transistors", *Journal of the American Chemical Society*, vol. 129, no. 15, pp. 4532–4533, 2007.

[247] O. Salihoglu, N. Kakenov, O. Balci, S. Balci, and C. Kocabas, "Graphene as a Reversible and Spectrally Selective Fluorescence Quencher", *Nature Publishing Group*, vol. 6, no. Sept, pp. 33 911–6, 2016.

[248] W. Gao, J. Shu, C. Qiu, and Q. Xu, "Excitation of plasmonic waves in graphene by guided-mode resonances", *ACS Nano*, vol. 6, no. 9, pp. 7806–7813, Sep. 2012.

[249] P. Sessi, J. R. Guest, M. Bode, and N. P. Guisinger, "Patterning graphene at the nanometer scale via hydrogen desorption", *Nano Letters*, vol. 9, no. 12, pp. 4343–4347, 2009.

[250] T. Buffeteau, J. Grondin, Y. Danten, J.-c. Lasse, and J. C. Lassègues, "Imidazolium-Based Ionic Liquids : Quantitative Aspects in the Far-Infrared Region", *Journal of Physical Chemistry B*, vol. 114, no. 22, pp. 7587–7592, 2010.

[251] R. D. Shannon, "Refractive Index and Dispersion of Fluorides and Oxides", *Journal of Physical and Chemical Reference Data*, vol. 31, no. 4, p. 931, 2002.

[252] MATLAB, *version 8.3.0.532 (R2014a)*, Natick, Massachusetts, 2014.

[253] Lumerical Solutions Inc., *Http://www.lumerical.com/tcad-products/fdtd/*, 2016.

[254] A. Taflove and S. Hagness, *Computational Electrodynamics: The Finite-Difference Time-Domain Method*, Second. Artech House, 2000, ISBN: 9781580538329.

[255] K. Yee, "Numerical solution of initial boundary value problems involving Maxwell's equations in isotropic media", *IEEE Transactions on Antennas and Propagation*, vol. 14, no. 3, pp. 302–307, 1966.

[256] S. D. Gedney, *Introduction to the Finite-Difference Time-Domain (FDTD) Method for Electromagnetics*, 1. Jan. 2011, vol. 6, ISBN: 9781608455225.

[257] J. P. Berenger, "A perfectly matched layer for the absorption of electromagnetic waves", *Journal Computational Physics*, vol. 114, no. 2, pp. 185–200, 1994.

[258] R. Courant, F. Kurt, and H. Lewy, "On the partial difference equations of mathematical physics", *Scientific Reports*, vol. 11, no. 2, pp. 32–74, 1959.

[259] E. D. Palik, *Handbook of optical constants of solids*. Academic press, 1998, ISBN: 978012-5444156.

[260] J. Weber, V. Calado, and M. Van de Sanden, "Optical constants of graphene measured by spectroscopic ellipsometry", *Applied Physics Letters*, vol. 97, no. 9, pp. 091 904–3, 2010.

[261] E. Şaşioğlu, H. Hadipour, C. Friedrich, S. Blügel, and I. Mertig, "Strength of effective Coulomb interactions and origin of ferromagnetism in hydrogenated graphene", *Physical Review B*, vol. 95, no. 6, pp. 3–6, 2017.

[262] A. Das, S. Pisana, B. Chakraborty, S. Piscanec, S. K. Saha, U. V. Waghmare, K. S. Novoselov, H. R. Krishnamurthy, A. K. Geim, A. C. Ferrari, and A. K. Sood, "Monitoring dopants by Raman scattering in an electrochemically top-gated graphene transistor.", *Nature Nanotechnology*, vol. 3, no. 4, pp. 210–15, Apr. 2008.

[263] L. Ju, J. Velasco, E. Huang, S. Kahn, C. Nosiglia, H.-Z. Tsai, W. Yang, T. Taniguchi, K. Watanabe, Y. Zhang, G. Zhang, M. Crommie, A. Zettl, and F. Wang, "Photoinduced doping in heterostructures of graphene and boron nitride.", *Nature Nanotechnology*, vol. 9, no. 5, pp. 348–52, 2014.

[264] Microchem, *Http://microchem.com/products/*, 2017.

[265] K. S. Novoselov, V. I. Fal'ko, L. Colombo, P. R. Gellert, M. G. Schwab, and K. Kim, "A roadmap for graphene", *Nature*, vol. 490, no. 7419, pp. 192–200, 2012.

[266] Y. Zhong, Z. Zhen, and H. Zhu, "Graphene: fundamental research and potential applications", *FlatChem*, vol. 4, no. August, pp. 20–32, 2017.

[267] S. Bae, H. K. Kim, Y. Lee, X. Xu, J.-S. Park, Y. Zheng, J. Balakrishnan, D. Im, T. Lei, Y. I. Song, Y. J. Kim, K. S. Kim, B. Özyilmaz, J.-H. Ahn, B. H. Hong, and S. Iijima, "Roll-to-roll production of 30 inch graphene films for transparent electrodes", *Nature Nanotechnology*, vol. 5, no. Aug, pp. 1–5, 2009.

[268] A. N. Obraztsov, "Making graphene on a large scale", *Nature Nanotechnology*, vol. 4, no. April, pp. 212–213, 2009.

[269] X. Liang, B. A. Sperling, I. Calizo, G. Cheng, C. A. Hacker, Q. Zhang, Y. Obeng, K. Yan, H. Peng, Q. Li, X. Zhu, H. Yuan, A. R. H. Walker, Z. Liu, L.-M. Peng, and C. A. Richter, "Toward clean and crackless transfer of graphene.", *ACS Nano*, vol. 5, no. 11, pp. 9144–53, Nov. 2011.

[270] K. S. Novoselov, A. K. Geim, S. V. Morozov, D Jiang, M. I. Katsnelson, I. V. Grigorieva, S. V. Dubonos, and A. A. Firsov, "Two-dimensional gas of massless Dirac fermions in graphene.", *Nature*, vol. 438, no. 7065, pp. 197–200, Nov. 2005.

[271] M. Pimenta, G. Dresselhaus, M. Dresselhaus, L. Cançado, A. Jorio, and R. Saito, "Studying disorder in graphite-based systems by Raman spectroscopy", *Physical Chemistry Chemical Physics*, vol. 9, no. 11, pp. 1276–1291, 2007.

[272] A. C. Ferrari and J. Robertson, "Raman spectroscopy of amorphous, nanostructured, diamond-like carbon, and nanodiamond", *Philosophical Transactions of the Royal Society A: Mathematical, Physical and Engineering Sciences*, vol. 362, no. 1824, pp. 2477–2512, 2004.

[273] E. Duval, "Far infrared and Raman vibrational trasnsitions of a solid sphere: Selection rules", *Physical Review B*, vol. 46, no. 9, pp. 5795–5797, 1992.

[274] Y. Y. Wang, Z. H. Ni, T. Yu, Z. X. Shen, H. M. Wang, Y. H. Wu, W. Chen, and A. T. S. Wee, "Raman studies of monolayer graphene: The substrate effect", *Journal of Physical Chemistry C*, vol. 112, no. 29, pp. 10 637–10 640, 2008.

[275] D. Graf, F. Molitor, K. Ensslin, C. Stampfer, A. Jungen, and C. Hierold, "Spatially Resolved Raman Spectroscopy of Single and Few-Layer Graphene", *Nano Letters*, vol. 2, no. 2, pp. 238–242, 2007.

[276] L. M. Malard, M. A. Pimenta, G. Dresselhaus, and M. S. Dresselhaus, "Raman spectroscopy in graphene", *Physics Reports*, vol. 473, no. 5-6, pp. 51–87, 2009.

[277] B. Krauss, T. Lohmann, D. H. Chae, M. Haluska, K. Von Klitzing, and J. H. Smet, "Laser-induced disassembly of a graphene single crystal into a nanocrystalline network", *Physical Review B*, vol. 79, no. 16, pp. 1–9, 2009.

[278] T. M. G. Mohiuddin, A. Lombardo, R. R. Nair, A. Bonetti, G. Savini, R. Jalil, N. Bonini, D. M. Basko, C. Galiotis, N. Marzari, K. S. Novoselov, A. K. Geim, and A. C. Ferrari, "Uniaxial strain in graphene by Raman spectroscopy: G peak splitting, Grüneisen parameters, and sample orientation", *Physical Review B*, vol. 79, no. 20, pp. 205 433–8, 2009.

[279] F. C. Thorley, K. J. Baldwin, D. C. Lee, and D. N. Batchelder, "Dependence of the Raman spectra of drug substances upon laser excitation wavelength", *Journal of Raman Spectroscopy*, vol. 37, no. 1-3, pp. 335–341, 2006.

[280] R. Szostak and S. Mazurek, "Quantitative determination of acetylsalicylic acid and acetaminophen in tablets by FT-Raman spectroscopy", *Analyst*, vol. 127, no. 1, pp. 144–148, 2002.

[281] S. Berciaud, S. Ryu, L. Brus, and T. Heinz, "Probing the Intrinsic Properties of Exfoliated Graphene: Raman Spectroscopy of Free-Standing Monolayers", *Nano Letters*, vol. 9, no. 1, pp. 346–352, 2008.

[282] J. Zabel, R. R. Nair, A. Ott, T. Georgiou, A. K. Geim, K. S. Novoselov, and C. Casiraghi, "Raman spectroscopy of graphene and bilayer under biaxial strain: Bubbles and balloons", *Nano Letters*, vol. 12, no. 2, pp. 617–621, 2012.

[283] C. Metzger, S. Rémi, M. Liu, S. V. Kusminskiy, A. H. Castro Neto, A. K. Swan, and B. B. Goldberg, "Biaxial strain in graphene adhered to shallow depressions", *Nano Letters*, vol. 10, no. 1, pp. 6–10, 2010.

[284] F. Ding, H. Ji, Y. Chen, A. Herklotz, K. Dörr, Y. Mei, A. Rastelli, and O. G. Schmidt, "Stretchable graphene: A close look at fundamental parameters through biaxial straining", *Nano Letters*, vol. 10, no. 9, pp. 3453–3458, 2010.

[285] M. Huang, H. Yan, C. Chen, D. Song, T. F. Heinz, and J. Hone, "Phonon softening and crystallographic orientation of strained graphene studied by Raman spectroscopy.", *Proceedings of the National Academy of Sciences of the United States of America*, vol. 106, no. 18, pp. 7304–7308, 2009.

[286] D. Yoon, Y. W. Son, and H. Cheong, "Strain-dependent splitting of the double-resonance raman scattering band in graphene", *Physical Review Letters*, vol. 106, no. 15, pp. 1–4, 2011.

[287] J. W. Suk, W. H. Lee, J. Lee, H. Chou, R. D. Piner, Y. Hao, D. Akinwande, and R. S. Ruoff, "Enhancement of the electrical properties of graphene grown by chemical vapor deposition via controlling the effects of polymer residue", *Nano Letters*, vol. 13, no. 4, pp. 1462–1467, 2013.

[288] S. Ryu, L. Liu, S. Berciaud, Y. J. Yu, H. Liu, P. Kim, G. W. Flynn, and L. E. Brus, "Atmospheric oxygen binding and hole doping in deformed graphene on a SiO2 substrate", *Nano Letters*, vol. 10, no. 12, pp. 4944–4951, 2010.

[289] M. Z. Iqbal, M. W. Iqbal, M. F. Khan, and J. Eom, "Ultraviolet-light-driven doping modulation in chemical vapor deposition grown graphene.", *Physical Chemistry Chemical Physics*, vol. 17, no. 32, pp. 20 551–6, 2015.

[290] W. Kohn, "Image of the Fermi surface in the vibration spectrum of a metal", *Physical Review Letters*, vol. 2, no. 9, pp. 393–394, 1959.

[291] M. Lazzeri and F. Mauri, "Nonadiabatic Kohn anomaly in a doped graphene monolayer", *Physical Review Letters*, vol. 97, no. 26, pp. 266 407–4, 2006.

[292] S. Piscanec, M. Lazzeri, F. Mauri, A. C. Ferrari, and J. Robertson, "Kohn anomalies and electron-phonon interactions in graphite", *Physical Review Letters*, vol. 93, no. 18, pp. 1–4, 2004.

[293] S. A. E. Marras, F. Russell Kramer, and S. Tyagi, "Multiplex detection of single-nucleotide variations using molecular beacons", *Genetic Analysis - Biomolecular Engineering*, vol. 14, no. 5-6, pp. 151–156, 1999.

[294] X. Guo, A. Zafar, H. Nan, Y. Yu, W. Zhao, Z. Liang, X. Zhang, and N. Zhenhua, "Manipulating fluorescence quenching efficiency of graphene by defect engineering", *Applied Physics Express*, vol. 9, no. 5, pp. 055 502–3, 2016.

[295] R. F. Kubin and A. N. Fletcher, "Fluorescence quantum yields of some rhodamine dyes", *Journal of Luminescence*, vol. 27, no. 4, pp. 455–462, 1982.

[296] K. P. Loh, Q. Bao, P. K. Ang, and J. Yang, "The chemistry of graphene", *Journal of Materials Chemistry*, vol. 20, no. 12, pp. 2277–2289, 2010.

[297] A. Perry, S. J. Green, D. W. Horsell, S. M. Hornett, and M. E. Wood, "A pyrene-appended spiropyran for selective photo-switchable binding of Zn(||): UV-visible and fluorescence spectroscopy studies of binding and non-covalent attachment to graphene, graphene oxide and carbon nanotubes", *Tetrahedron*, vol. 71, no. 38, pp. 6776–6783, 2015.

[298] T. Alava, J. A. Mann, C. Théodore, J. J. Benitez, W. R. Dichtel, J. M. Parpia, and H. G. Craighead, "Control of the graphene-protein interface is required to preserve adsorbed protein function", *Analytical Chemistry*, vol. 85, no. 5, pp. 2754–2759, 2013.

[299] J. A. Mann and W. R. Dichtel, "Improving the binding characteristics of tripodal compounds on single layer graphene", *ACS Nano*, vol. 7, no. 8, pp. 7193–7199, 2013.

[300] Y. Cao, X. Li, D. Wang, X. Fan, X. Lu, Z. Zhang, C. Zeng, and Z. Zhang, "Highly anisotropic hybridization, dispersion, damping, and propagation of quantum plasmons in graphene superlattices", *Physical Review B*, vol. 90, no. 24, pp. 1–6, 2014.

[301] C. Zhang, L. Wu, D. Cai, C. Zhang, N. Wang, J. Zhang, and Z. Wu, "Adsorption of polycyclic aromatic hydrocarbons (fluoranthene and anthracenemethanol) by functional graphene oxide and removal by pH and temperature-sensitive coagulation", *ACS Applied Materials and Interfaces*, vol. 5, no. 11, pp. 4783–4790, 2013.

[302] F. M. Zehentbauer, C. Moretto, R. Stephen, T. Thevar, J. R. Gilchrist, D. Pokrajac, K. L. Richard, and J. Kiefer, "Fluorescence spectroscopy of Rhodamine 6G: Concentration and solvent effects", *Spectrochimica Acta - Part A: Molecular and Biomolecular Spectroscopy*, vol. 121, no. March, pp. 147–151, 2014.

[303] M. J. Tapia Estavez, F. L. Arbeloa, T. L. Arbeloa, and I. L. Arbeloa, "Absorption and Fluorescence Properties of Rhodamine 6G Adsorbed on Aqueous Suspensions of Wyoming Montmorillonite", *Langmuir*, vol. 9, no. 14, pp. 3629–3634, 1993.

[304] S. V. Polyakov, "Photomultiplier Tubes", *Experimental Methods in the Physical Sciences*, vol. 45, pp. 69–82, 2013.

[305] Hamamatsu, *https://www.hamamatsu.com/jp/en/ product/ category/ 3100/3001/ R960/index.html*, 2017.

[306] D.-W. Shin, D. Sung, J. S. Hong, M. Kim, S. S. Yoon, Y.-J. Song, G. Kim, S. Hong, and J.-B. Yoo, "Observation of graphene grain boundaries through selective adsorption of rhodamine B using fluorescence microscopy", *Carbon*, vol. 108, no. November, pp. 72–78, 2016.

[307] T. Yu, Z. Ni, C. Du, Y. You, Y. Wang, and Z. Shen, "Raman mapping investigation of graphene on transparent flexible substrate: The strain effect", *Journal of Physical Chemistry C*, vol. 112, no. 33, pp. 12 602–12 605, 2008.

[308] S. P. Mulvaney and C. D. Keating, "Raman Spectroscopy", *Journal of Raman Spectroscopy*, vol. 72, no. 12, pp. 145–158, 2000.

[309] K. Elibol, B. C. Bayer, S. Hummel, J. Kotakoski, G. Argentero, and J. C. Meyer, "Visualising the strain distribution in suspended two-dimensional materials under local deformation", *Scientific Reports*, vol. 6, no. April, pp. 28 485–9, 2016.

[310] Z. Li and N. Yu, "Modulation of mid-infrared light using graphene-metal plasmonic antennas", *Applied Physics Letters*, vol. 102, no. 13, pp. 131 108–1, 2013.

[311] N. M. R. Peres, Y. V. Bludov, A. Ferreira, and M. I. Vasilevskiy, "Exact solution for square-wave grating covered with graphene: surface plasmon-polaritons in the terahertz range.", *Journal of Physics: Condensed Matter*, vol. 25, no. 12, pp. 125 303–10, Mar. 2013.

[312] T. M. Slipchenko, M. L. Nesterov, L. Martin-Moreno, and A. Nikitin, "Analytical solution for the diffraction of an electromagnetic wave by a graphene grating", *Journal of Optics*, vol. 15, no. 11, pp. 114 008–20, Jul. 2013.

[313] P. Simonet, D. Bischoff, A. Moser, T. Ihn, and K. Ensslin, "Graphene nanoribbons: relevance of etching process", *Journal of Applied Physics*, vol. 117, no. 18, pp. 184 303–5, 2015.

[314] N. M. R. Peres, A. Ferreira, Y. V. Bludov, and M. I. Vasilevskiy, "Light scattering by a medium with a spatially modulated optical conductivity: the case of graphene.", *Journal of Physics: Condensed Matter*, vol. 24, no. 24, pp. 245 303–9, Jun. 2012.

[315] Z. Fang, S. Thongrattanasiri, A. Schlather, Z. Liu, L. Ma, Y. Wang, P. M. Ajayan, P. Nordlander, N. J. Halas, and F. J. García de Abajo, "Gated tunability and hybridization of localized plasmons in nanostructured graphene.", *ACS Nano*, vol. 7, no. 3, pp. 2388–2395, Mar. 2013.

[316] C. Ye, Z. Zhu, W. Xu, X. Yuan, and S. Qin, "Electrically tunable absorber based on nonstructured graphene", *Journal of Optics*, vol. 17, no. 12, pp. 125 009–6, 2015.

[317] Y. V. Bludov, A. Ferreira, N. Peres, and M. Vasilevskiy, "A Primer on Surface Plasmon-Polaritons in Graphene", *International Journal of Modern Physics B*, vol. 27, no. 10, pp. 1–75, Feb. 2013.

[318] J. W. Goodman, *Introduction to Fourier Optics*, Second, Roberts and Company Publishers, Ed. McGraw Hill, 2005, ISBN: 0974707724.

[319] W. Rechberger, A. Hohenau, A. Leitner, J. R. Krenn, B. Lamprecht, and F. R. Aussenegg, "Optical properties of two interacting gold nanoparticles", *Optics Communications*, vol. 220, no. 1, pp. 137–141, 2003.

[320] L. Novotny, "Strong coupling, energy splitting, and level crossings: A classical perspective", *American Journal of Physics*, vol. 78, no. 11, pp. 1199–1202, 2010.

[321] I. Luxmoore, P. Gan Ch .and Liu, and F. Valmorra, "Strong coupling in the far-infrared between graphene plasmons and the surface optical phonons of silicon dioxide", *ACS Photonics*, vol. 1, no. 11, pp. 1151–1155, 2014.

[322] B. Wunsch, T. Stauber, F. Sols, and F. Guinea, "Dynamical polarization of graphene at finite doping", *New Journal of Physics*, vol. 8, no. 12, pp. 318–337, 2006.

[323] A. Pirkle, J. Chan, A. Venugopal, D. Hinojos, C. W. Magnuson, S. McDonnell, L. Colombo, E. M. Vogel, R. S. Ruoff, and R. M. Wallace, "The effect of chemical residues on the physical and electrical properties of chemical vapor deposited graphene transferred to SiO_2", *Applied Physics Letters*, vol. 99, no. 12, pp. 122 108–3, 2011.

[324] J. L. Cheng, N. Vermeulen, and J. E. Sipe, "Third-order nonlinearity of graphene: Effects of phenomenological relaxation and finite temperature", *Physical Review B*, vol. 91, no. 23, pp. 235 320–22, 2015.

[325] V. Margulis, E. Muryumin, and E. Gaiduk, "Frequency dependence of optical third-harmonic generation from doped graphene", *Physics Letters A*, vol. 380, no. 1-2, pp. 304–310, 2016.

[326] T. V. Dolgova, A. I. Maidykovski, M. G. Martemyanov, A. A. Fedyanin, O. A. Aktsipetrov, G. Marowsky, V. A. Yakovlev, and G. Mattei, "Giant microcavity enhancement of second-harmonic generation in all-silicon photonic crystals", *Applied Physics Letters*, vol. 81, no. 15, pp. 2725–2727, 2002.

[327] T. V. Dolgova, A. I. Maidykovski, M. G. Martemyanov, A. A. Fedyanin, O. A. Aktsipetrov, G. Marowsky, V. A. Yakovlev, G. Mattei, N. Ohta, and S. Nakabayashi, "Giant optical second-harmonic generation in single and coupled microcavities formed from one-dimensional photonic crystals", *Journal of the Optical Society of America B*, vol. 19, no. 9, pp. 2129–2140, 2002.

[328] M. Liscidin and L. C. Andreani, "Highly efficient second-harmonic generation in doubly resonant planar microcavities", *Applied Physics Letters*, vol. 85, no. 11, pp. 1883–1885, 2004.

[329] T. Carmon and K. J. Vahala, "Visible continuous emission from a silica microphotonic device by third-harmonic generation", *Nature Physics*, vol. 3, no. 6, pp. 430–435, 2007.

[330] B. D. Kong, J. G. Champlain, and J. B. Boos, "Hot electron inelastic scattering and transmission across graphene surfaces", *Journal of Applied Physics*, vol. 121, no. 23, pp. 235 101–12, 2017.

[331] Thorlabs, *Https://www.thorlabs.com/*, 2017.

[332] C. Neumann, S. Reichardt, P. Venezuela, M. Drögeler, L. Banszerus, M. Schmitz, K. Watanabe, T. Taniguchi, F. Mauri, B. Beschoten, S. V. Rotkin, C. Stampfer, C. Neumann, S. Reichardt, and M Dro, "Raman spectroscopy as probe of nanometre-scale strain variations in graphene", *Nature Communications*, vol. 6, no. May, pp. 8429–6, 2015.

[333] V. J. Surya, K. Iyakutti, H. Mizuseki, and Y. Kawazoe, "Effect of strain on adsorption of hydrogen on graphene: A first-principles study", *AIP Conference Proceedings*, vol. 1447, no. 1, pp. 269–270, 2012.

[334] M. Yang, A. Nurbawono, C. Zhang, R. Wu, Y. Feng, and Ariando, "Manipulating absorption and diffusion of H atom on graphene by mechanical strain", *AIP Advances*, vol. 1, no. 3, pp. 032 109–7, 2011.

[335] F. Guinnea, M. I. Katsnelson, and A. K. Geim, "Energy gaps and a zero-field quantum Hall effect in graphene by strain engineering", *Nature Physics*, vol. 6, no. 1, pp. 30–33, 2009.

[336] N. Levy, S. A. Burke, K. L. Meaker, M. Panlasigui, A. Zettl, F. Guinea, A. H. C. Neto, and M. F. Crommie, "Strain-Induced Pseudo-Magnetic Fields Greater Than 300 Tesla in Graphene Nanobubbles", *Science*, vol. 329, no. July, pp. 544–547, 2010.

[337] F. Sols, F. Guinea, and A. H. C. Neto, "Coulomb blockade in graphene nanoribbons", *Physical Review Letters*, vol. 99, no. 16, pp. 1–4, 2007.

[338] E. R. Mucciolo, A. H. Castro Neto, and C. H. Lewenkopf, "Conductance quantization and transport gaps in disordered graphene nanoribbons", *Physical Review B*, vol. 79, no. 7, pp. 1–5, 2009.

[339] V. M. Pereira and A. H. Castro Neto, "Strain Engineering of Graphene's Electronic Structure", *Physical Review Letters*, vol. 103, no. 4, pp. 1–4, 2009.

[340] S. T. Gill, J. H. Hinnefeld, S. Zhu, W. J. Swanson, T. Li, and N. Mason, "Mechanical Control of Graphene on Engineered Pyramidal Strain Arrays", *ACS Nano*, vol. 9, no. 6, pp. 5799–5806, 2015.

[341] H. Kim and W. J. Kim, "Photothermally controlled gene delivery by reduced graphene oxide-polyethylenimine nanocomposite", *Small*, vol. 10, no. 1, pp. 117–126, 2014.

[342] J. D. Fowler, M. J. Allen, V. C. Tung, Y. Yang, R. B. Kaner, and B. H. Weiller, "Practical chemical sensors from chemically derived graphene", *ACS Nano*, vol. 3, no. 2, pp. 301–306, 2009.

[343] T. Kuila, S. Bose, P. Khanra, A. K. Mishra, N. H. Kim, and J. H. Lee, "Recent advances in graphene-based biosensors", *Biosensors and Bioelectronics*, vol. 26, no. 12, pp. 4637–4648, 2011.

[344] Q. H. Wang, Z. Jin, K. K. Kim, A. J. Hilmer, G. L. C. Paulus, C.-J. Shih, M.-H. Ham, J. D. Sanchez-Yamagishi, K. Watanabe, T. Taniguchi, J. Kong, P. Jarillo-Herrero, and M. S. Strano, "Understanding and controlling the substrate effect on graphene electron-transfer chemistry via reactivity imprint lithography.", *Nature Chemistry*, vol. 4, no. 9, pp. 724–32, 2012.

[345] F. H. Koppens, D. E. Chang, and F. J. Garcia de Abajo, "Graphene plasmonics: A platform for strong light–matter interactions", *Nano Letters*, vol. 11, no. 8, pp. 3370–3377, 2011.

[346] L. A. Blanco and F. J. García De Abajo, "Spontaneous light emission in complex nanostructures", *Physical Review B*, vol. 69, no. 20, pp. 1–12, 2004.

[347] V. M. Pereira, A. H. Castro Neto, and N. M. R. Peres, "Tight-binding approach to uniaxial strain in graphene", *Physical Review B*, vol. 80, no. 4, pp. 045 401–9, 2009.

[348] F. M. D. Pellegrino, G. G. N. Angilella, and R. Pucci, "Strain effect on the optical conductivity of graphene", *Physical Review B*, vol. 81, no. 3, pp. 035 411–12, 2010.

[349] V. M. Pereira, R. M. Ribeiro, N. M. R. Peres, and A. H. Castro Neto, "Optical properties of strained graphene", *Europhysics Letters*, vol. 92, no. 6, 67 001–p6, 2010.

[350] A. H. Castro Neto and F. Guinea, "Electron-phonon coupling and Raman spectroscopy in graphene", *Physical Review B*, vol. 75, no. 4, pp. 045 404–9, 2007.

[351] O. L. Blakslee, D. G. Proctor, E. J. Seldin, G. B. Spence, and T. Weng, "Elastic constants of compression-annealed pyrolytic graphite", *Journal of Applied Physics*, vol. 41, no. 8, pp. 3373–3382, 1970.

[352] G. X. Ni, H. Z. Yang, W. Ji, S. J. Baeck, C. T. Toh, J. H. Ahn, V. M. Pereira, and B. Özyilmaz, "Tuning optical conductivity of large-scale CVD graphene by strain engineering", *Advanced Materials*, vol. 26, no. 7, pp. 1081–1086, 2014.

[353] P. Alonso-Gonzalez, A. Y. Nikitin, F Golmar, A Centeno, A Pesquera, S. Velez, J Chen, G Navickaite, F Koppens, A Zurutuza, F Casanova, L. E. Hueso, and R Hillenbrand, "Controlling graphene plasmons with resonant metal antennas and spatial conductivity patterns", *Science*, vol. 1369, no. May, pp. 1–8, 2014.

[354] E. Luppi and V. Véniard, "A review of recent theoretical studies in nonlinear crystals: towards the design of new materials", *Semiconductor Science and Technology*, vol. 31, no. 12, pp. 123 002–20, 2016.

[355] C. Chen, Y. Wu, A. Jiang, B. Wu, G. You, R. Li, and S. Lin, "New nonlinear-optical crystal: LiB_3O_5", *Journal of the Optical Society of America B*, vol. 6, no. 4, pp. 616–621, 1989.

[356] Z. Sun, D. Popa, T. Hasan, F. Torrisi, F. Wang, E. J. R. Kelleher, J. C. Travers, and A. C. Ferrari, "Wideband tunable, graphene-mode locked, ultrafast laser", *Nano Research*, vol. 3, no. 653, pp. 653–660, 2010.

[357] N. Gao, T. Gao, X. Yang, X. Dai, W. Zhou, A. Zhang, and C. M. Lieber, "Specific detection of biomolecules in physiological solutions using graphene transistor biosensors.", *Proceedings of the National Academy of Sciences of the United States of America*, vol. 113, no. 51, pp. 14 633–14 638, 2016.

[358] J. Rodríguez-López, N. L. Ritzert, J. A. Mann, C. Tan, W. R. Dichtel, and H. D. Abruña, "Quantification of the surface diffusion of tripodal binding motifs on graphene using scanning electrochemical microscopy.", *Journal of the American Chemical Society*, vol. 134, no. 14, pp. 6224–36, 2012.